Title
Scalable fabrication of large-area graphene and graphene nano-composite films for flexible electronics and sensors.

Permalink
https://escholarship.org/uc/item/5167f9dj

Author
Zaretski, Aliaksandr

Publication Date
2016

Peer reviewed|Thesis/dissertation

UNIVERSITY OF CALIFORNIA, SAN DIEGO

Scalable fabrication of large-area graphene and graphene nano-composite films for flexible electronics and sensors.

A Dissertation submitted in partial satisfaction of the requirements for the degree of
Doctor of Philosophy

in

NanoEngineering

by

Aliaksandr Victorovich Zaretski

Committee in charge:

Professor Darren Lipomi, Chair
Professor Shaochen Chen
Professor Eric Fullerton
Professor Patrick Mercier
Professor Albert Pisano

2016

This Dissertation of Aliaksandr Victorovich Zaretski is approved, and it is acceptable in quality and form for publication on microfilm and electronically:

Chair

University of California, San Diego

2016

DEDICATION

To my dearest wife Sviatlana

TABLE OF CONTENTS

LIST OF FIGURES

LIST OF TABLES

ACKNOWLEDGEMENTS

This trip towards the doctorate degree has been exhilarating, illuminating, and rewarding and yet, as any worthy endeavor, sporadically sprinkled with stones and thorns. *Per aspera ad astra* indeed has been the motto. There is no way in this universe I could have reached this destination on my journey without the limitless and all-powerful support of my loving wife Sviatlana. She has been calming the surf when the seas were high and lifting up the surge when the tides were low. If ever the results of my work give meaningful fruit, my dear, You are the reason.

Even applying all the imagination, these days I cannot envision a scenario where I was doing my work in a laboratory of another professor other than Darren. So perfectly and harmoniously did my aspirations and ideas fit into the vision of Professor Lipomi, that I am sure, even half of the things we have discovered would have been impossible without the serendipity of our meeting. Ever so encouraging, inspiring, and benevolent, Darren is not unlike Yoda… Do I need to say more?!

All the first Darren's padovans: Adam, Suchol, Tim, I have learnt from each of you. Perseverance from Adam, drive to perfection from Suchol, categoricity from TimM. Sam showed to me such facets of genius that I have not previously encountered. I wish to thank "my students" (I hope I can call them that) Herad, Casey, Eduardo, Liban, and both Rachel O. and M. You gave me the pleasure of sharing knowledge and skills, of practicing academia and taught me in response. I hope some day to see your names among the best and the brightest of this world.

Having worked with all of you for the last four years has been an honor and a pleasure. Thank you for your guidance, help, advice, and patience.

I am very grateful to Rosibel Ochoa and everyone at The Von Liebig Center for setting me onto the path of entrepreneurship. *Per magis aspera nondum ad lucidius astra*, I hope.

I am very thankful to all the members of my dissertation committee for finding the time in your busy schedules and devoting hours of your life to my cause.

Of course, I thank my family: my mother Tamara, father Victor, and my brother Pavel. From the very beginning of my life you worked hard to “raise the embankments”, “dig the channels”, and direct the river of my life into the estuaries of today. Thank you!

I also include the following acknowledgements below as required by the University of California, San Diego.

Chapter 1, in full, is a reprint of the material as it appears in *Nanoscale* 7, 9963–9 (2015). Zaretski, A. V & Lipomi, D. J. Processes for non-destructive transfer of graphene: widening the bottleneck for industrial scale production. The dissertation author was the primary investigator and author of this paper.

Chapter 2, in full, is a reprint of the material as it appears in *Nanotechnology* 26, 045301 (2015). Aliaksandr V. Zaretski, Herad Moetazedi, Casey Kong, Eric J. Sawyer, Suchol Savagatrup, Eduardo Valle, Timothy F. O’Connor, Adam D. Printz, and Darren J Lipomi. Metal-assisted exfoliation (MAE): green, roll-to-roll compatible method for transferring graphene to flexible substrates. The dissertation author was the primary investigator and author of this paper.

Chapter 3, in full, is a reprint of the material as it appears in *Nano Lett*. 15, 635–640 (2015). Aliaksandr V. Zaretski, Brandon C. Marin, Herad Moetazedi, Tyler J. Dill, Liban Jibril, Casey Kong, Andrea R. Tao, and Darren J. Lipomi. Using the Thickness of

Graphene to Template Lateral Sub-Nanometer Gaps between Gold Nanostructures. The dissertation author was the primary investigator and author of this paper.

Chapter 4, in full, is a reprint of the material as it appears in *Nano Lett.* 16, 1375–1380 (2016). Aliaksandr V. Zaretski, Samuel E. Root, Alexander Savchenko, Elena Molokanova, Adam D. Printz, Liban Jibril, Gaurav Arya, Mark Mercola, and Darren J. Lipomi. Metallic Nanoislands on Graphene as Highly Sensitive Transducers of Mechanical, Biological, and Optical Signals. The dissertation author was the primary investigator and author of this paper.

VITA

2012	Bachelor of Science in Biomedical Engineering, Florida International University, Miami
2014	Master of Science in NanoEngineering, University of California, San Diego
2016	Doctor of Philosophy in NanoEngineering, University of California, San Diego

PUBLICATIONS

E. J. Sawyer, **A. V. Zaretski**, A. D. Printz, V. Nathaniel, A. Bautista-Gutierrez, and D. J. Lipomi, “Large increase in stretchability of organic electronic materials by encapsulation,” *Extreme Mechanics Letters*, 2016, In press.

T. F. O’Connor, **A. V. Zaretski**, S. Savagatrup, A. D. Printz, C. D. Wilkes, M. I. Diaz, D. J. Lipomi, “Wearable organic solar cells with high cyclic bending stability: Materials selection criteria,” *Solar Energy Materials & Solar Cells*, 2015, 144, 438.

A. V Zaretski, S. E. Root, A. Savchenko, E. Molokanova, A. D. Printz, L. Jibril, G. Arya, M. Mercola, and D. J. Lipomi, “Metallic Nanoislands on Graphene as Highly Sensitive Transducers of Mechanical, Biological, and Optical Signals,” *Nano Letters*, 2016, 16, 1375–1380.

A. V. Zaretski, D. J. Lipomi, Method for the fabrication and transfer of graphene, US patent 20,150,371,848, 2015.

A. D. Printz, **A. V. Zaretski,** S. Savagatrup, A. S-C. Chiang, and D. J. Lipomi, “Yield Point of Semiconducting Polymer Films on Stretchable Substrates Determined by Onset of Buckling,” *ACS Applied Materials & Interfaces,* 2015, 7, 23257.

S. Savagatrup†, A. D. Printz†, H. Wu, K. M. Rajan, E. J. Sawyer, **A. V. Zaretski**, C. J. Bettinger, and D. J. Lipomi, “Viability of Stretchable Poly(3-heptylthiophene) (P3HpT) for Organic Solar Cells and Field-Effect Transistors,” *Synthetic Metals*, 2015, 203, 208. († *Equal contribution*)

A. V. Zaretski, H. Moetazedi, C. Kong, E. J. Sawyer, S. Savagatrup, E. Valle, T. F. O’Connor, A. D. Printz, and D. J. Lipomi, “Metal-Assisted Exfoliation (MAE): Green, Roll-to-Roll Compatible Method for Transferring Graphene to Flexible Substrates,” *Nanotechnology*, 2015, 26, 045301.

A. V Zaretski, B. C. Marin, H. Moetazedi, T. J. Dill, L. Jibril, C. Kong, A. R. Tao, and D. J. Lipomi, "Using the thickness of graphene to template lateral subnanometer gaps between gold nanostructures," *Nano letters*, 2015, **15**, 635–640.

A. V. Zaretski, D. J. Lipomi, "Processes for non-destructive transfer of graphene: widening the bottleneck for industrial scale production*," Nanoscale*, 2015, **7**, 9963–9969.

S. Savagatrup, E. Chan, S. M. Renteria-Garcia, A. D. Printz, **A. V. Zaretski**, T. F. O'Connor, D. Rodriquez, E. Valle, and D. J. Lipomi, "Plasticization of PEDOT:PSS by Common Additives for Mechanically Robust Devices and Wearable Sensors," *Advanced Functional Materials*, 2015, 4, 13635.

S. Savagatrup, A. D. Printz, T. F. O'Connor, **A. V. Zaretski**, D. Rodriquez, E. J. Sawyer, K. Rajan, R. I. Acosta, S. E. Root, and D. J. Lipomi, "Mechanical Degradation and Stability of Organic Solar Cells: Molecular and Microstructural Determinants," *Energy and Environmental Science*, 2015, 8, 55

E. J. Sawyer, S. Savagatrup, T. F. O'Connor, A. S. Makaram, D. J. Burke, **A. V. Zaretski**, A. D. Printz, D. J. Lipomi, "Toward Intrinsically Stretchable Organic Semiconductors: Mechanical Properties of High-Performance Conjugated Polymers," *Proc. SPIE 9185, Organic Field-Effect Transistors XIII; and Organic Semiconductors in Sensors and Bioelectronics VII, 91850U (October 7, 2014); doi:10.1117/12.2059098*

S. Savagatrup, A. D. Printz, T. F. O'Connor, **A. V. Zaretski**, and D. J. Lipomi, "Molecularly Stretchable Electronics," *Chemistry of Materials*, 2014, 26, 3028.

T. F. O'Connor, **A. V. Zaretski**, B. A. Shiravi, S. Savagatrup, A. D. Printz, M. I. Diaz, and D. J. Lipomi, "Stretching and Conformal Bonding of Organic Solar Cells to Non-Planar Substrates," *Energy & Environmental Science*, 2014, 7, 370.

Chapter 1

Processes for non-destructive transfer of graphene: widening the bottleneck for industrial scale production

Aliaksandr V. Zaretski and Darren J. Lipomi

Department of NanoEngineering, University of California, San Diego

9500 Gilman Drive, Mail Code 0448, La Jolla, CA 92093-0448

Nanoscale

MINIREVIEW

Cite this: *Nanoscale*, 2015, **7**, 9963

Processes for non-destructive transfer of graphene: widening the bottleneck for industrial scale production

Aliaksandr V. Zaretski and Darren J. Lipomi*

The exceptional charge-transport, mechanical, and barrier properties of graphene are well known. High-quality films of single-layer graphene produced over large areas, however, are extremely expensive. The high cost of graphene precludes its use in industries—such as transparent electrodes and flexible packaging—that might take full advantage of its properties. This minireview presents several strategies for the transfer of graphene from the substrates used for growth to substrates used for the final application. Each strategy shares the characteristic of being non-destructive: that is, the growth substrate remains reusable for further synthesis of new graphene. These processes have the potential to lower significantly the costs of manufacturing graphene, to increase production yields, and to minimize environmental impact. This article is divided into sections on (i) the synthesis of high-quality single-layer graphene and (ii) its non-destructive transfer to a host substrate. Section (ii) is further divided according to the substrate from which graphene is transferred: single-crystalline wafers or flexible copper foils. We also comment, wherever possible, on defects produced as a result of the transfer, and potential strategies to mitigate these defects. We conclude that several methods for the green synthesis and transfer of graphene have several of the right characteristics to be useful in industrial scale production.

Received 19th March 2015,
Accepted 15th April 2015

DOI: 10.1039/c5nr01777g

www.rsc.org/nanoscale

1. Introduction.

While many of the most exciting potential applications of graphene exist at the nanoscale—*e.g.*, all-graphene integrated circuits—this versatile material has equally exciting applications on the very large scale. For example, graphene can substitute for indium-tin oxide in transparent conducting electrodes,[1,2] can serve as a gas-separation membrane,[3] and exhibits barrier properties for the encapsulation of organic electronic devices.[4] All these applications require large areas of this material. For graphene to constitute any considerable segment of the global markets for these applications, the outstanding performance and properties of graphene have to be accompanied by large-volume manufacturability at low cost and with minimal environmental impact. Manufacturing for large-area applications can be subdivided into two steps: synthesis and transfer.

Methods for synthesizing graphene have been under investigation since 2004.[5] The intensity of this work has resulted in the ability to synthesize large areas of graphene (100 m sheets) in a roll-to-roll fashion[6] at high speeds (0.6 m min^{-1}).[7] Nevertheless, there appears to be a bottleneck in the industrial-scale production of graphene, that is, inexpensive, non-destructive transfer from the substrate used for synthesis to the final substrate used for the application. The current state-of-the-art techniques for transferring high-quality single layers are slow (*i.e.*, they cost a minimum of 30 min per batch because of etching the growth substrate) and deleterious to the environment.[8] To enable proliferation of large-area graphene to every industry for which the material has potential—and potentially great—value, the ability to transfer graphene rapidly and in a non-destructive manner is required. While there exist methodologies of inexpensive large-volume production of suspensions of exfoliated graphene that can be spray-coated onto a substrate to generate conducting surfaces[9] or mixed in with polymers to make conductive composites[10] and barrier films,[11] this minireview focuses only on processes for transfer that preserve the desirable characteristics of high-quality single-layer graphene, including high transparency, high electron mobility, and low sheet resistance.[12]

2. Synthesis of large-area graphene

There are two principal methodologies for the synthesis of large-area single-layer graphene: silicon-carbide (SiC) epitaxy[13] and chemical vapor deposition (CVD).[14] While neither of the techniques guarantees the formation of a single-layer of gra-

---

Department of NanoEngineering, University of California, San Diego, 9500 Gilman Drive Mail Code 0448, La Jolla, CA 92093-0448, USA. E-mail: dlipomi@ucsd.edu

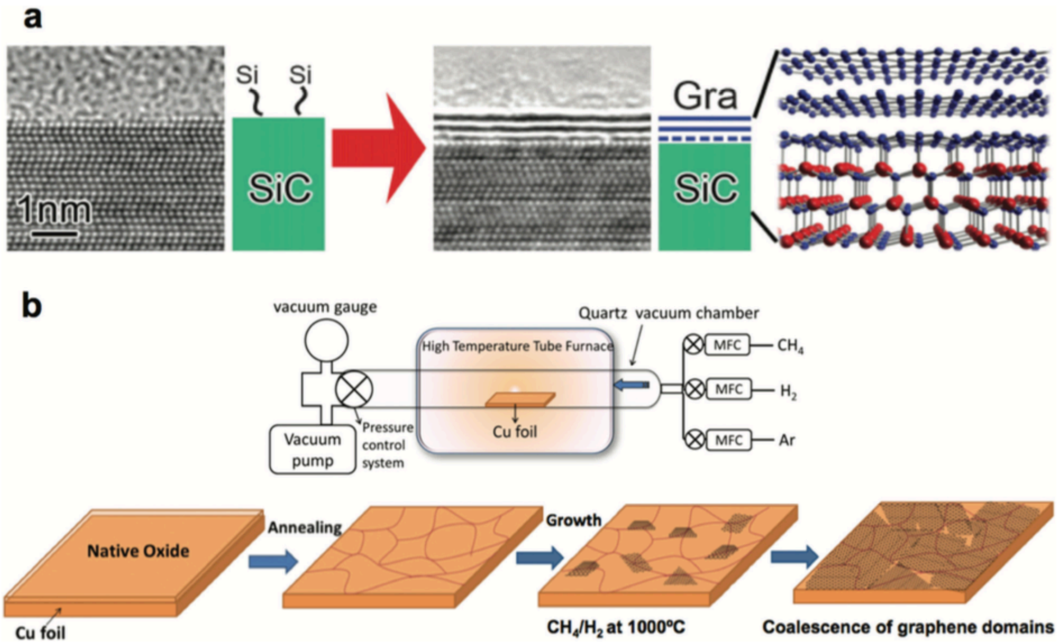

Fig. 1 Methods for synthesizing high-quality large-area graphene. (a) Epitaxial synthesis of graphene on a SiC wafer. Reproduced with permission from ref. 13. Copyright 2014, Royal Society of Chemistry. (b) Chemical vapor deposition (CVD) of graphene on copper foil. Reproduced with permission from ref. 16, Copyright 2011, American Chemical Society, and from ref. 20, Copyright 2013, InTech.

phene, both can be modified to do so, and both have their advantages and limitations.

2.1 SiC epitaxy

In SiC epitaxy, a single crystalline SiC wafer is heated in a vacuum or argon atmosphere to the temperatures above 2000 °C. At this temperature, silicon atoms sublimate from the (0001) face of the crystal. The remaining carbon (which has a lower vapor pressure than silicon) rearranges to form graphene (Fig. 1a).[13] By tight control of the parameters of this process, synthesis of single-, few-, and multilayer graphene has been demonstrated.[15] One particular advantage of this method is that it produces graphene covering the entire surface of an insulating wafer, and thus allows the fabrication of circuitry directly on the growth substrate. Such graphene possesses exceptionally high electron mobilities, which is desirable for high-performance components of integrated circuits. We return to this process in section 3.1.1 when we discuss the process of transferring single layer graphene from the SiC wafer onto flexible host substrates.

2.2 CVD of graphene

The process of chemical vapor deposition (CVD) of graphene offers great versatility as it allows synthesis of single- or multilayer graphene on a large number of substrates (usually refractory metals,[16] Fig. 1b). The use of copper foil is by far the best studied, because copper is relatively inexpensive. Moreover, the low solubility of carbon in copper permits synthesis of predominantly single layer graphene of high quality.[16] CVD of graphene can be performed in vacuum[17] or atmospheric pressure[18] and at temperatures as low as 300 °C.[19] Additionally, as compared to SiC epitaxy, CVD of graphene is not limited to the small dimensions of a wafer.

3. Graphene transfer methods

In order to be usable, the graphene synthesized on copper foil by CVD has to be transferred to the substrate of interest, which usually requires supporting of graphene by a polymeric film and etching the copper foil in a corrosive medium[8,20] (Fig. 2). Such transfer processes are time consuming: it takes at least 30 min to dissolve 25 μm-thick copper foil. This process is also wasteful: it requires 300 kg of copper to produce 1 g of graphene,[21] and thus produces an outsized amount of toxic waste. These disadvantages currently limit the fabrication of graphene to small amounts mostly for research and development purposes and need to be overcome in order to make graphene over large areas at low costs.

3.1 Non-destructive graphene transfer

In order to remove graphene from the synthesis substrate non-destructively so that the substrate can be recycled, the

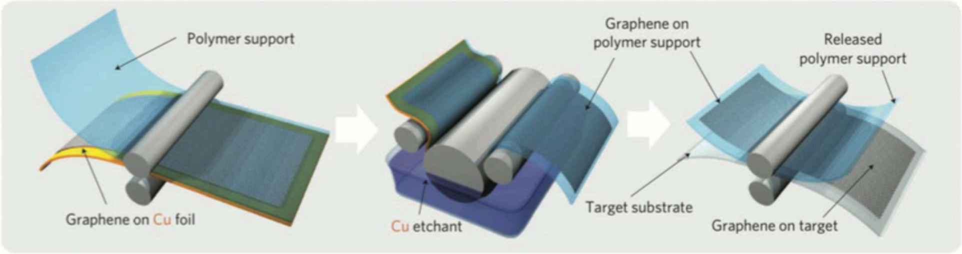

Fig. 2 Schematic of the wet roll-to-roll graphene transfer from copper foils to polymeric substrates. Reproduced with permission from ref. 8. Copyright 2010, Nature Publishing Group.

adhesion between graphene and the growth substrate needs to be overcome. Despite its mechanical strength, a single-layer of graphene is too delicate to be exfoliated unsupported, or manipulated as a free-standing film, and thus requires a relatively rigid backing. Typically, the rigid support is a thicker polymeric sheet or foil that, in some cases, is the final receiving substrate, or is an intermediate substrate used only for mechanical support during transfer. In any case, the strength of adhesion of graphene to the supporting substrate has to be greater than to the substrate used for growth. The supporting substrate can provide strong adhesion in either its native state or it can be modified with adhesion layers whose effect is produced by covalent or van der Waals bonding. Knowing both values of adhesion energy, or at least their relative magnitudes, allows the design of the graphene exfoliation process from a given growth substrate to the final receiving substrate either directly or using a multi-step manipulation. The strengths of adhesion of graphene to various media are listed in Table 1.

The design of a process to exfoliate graphene is not limited to the relative strengths of adhesion between graphene and the substrate used for synthesis and the substrate used for exfoliation. For example, the roughness of the substrate used for growth and the parameters of processing—*e.g.*, the temperature and pressure at which the supporting substrate is deposited, which affects the interfacial area between the graphene and the supporting substrate—also plays a key role. A hot press is often used to apply the supporting substrate to increase its adhesion to the graphene. Another consideration is the chemical modification of graphene by the supporting/adhesion layer (covalent bonding, doping), which can potentially change the electronic properties of graphene.[29] Not least important are the mechanical aspects of the transfer process such as the distribution of stress during the exfoliation, which may be especially problematic with roll-to-roll transfer. For example, a film that is 200 microns thick when bent to the radius of 5 millimeters experiences a tensile strain on the top surface of 2% and an equal in magnitude compressive strain on the bottom surface.[30] Such strains can cause catastrophic failures in a number of thin-film materials.[31]

Table 1 Strength of adhesion of graphene to growth/support substrates

Interface	Strength of adhesion (J m^{-2})	Ref.
Graphene/graphene	0.3	22
Graphene/copper	0.4–0.7	23–25
Graphene/gold	0.7	26
Graphene/SiC	2.3–3.0	27 and 28
Graphene/nickel	3.5	23

3.1.1 Graphene transfer from single-crystalline wafers. As discussed in section 2.1, SiC epitaxy is a useful technique for generating high-quality graphene with a high degree of control over the number of graphene layers and their crystallographic orientations.[15] Additionally, graphene synthesized in this fashion exhibits minimal surface roughness. Considering the weak graphene/graphene interlayer interaction (Table 1), it is easily exfoliated from a multilayer stack.[32] As demonstrated by Kim *et al.*,[33] however, even single-layer graphene, which is relatively strongly bonded to SiC, can be exfoliated with the right adhesion layer. Using an evaporated thin nickel film as an adhesion layer and thermal-release tape as the supporting substrate, the authors were able to exfoliate single-layer graphene (with some graphene add-layers) from the SiC wafer by direct fracture of the SiC/graphene interface. The authors "cleaned" the transferred graphene—*i.e.*, removed the add-layers—by evaporating and subsequently exfoliating a thin film of gold, along with the noncontiguous sheets of the double layers. The choice of gold was justified because its adhesion to graphene is stronger than graphene to graphene, but weaker than nickel to graphene. The resulting graphene appeared contiguous and exhibited a minimal D-peak in the Raman spectrum. The low intensity of this signal was consistent with a low density of defects (Fig. 3a). This nickel-supported graphene could also be transferred onto the final receiving substrate (Si/SiO_2 wafer) after which the metal could easily be etched away. After exfoliation of graphene, the SiC wafer was immediately available for an additional cycle of graphene synthesis. Besides providing the necessary adhesion strength, the evaporated nickel film

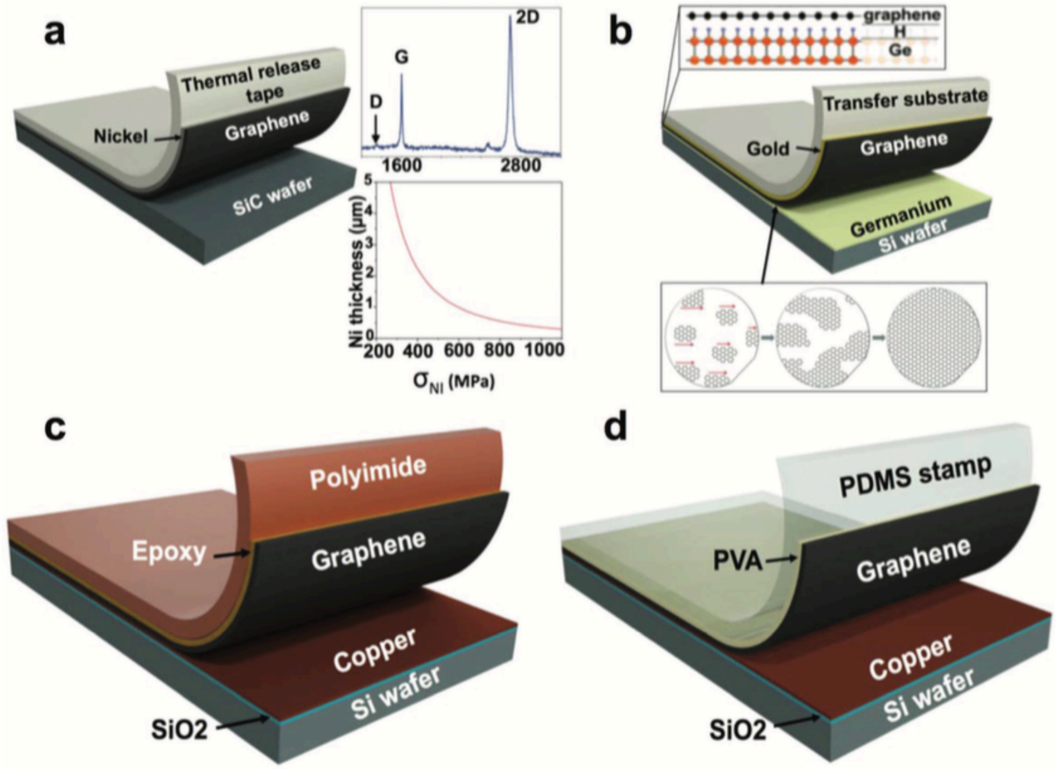

Fig. 3 Summary of methods used to transfer graphene from single-crystalline wafers. (a) Schematic diagram of graphene transfer from SiC wafer after SiC epitaxy. Reproduced with permission from ref. 33. Copyright 2013, American Association for the Advancement of Science. (b) Graphene transfer from a silicon wafer bearing a film of germanium. Reproduced with permission from ref. 35. Copyright 2014, American Association for the Advancement of Science. (c) Graphene transfer from evaporated copper substrate using epoxy. Adapted from ref. 25. (d) Graphene transfer from evaporated copper substrate using a PDMS/PVA stamp. Adapted from ref. 36.

imposes epitaxial stress onto graphene. The additional stress facilitated adhesive fracture of the copper/graphene interface during the exfoliation.[34]

Repetitive synthesis by CVD and subsequent exfoliation of a wafer-scale single-crystalline single-layer graphene from a hydrogen-terminated germanium-coated silicon wafer has been demonstrated by Lee *et al.*[35] This process was facilitated by three characteristics (1) the low solubility of carbon in germanium, (2) its catalytic activity toward methane cracking, and (3) its perfect crystalline order as deposited on the surface of the silicon wafer. The hydrogen-terminated germanium, which exhibited a weak adhesion to graphene, allowed the authors to exfoliate the graphene from the wafer using a thin film of evaporated gold (Fig. 3b). This group also demonstrated a repetitive sequential graphene synthesis and exfoliation from the same wafer without any apparent deterioration of the graphene.[35]

Copper evaporated onto a silicon wafer bearing a layer of thermally grown oxide can also support CVD of graphene. Yoon *et al.*[25] demonstrated the effective direct exfoliation of graphene from the copper-coated wafer to a flexible polyimide film (PI) by binding them with epoxy as the permanent adhesion layer (Fig. 3c). The authors stated that this approach helped to avoid doping of graphene with metals and the detrimental acidic treatments. They demonstrated the utility of the graphene prepared in this manner by fabricating a flexible field-effect transistor (FET) with good gate modulation of the graphene channel conductivity on the PI film. Regrowth of graphene on the same substrate was performed and generated graphene with a somewhat increased defect density as judged by the Raman D-peak of graphene on copper.[25] This defectiveness could be explained in principle by the evaporative deterioration of the thin copper layer during graphene synthesis.

Similarly, Yang *et al.*[36] employed an adhesion layer, albeit water soluble—polyvinyl alcohol—to exfoliate graphene from copper-coated Si/SiO$_2$ wafer and to transfer it to arbitrary substrates (Fig. 3d). During the transfer, graphene sustained minimal physical damage, as indicated by the D/G peak ratio of 0.06. A polydimethylsiloxane (PDMS) stamp served as a support substrate for the transfer and provided a kinetically controlled adhesion necessary for the graphene transfer: rapidly peeling the stamp away from the copper-coated wafer promoted exfoliation of the PVA-coated graphene. In the next step, the PVA-coated graphene was pressed against the final receiving substrate and by peeling the stamp away slowly was released. After the transfer, the PVA adhesion layer could be dissolved in deionized water. As with the exfoliation process that did not involve metal etching, developed by Yoon *et al.*[25] above, the graphene produced by this method was free of doping and preserves its charge neutrality with the value of V_{dirac} close to 0 V in the FETs fabricated with the exfoliated graphene.

3.1.2 Graphene transfer from copper foil. Certain applications require the synthesis of graphene over areas greater than are possible using the largest available single crystalline wafers (≤12 inches in diameter). These applications include transparent conducting electrodes for liquid crystal displays, photovoltaic panels, and barrier films for electronics and flexible packaging. So far, the only method that can generate equal or greater areas of single-layer and high-quality material is CVD on copper foil. Exfoliation of graphene is especially challenging due to the intrinsic surface roughness and highly pliable nature of the copper foil after annealing. Due to the manufacturing process (cold-rolling), commercially available copper foils have grooves that, in turn, produce highly anisotropic rms roughness of 615 nm.[18] Even when the copper foils are electropolished and the roughness is reduced to 148 nm,[18] after graphene synthesis, >150 nm-deep fissures form at the copper grain boundaries.[37] In case of atomically smooth copper films produced by deposition and stripping from a single-crystalline wafer, heating to 1000 °C increases the roughness from 0.5 nm to above 10 nm.[19] Hence the exfoliation process designed for removing graphene from copper foils needs to accommodate the roughness. Several groups have designed such processes that employ a polymeric receiving substrate and a hot press that heats the polymer above its glass transition temperature, while the high pressure molds the polymer into the relief structures in the copper foil. In this way, Fechine *et al.*[38] demonstrated a complete graphene trans-

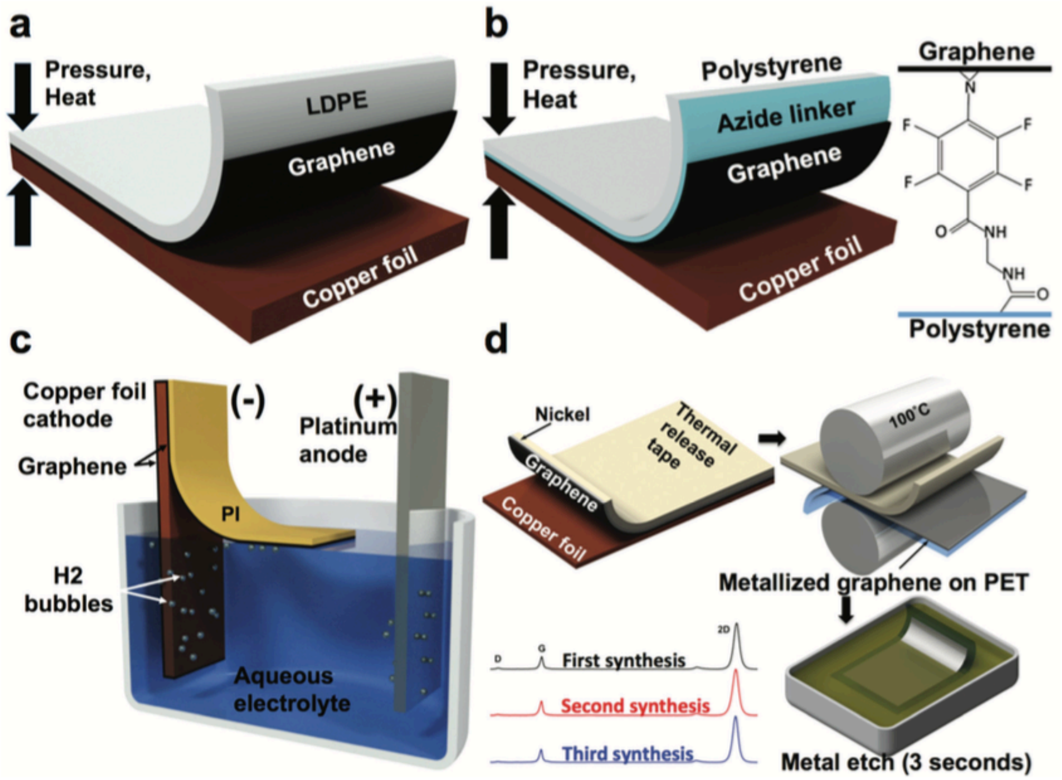

Fig. 4 Summary of methods used to transfer graphene from flexible copper foils. (a) Direct dry transfer of graphene from copper foil to polymeric substrates using a hot press. Adapted from ref. 38. (b) Adhesion molecule assisted dry transfer of graphene from copper foil to polymeric substrates using a hot press. Adapted from ref. 39. (c) Electrochemical delamination of PI-supported graphene from copper foil. Adapted from ref. 43. (d) Metal-assisted exfoliation of graphene from copper foil. Adapted from ref. 21.

fer (albeit of an unknown graphene intactness) from a copper foil to low-density polyethylene (LDPE) and to other polymers (Fig. 4a).

A similar approach enhanced with a molecule that covalently bonds graphene to polystyrene—*N*-ethylamino-4-azidotetrafluorobenzoate (TFPA-NH_2)—was employed by Lock *et al.*[39–41] and resulted in graphene with a sheet resistance of about 1 kΩ sq^{-1} (Fig. 4b). TFPA is known to form strong covalent bonds with graphene[42] and thus the polystyrene substrate was dip-coated in TFPA-NH_2 solution after plasma treatment to promote the adhesion to graphene. It is noteworthy that without the TFPA treatment, polystyrene demonstrated poor adhesion, which resulted in only partial (19%) transfer.[38]

A noteworthy process to transfer graphene non-destructively by "electrochemical delamination" has been demonstrated by Wang *et al.*[43] In this process, the final receiving substrate (PI) is spin–coated on the CVD graphene on copper foil, which serves as a cathode in an electrochemical cell with 0.5 M sodium hydroxide as an electrolyte and platinum wire mesh as an anode. By applying a 15 V bias between the electrodes, hydrolysis of water produced hydrogen bubbles between the copper foil and graphene and promoted separation of this interface (Fig. 4c). Graphene supported by 9 μm-thick PI was observed to float away from the copper foil. It was then collected, and its conductivity was measured under various bending radii. The process reportedly took 5 min for a 50 × 15 mm size sheet and generated graphene with a sheet resistance of 459 Ω sq^{-1}.

Our laboratory reported a process for exfoliating single-layer graphene from copper foils without the use of a hot press, nicknamed metal-assisted exfoliation (MAE, Fig. 4d).[21] This method employed the evaporation of a thin film (>20 nm) of nickel or cobalt onto the CVD-grown graphene on copper foil. The preferential adhesion of graphene to nickel and cobalt ensured delamination of graphene from the copper during exfoliation, while the use of a thermal-release tape as the supporting substrate enabled the transfer of the metalized exfoliated graphene onto flexible transparent polymeric films bearing a thermoplastic adhesive by quick processing through a commercial document laminator. Further, the nanoscopic metal film (nickel or cobalt) could be etched rapidly in an acidic solution to yield single-layer graphene on a flexible polymeric film.

The mechanical stresses induced in thin films during exfoliation process need to be considered as even small forces may cause large deformations. Evidence of the effects of anisotropic stresses induced in roll-to-roll processing is the anisotropic sheet resistances of the graphene resulting from MAE when excessively large tensile strains are imposed onto the metallized graphene during the process of exfoliation. The bending radii of the metallized graphene supported by thermal release tape during the manual exfoliation were small enough to cause metal film cracking that propagates through graphene and produced sheet resistances on the order of 0.8 kΩ sq^{-1} parallel to the cracks and 8 kΩ sq^{-1} in the perpendicular orientation. This problem can in principle be solved by avoiding excessively small bending radii during the exfoliation process or by using very thin supporting substrates.

4. Conclusion

With more than 8000 patents filed to date, graphene has been proposed for a multitude of possible applications in a number of various industries. It is likely that different approaches of graphene synthesis and transfer will be used for different applications, considering the strong dependence of the quality, yield, and cost of graphene based on the process selected. Some of the processes discussed in this minireview may be better suited for research and development and small chip-scale production, while others are more amenable to industrial-scale roll-to-roll fabrication schemes. Further developments are needed in order to overcome the still remaining shortcomings: mechanical damage during exfoliation, the use of expensive sacrificial layers (evaporated metal films) and transfer substrates (thermal-release tapes and thermoplastic adhesives). In particular, routes of mechanical degradation of the graphene should be characterized more fully than they currently are, so that these pathways can be mitigated. We conclude that non-destructive, economically feasible, and environmentally friendly and sustainable processes for manufacturing graphene at scales demanded by industry will need to be further developed, though several potentially significant strategies have been proposed. Progress in these areas is required if this material is to make a truly significant impact on society.

Acknowledgements

This work was supported by the laboratory startup funds from the University of California, San Diego. A. Z. acknowledges a fellowship from SoCal Clean Energy Technology Acceleration Program from the von Liebig Center at UCSD sponsored by the US Department of Energy, and a fellowship from the National Science Foundation Graduate Research Fellowship Program, DGE-1144086.

References

1 I. Khrapach, F. Withers, T. H. Bointon, D. K. Polyushkin, W. L. Barnes, S. Russo and M. F. Craciun, *Adv. Mater.*, 2012, **24**, 2844–2849.
2 J. Ryu, Y. Kim, D. Won, N. Kim, J. S. Park, E.-K. Lee, D. Cho, S.-P. Cho, S. J. Kim, G. H. Ryu, H.-A.-S. Shin, Z. Lee, B. H. Hong and S. Cho, *ACS Nano*, 2014, **8**, 950–956.
3 D. E. Jiang, V. R. Cooper and S. Dai, *Nano Lett.*, 2009, **9**, 4019–4024.
4 Z. Liu, J. Li and F. Yan, *Adv. Mater.*, 2013, **25**, 4296–4301.
5 K. S. Novoselov, A. K. Geim, S. V. Morozov, D. Jiang, Y. Zhang, S. V. Dubonos, I. V. Grigorieva and A. A. Firsov, *Science*, 2004, **306**, 666–669.

6 T. Kobayashi, M. Bando, N. Kimura, K. Shimizu, K. Kadono, N. Umezu, K. Miyahara, S. Hayazaki, S. Nagai, Y. Mizuguchi, Y. Murakami and D. Hobara, *Appl. Phys. Lett.*, 2013, **102**, 023112.

7 T. Yamada, J. Kim, M. Ishihara and M. Hasegawa, *J. Phys. D: Appl. Phys.*, 2013, **46**, 063001.

8 S. Bae, H. Kim, Y. Lee, X. Xu, J.-S. Park, Y. Zheng, J. Balakrishnan, T. Lei, H. R. Kim, Y. Il Song, Y.-J. Kim, K. S. Kim, B. Ozyilmaz, J.-H. Ahn, B. H. Hong and S. Iijima, *Nat. Nanotechnol.*, 2010, **5**, 574–578.

9 D.-Y. Kim, S. Sinha-Ray, J.-J. Park, J.-G. Lee, Y.-H. Cha, S.-H. Bae, J.-H. Ahn, Y. C. Jung, S. M. Kim, A. L. Yarin and S. S. Yoon, *Adv. Funct. Mater.*, 2014, **24**, 4986–4995.

10 Y. Li, Y. A. Samad, K. Polychronopoulou, S. M. Alhassan and K. Liao, *Sci. Rep.*, 2014, **4**, 4652.

11 Y. Su, V. G. Kravets, S. L. Wong, J. Waters, A. K. Geim and R. R. Nair, *Nat. Commun.*, 2014, **5**, 4843.

12 J. S. Bunch, S. S. Verbridge, J. S. Alden, A. M. Van Der Zande, J. M. Parpia, H. G. Craighead and P. L. McEuen, *Nano Lett.*, 2008, **8**, 2458–2462.

13 W. Norimatsu and M. Kusunoki, *Phys. Chem. Chem. Phys.*, 2014, **16**, 3501–3511.

14 A. Reina, X. Jia, J. Ho, D. Nezich, H. Son, V. Bulovic, M. S. Dresselhaus and J. Kong, *Nano Lett.*, 2008, **9**, 30–35.

15 W. Norimatsu and M. Kusunoki, *Chem. Phys. Lett.*, 2009, **468**, 52–56.

16 C. Mattevi, H. Kim and M. Chhowalla, *J. Mater. Chem.*, 2011, **21**, 3324.

17 N. S. Mueller, A. J. Morfa, D. Abou-Ras, V. Oddone, T. Ciuk and M. Giersig, *Carbon N. Y.*, 2014, **78**, 347–355.

18 I. Vlassiouk, P. Fulvio, H. Meyer, N. Lavrik, S. Dai, P. Datskos and S. Smirnov, *Carbon N. Y.*, 2013, **54**, 58–67.

19 P. Procházka, J. Mach, D. Bischoff, Z. Lišková, P. Dvořák, M. Vaňatka, P. Simonet, A. Varlet, D. Hemzal, M. Petrenec, L. Kalina, M. Bartošík, K. Ensslin, P. Varga, J. Čechal and T. Šikola, *Nanotechnology*, 2014, **25**, 185601.

20 A. Kumar and C. H. Lee, in *Advances in Graphene Science*, ed. M. Aliofkhazraei, 2013, pp. 55–75. DOI: 10.5772/55728.

21 A. V. Zaretski, H. Moetazedi, C. Kong, E. J. Sawyer, S. Savagatrup, E. Valle, T. F. O'Connor, A. D. Printz and D. J. Lipomi, *Nanotechnology*, 2015, **26**, 45301.

22 D. J. Henry, G. Yiapanis, E. Evans and I. Yarovsky, *J. Phys. Chem. B*, 2005, **109**, 17224–17231.

23 J. Lahiri, T. S. Miller, A. J. Ross, L. Adamska, I. I. Oleynik and M. Batzill, *New J. Phys.*, 2011, **13**, 025001.

24 Z. Xu and M. J. Buehler, *J. Phys.: Condens. Matter*, 2010, **22**, 485301.

25 T. Yoon, W. C. Shin, T. Y. Kim, J. H. Mun, T.-S. Kim and B. J. Cho, *Nano Lett.*, 2012, **12**, 1448–1452.

26 I. Hamada and M. Otani, *Phys. Rev. B: Condens. Matter Mater. Phys.*, 2010, **82**, 153412.

27 A. Mattausch and O. Pankratov, *Phys. Rev. Lett.*, 2007, **99**, 086802.

28 G. H. Wells, T. Hopf, K. V. Vassilevski, E. Escobedo-Cousin, N. G. Wright, A. B. Horsfall, J. P. Goss, A. G. O'Neill and M. R. C. Hunt, *Appl. Phys. Lett.*, 2014, **105**, 193109.

29 H. Liu, Y. Liu and D. Zhu, *J. Mater. Chem.*, 2011, **21**, 3335.

30 N. Lu, Z. Suo and J. J. Vlassak, *Acta Mater.*, 2010, **58**, 1679–1687.

31 S. Savagatrup, A. D. Printz, T. F. O'Connor, A. V. Zaretski, D. Rodriquez, E. J. Sawyer, K. M. Rajan, R. I. Acosta, S. E. Root and D. J. Lipomi, *Energy Environ. Sci.*, 2015, **8**, 55–80.

32 T. Moldt, A. Eckmann, P. Klar, S. V. Morozov, A. A. Zhukov, K. S. Novoselov and C. Casiraghi, *ACS Nano*, 2011, **5**, 7700–7706.

33 J. Kim, H. Park, J. B. Hannon, S. W. Bedell, K. Fogel, D. K. Sadana and C. Dimitrakopoulos, *Science*, 2013, **342**, 833–836.

34 Y. He, W. F. Chen, W. B. Yu, G. Ouyang and G. W. Yang, *Sci. Rep.*, 2013, **3**, 2660.

35 J.-H. Lee, E. K. Lee, W.-J. Joo, Y. Jang, B.-S. Kim, J. Y. Lim, S.-H. Choi, S. J. Ahn, J. R. Ahn, M.-H. Park, C.-W. Yang, B. L. Choi, S.-W. Hwang and D. Whang, *Science*, 2014, **344**, 286–289.

36 S. Y. Yang, J. G. Oh, D. Y. Jung, H. Choi, C. H. Yu, J. Shin, C.-G. Choi, B. J. Cho and S.-Y. Choi, *Small*, 2015, **11**, 175–181.

37 D. Lee, G. D. Kwon, J. H. Kim, E. Moyen, Y. H. Lee, S. Baik and D. Pribat, *Nanoscale*, 2014, **6**, 12943–12951.

38 G. J. M. Fechine, I. Martin-Fernandez, G. Yiapanis, R. Bentini, E. S. Kulkarni, R. V. Bof de Oliveira, X. Hu, I. Yarovsky, A. H. Castro Neto and B. Özyilmaz, *Carbon N. Y.*, 2015, **83**, 224–231.

39 E. H. Lock, M. Baraket, M. Laskoski, S. P. Mulvaney, W. K. Lee, P. E. Sheehan, D. R. Hines, J. T. Robinson, J. Tosado, M. S. Fuhrer, S. C. Hernández and S. G. Walton, *Nano Lett.*, 2012, **12**, 102–107.

40 E. H. Lock, D. M. Delongchamp, S. W. Schmucker, B. Simpkins, M. Laskoski, S. P. Mulvaney, D. R. Hines, M. Baraket, S. C. Hernandez, J. T. Robinson, P. E. Sheehan, C. Jaye, D. A. Fisher and S. G. Walton, *Carbon N. Y.*, 2015, **86**, 288–300.

41 E. H. Lock, S. C. Hernández, T. J. Anderson, S. W. Schmucker, M. Laskoski, S. P. Mulvaney, F. J. Bezares, J. D. Caldwell, P. E. Sheehan, J. T. Robinson, B. N. Feygelson and S. G. Walton, *Surf. Coat. Technol.*, 2014, **241**, 118–122.

42 L. H. Liu and M. Yan, *Nano Lett.*, 2009, **9**, 3375–3378.

43 X. Wang, L. Tao, Y. Hao, Z. Liu, H. Chou, I. Kholmanov, S. Chen, C. Tan, N. Jayant, Q. Yu, D. Akinwande and R. S. Ruoff, *Small*, 2014, **10**, 694–698.

Chapter 2

Metal-assisted exfoliation (MAE): green, roll- to-roll compatible method for transferring graphene to flexible substrates

Aliaksandr V. Zaretski, Herad Moetazedi, Casey Kong, Eric J. Sawyer, Suchol Savagatrup, Eduardo Valle, Timothy F. O'Connor, Adam D. Printz, and Darren J Lipomi

Department of NanoEngineering, University of California, San Diego

9500 Gilman Drive, Mail Code 0448, La Jolla, CA 92093-0448

IOP Publishing Nanotechnology

Nanotechnology **26** (2015) 045301 (7pp) doi:10.1088/0957-4484/26/4/045301

Metal-assisted exfoliation (MAE): green, roll-to-roll compatible method for transferring graphene to flexible substrates

Aliaksandr V Zaretski, Herad Moetazedi, Casey Kong, Eric J Sawyer, Suchol Savagatrup, Eduardo Valle, Timothy F O'Connor, Adam D Printz and Darren J Lipomi

Department of NanoEngineering, University of California, San Diego, 9500 Gilman Drive, MC 0448, La Jolla, CA 92093-0448, USA

E-mail: dlipomi@ucsd.edu

Received 16 September 2014, revised 28 October 2014
Accepted for publication 3 November 2014
Published 5 January 2015

Abstract

Graphene is expected to play a significant role in future technologies that span a range from consumer electronics, to devices for the conversion and storage of energy, to conformable biomedical devices for healthcare. To realize these applications, however, a low-cost method of synthesizing large areas of high-quality graphene is required. Currently, the only method to generate large-area single-layer graphene that is compatible with roll-to-roll manufacturing destroys approximately 300 kg of copper foil (thickness = 25 μm) for every 1 g of graphene produced. This paper describes a new environmentally benign and scalable process of transferring graphene to flexible substrates. The process is based on the preferential adhesion of certain thin metallic films to graphene; separation of the graphene from the catalytic copper foil is followed by lamination to a flexible target substrate in a process that is compatible with roll-to-roll manufacturing. The copper substrate is indefinitely reusable and the method is substantially greener than the current process that uses relatively large amounts of corrosive etchants to remove the copper. The sheet resistance of the graphene produced by this new process is unoptimized but should be comparable in principle to that produced by the standard method, given the defects observable by Raman spectroscopy and the presence of process-induced cracks. With further improvements, this green, inexpensive synthesis of single-layer graphene could enable applications in flexible, stretchable, and disposable electronics, low-profile and lightweight barrier materials, and in large-area displays and photovoltaic modules.

S Online supplementary data available from stacks.iop.org/NANO/26/045301/mmedia

Keywords: graphene, transparent electrode, roll-to-roll processing, green nanofabrication, CVD, flexible electronics

(Some figures may appear in colour only in the online journal)

1. Introduction

The only current method for growing large-area single-layer graphene that is compatible with roll-to-roll manufacturing is highly wasteful [1]. Efforts to reduce this waste have been driven by two goals. The first goal is to reduce the cost and environmental impact for relatively high-end applications—i.e., nanoelectronics [2, 3] and transparent electrodes [4]—for which graphene is currently regarded as an important future component. The second goal is to enable potential applications—i.e., disposable electronics [5], textiles [6, 7], conformable biomedical devices [8], and thin-film photovoltaic modules [9, 10] (which will need to cover thousands of square kilometers)—that would be difficult to realize using graphene at its current cost. In the well-known, roll-to-roll-compatible process originally described by Bae *et al*, single-

0957-4484/15/045301+07$33.00

layer graphene was grown on large-area copper foils by chemical vapor deposition (CVD) and released onto a carrier substrate by chemical etching of the copper [4]. This process is significant in its ability to produce films over relatively large areas, but the cost of a one-atom-thick layer of graphene includes the destruction of an equal area of a 10^5-atom-thick copper foil, along with the economic costs and environmental externalities associated with preparing the copper substrates for synthesis and handling large amounts of corrosive waste.

There exists another issue that precludes the manufacturing of graphene on an industrial scale besides the high costs of graphene production. Generating sufficient amounts (square kilometers) of graphene the industries that can best utilize its properties—as a barrier material or as a transparent conductive electrode—requires a robust process capable of high production yields. The production rate for the above-mentioned process is limited by the need to prepare each batch of copper foil prior to graphene synthesis (extensive cleaning, electropolishing, and annealing) as well as the need for the prolonged etching of the copper foil in order to liberate graphene. Both steps amount to more than an hour of additional processing time for a given batch, besides significantly adding to the cost of the product. Reusing the copper substrate by non-destructive removal of graphene from its surface would not only substantially increase the attainable production rate by removing the necessity of priming and etching the copper substrates, but would also make it possible to double the graphene yield per batch due to the ability to remove graphene on both surfaces of the foil. This paper describes a process that is amenable to large-area production of single-layer graphene by mechanical exfoliation. We believe the process could be performed at rates of production that are required for manufacturing.

2. Experimental design

Our process is based on the differential adhesion of graphene to various metals, subsequent mechanical exfoliation, and lamination to a flexible substrate using a thermally deactivated adhesive (each step of the process is depicted in figure 1). We have nicknamed the process metal-assisted exfoliation—'MAE'. A similar technique has been previously used to exfoliate graphene from single-crystalline wafers [11] bearing hydrogen-terminated germanium using gold as the 'adhesive' metal [12] but to our knowledge such attempts have been limited to graphene transferred from the perfect surfaces of wafers and to their dimensions, and this is the first time that MAE is demonstrated for graphene grown on copper. The process appears to be applicable to large-area (limited by the reactor and metallization chamber dimensions) graphene transfer from relatively rough surfaces. In brief, single-layer graphene was grown on a copper foil by ambient-pressure CVD (step 1). A 150 nm film of nickel (or cobalt) was deposited on the graphene by physical vapor deposition (step 2 and figure 2(a)). Thermal release tape was applied (step 3 and figure 2(b)); peeling up the thermal release tape exfoliated the metal/graphene bilayer films from the copper substrate (step 4 and figure 2(c)), which was reusable without further treatment. Lamination of the graphene to a commercial polyethyelene terephthalate (PET) substrate, bearing a thermoplastic adhesive coating, at 100 °C deactivated the adhesive on the thermal release tape, and the graphene remained on the plastic substrate (step 5 and figures 2(d), (e)). The sheet containing PET/graphene/metallic film was then dipped into the bath containing a metal etchant solution for 3–5 s (step 6 and figure 2(f)) and rinsed in deionized water to yield a sheet of PET covered with single-layer graphene (step 7 and figures 2(g) and (h)).

Even though vacuum metallization techniques are generally perceived in academia as being costly, such techniques have been used for many decades to produce thousands of square kilometers of such commodities as potato-chip bags, magnetic tapes, capacitors and optical films. Such systems reach web-speeds of meters per second, deposition rates of hundreds of micrometers per minute, and annual production of millions of square meters [13]. Additionally, alternative, ambient pressure graphene metallization techniques such as nickel electro(less)-deposition that could further increase the production rate and decrease its cost are currently under investigation.

The final receiving substrate—PET—was selected for its widespread use in flexible electronics. Additionally, the commercially available PET films used in the lamination process bear a thermoplastic layer that adheres well to graphene and facilitates its transfer from the thermal release tape. We successfully exfoliated graphene from the copper foil using thin films of nickel, cobalt, and gold. A comparative density-functional study of the binding energies between graphene and various metal surfaces by Hamada and Otani revealed a stronger preference of graphene to nickel (141 meV) than to copper (62 meV) [14]. The strong adhesion of nickel to graphene was also exploited by Kim *et al* in a two-step exfoliation of graphene from SiC surfaces, but this process is not likely to be compatible with roll-to-roll manufacturing, because of the inflexibility of the SiC wafers [15]. In addition to the metals listed above, we also attempted MAE with iron and aluminum, but found they did not exhibit preferential adhesion to graphene and thus did not enable exfoliation of graphene from the copper substrate. Of the three metals that enabled exfoliation, only nickel and cobalt could be etched without damaging the graphene (i.e., by etching it or rendering it non-conductive). For example, etching gold with the standard solution containing iodine and potassium iodide rendered the graphene non-conductive.

3. Results and discussion

To determine the quality of the graphene transferred by our method, we measured the sheet resistance (R_s) and the ratio of the D/G peak from the Raman spectra. We obtained values of R_s that varied within an order of magnitude between samples. We attribute the variability, in part, to the manual nature of the transfer of the nickel/graphene or cobalt/graphene bilayer films to the thermal release tape and the subsequent

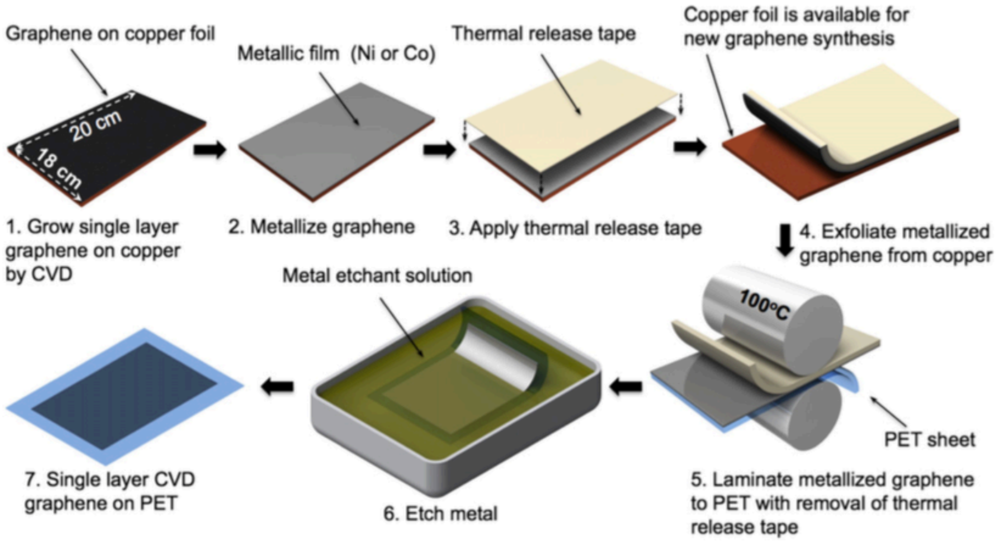

Figure 1. Summary of the MAE process: large-area transfer of single-layer graphene from catalytic copper substrates to PET sheets. The process is based on preferential adhesion of nickel (or cobalt) to graphene, exfoliation, and lamination mediated by tape with a thermally deactivated adhesive.

mechanical damage to the film due to the hot-press lamination of the composite to PET at 100 °C. The lowest value of R_s we obtained was $163\,\Omega\,\text{sq}^{-1}$ compared to the lowest value of $325\,\Omega\,\text{sq}^{-1}$ obtained from graphene transferred using the standard method in which the copper was etched. This low observed resistance is possibly due to doping of the graphene surface with metals (nickel, iron) or their chlorides [16], as we did not perform any other post-processing of the MAE transferred graphene following the etching of the nickel film in iron (III) chloride besides rinsing in deionized water (three times, 5 min each). We also observed cracks in the nickel film after exfoliation (figures 2(c), 3), which we attribute, again, to the manual nature of the exfoliation step, along with the inability of the nickel or cobalt film to accommodate the tensile strain imposed on it during the peeling process. These cracks, which probably propagated through the graphene (figure 2(h)), produced an anisotropic sheet resistance; the average R_s measured parallel to the cracks ($850 \pm 250\,\Omega\,\text{sq}^{-1}$) was an order of magnitude lower than when measured perpendicular to the cracks ($8000 \pm 2000\,\Omega\,\text{sq}^{-1}$). The cracks formed mostly orthogonally to the peeling direction with their density highest at the starting point of the exfoliation (about three cracks per mm), where the radius of curvature of the films was the smallest and the metallic films were subject to greatest tensile stress, to the average of 0.7 cracks per mm throughout the major area of the film, where the radius of curvature was mostly constant throughout the process of exfoliation. It is important to note that the formation of cracks is not intrinsic to the MAE and can be mitigated. For example, relatively large areas of metallized graphene can be exfoliated directly, without additional supporting films or other structures. Such exfoliated films tend to scroll up due to the inherent stresses in evaporated thin films and are difficult to handle but display no cracking behavior over the entire observed area (about 1 cm^2). The absence of cracking can be explained by the thinness of the films sandwich as compared to that where the films are supported by thermal release tape. Being about 1000 times thinner, the freestanding films allow 1000 times smaller bending radii. An automated process, where the metallized graphene film is subject to reduced tensile strain by using rollers with large radii of curvature, or by using a stiffer adhesive, should reduce the occurrence of cracking or help avoid it altogether. It is possible that kinetically controlled transfer printing by a reusable stamp, as described by Rogers and coworkers, would permit transfer without using thermal release tape [17].

The metal thickness of 150 nm was found to be optimal for the MAE process as it supported complete graphene removal while being thin enough to allow fast processing times. Thicknesses of 10, 20, and 50 nm achieved partial to complete graphene removal from copper but appeared to not be robust enough for the MAE process and resulted in severely degraded transferred films. Thicker films of 1 and 2 μm (150 nm were evaporated and 850 and 1850 nm were electroplated) were also explored. While these thick films made direct (unsupported) exfoliation of metallized graphene from copper more productive (greater areas of graphene could be peeled off with tweezers), the large-area MAE transfer utilizing these films still produced the anisotropic cracking, albeit of a lower density (~0.3 cracks per mm).

The Raman spectra of the graphene as grown on copper and after exfoliation are shown in figures 4(a) and (b). The spectra reveal the complete removal of graphene from copper in the exfoliated region as also supported by optical microscopy studies of the residual material on copper (figure 6(d)). To determine the capacity of a given metal to support MAE of

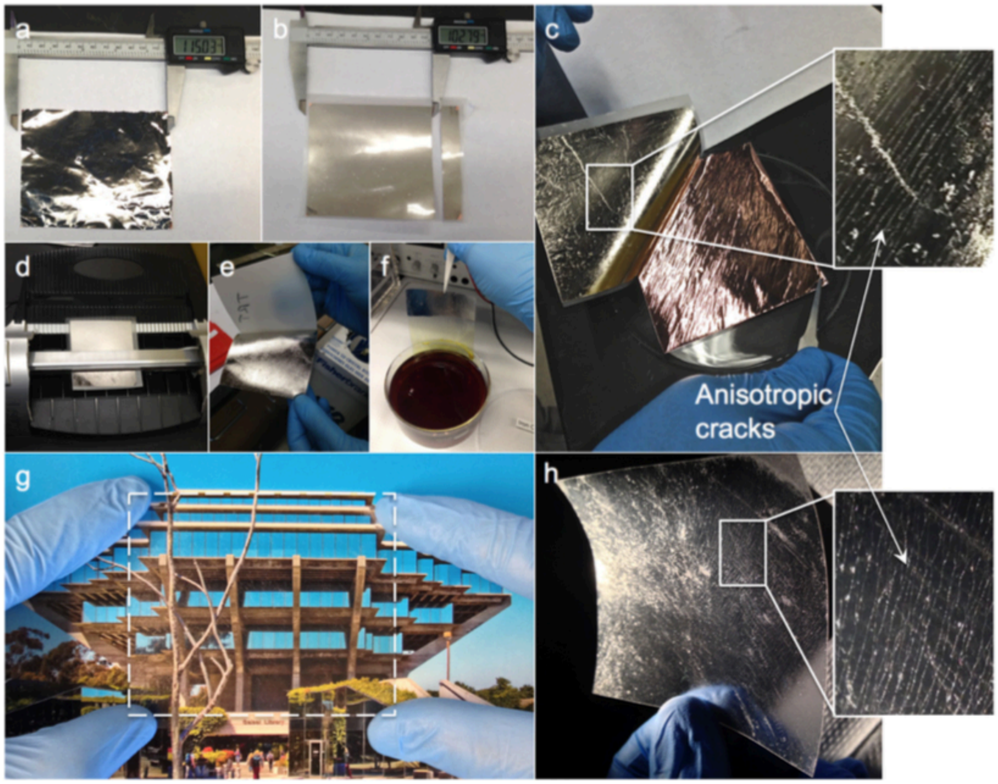

Figure 2. Photographs of the consecutive steps of the MAE of graphene. Single layer graphene on a copper foil after: (a) metallization with nickel, (b) application of thermal release tape, (c) peeling metallized graphene off of the copper foil, (d) lamination of a PET sheet to the metallized graphene (with concomitant deactivation of the thermal release tape), (e) removal of the thermal release tape from the PET/graphene/nickel sheet, (f) dipping the PET/graphene/nickel sheet into the iron (III) chloride solution (3–5 s). The PET sheet coated with single-layer graphene (g) is shown against a postcard depicting the UCSD Geisel library (the outline of the PET/graphene sheet is indicated by the dashed rectangle). An image (h) is also shown of the PET/graphene sheet illuminated at a grazing angle to highlight the cracks that form perpendicular to the peeling of the thermal release tape/metallic film/graphene sheet from the copper foil (shown in detail in the insets of (c) and (h)).

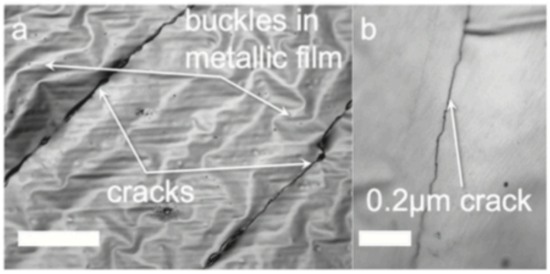

Figure 3. Optical micrograph of cracks in the nickel film after MAE of graphene from copper at 200× magnification ((a), scale bar 100 μm) and at 1000× magnification ((b), scale bar 10 μm). The cracks range in width from tens of nanometers to 1.5 μm.

graphene from copper, we compared the spectra of the metallic films of gold, cobalt, and nickel after exfoliation of graphene (figures 4(c), (e), and (g)) to the spectra of the respective bare metallic films (figures 4(d), (f), and (h)). The appearance of the peaks characteristic of graphene (D, G, and 2D, highlighted in yellow) on the spectra (figures 4(c), (e), and (g)) revealed the presence of graphene on the films after exfoliation; this observation demonstrated the removal of graphene from copper. We noticed that graphene exfoliated with gold (figure 4(c)) exhibited a smaller D peak than that of graphene transferred with cobalt and nickel (figures 4(e), (g)); this observation suggests that gold is less damaging to graphene, possibly because of the chemical inertness of gold. Figure 5 provides a direct comparison of the defects present in the graphene produced by the prevailing method of wet-transfer described by Bae *et al* to that produced by the MAE process [4]. To obtain these spectra, the graphene produced by both processes was laminated to a Si/SiO$_2$ substrate. For the traditional wet-transfer, this was achieved by spin-coating poly(methylmethacrylate) (PMMA) on top of graphene and etching the copper substrate. For the Raman spectroscopy of the MAE sample, epoxy was cured on top of the metallized graphene and it was then peeled off of the copper foil. We then spin-coated PMMA on top of the exposed surface of graphene and etched the underlying nickel film in FeCl$_3$. The

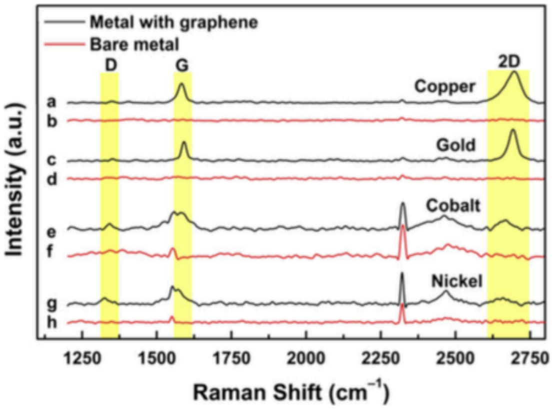

Figure 4. Representative Raman spectra of graphene 'as grown' on copper foil (a), copper foil after metal-assisted graphene exfoliation (b) (no graphene peaks indicate a complete graphene removal from the copper foil), graphene on metallic films transferred by MAE from copper ((c), (e), (g)) and the pure metal films respectively ((d), (f), (h)) (gold and copper substrates significantly enhance the Raman scattering and produce strong, well-defined graphene peaks—highlighted in yellow—as compared to cobalt and nickel). The baseline in the spectra has been 'flattened' by curve-fitted subtraction.

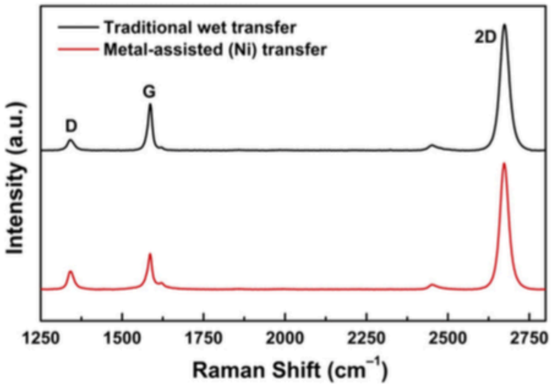

Figure 5. Raman spectra of graphene transferred to Si/SiO$_2$ by traditional wet-transfer method (black) and metal-assisted (Ni) method (red).

freestanding graphene/PMMA was then transferred to DI water three times before applying it to the Si/SiO$_2$ wafer chip. The PMMA was then removed by submersion in a boiling acetone bath.

The quality of graphene was judged on the basis of the ratio of the D/G (at 1330 cm^{-1} and 1580 cm^{-1}) and 2D/G peaks (at 2700 cm^{-1} and 1580 cm^{-1}) in the Raman spectra [18]. The observed 2D/G ratio of our graphene was equal to or greater than 2.8 for all measurements; this ratio is consistent with the presence of single layer graphene [18]. Compared to the traditional wet-transfer process, the D/G peak ratio in the MAE process was increased by a factor of two (from 0.23 for wet-transfer to 0.50 for MAE). It is possible that the increase in the D-peak in the graphene transferred by the MAE process is due to damage during the electron-beam evaporation of the nickel film, mechanical damage during the metal-assisted exfoliation, as well as damage during the following wet-transfer process. We expect that other metallization techniques such as electro- or electroless deposition of nickel could be less damaging to the graphene.

The environmental benignity of the MAE process is predicated on the reusability of the copper foil used to grow the graphene. To determine the impact of reusing the same copper substrate on the growth of graphene, we investigated the quality of the graphene grown on copper after cyclic growth and transfer. Remarkably, the quality of the graphene increased after successive cycles of growth (figures 6(a)–(c), (e)). We hypothesize that the increase in quality might be because of the additional annealing of the copper substrate during each cycle of graphene synthesis as well as the removal of surface contaminants with each metal-assisted graphene exfoliation, which produced a cleaner surface for subsequent growth (after each graphene exfoliation, the copper foil substrate was immediately placed into the CVD reactor chamber under high vacuum to avoid contamination of the surface).

In order to demonstrate that the MAE process completely exfoliates graphene from the copper foil, all material remaining on the copper foil after exfoliation of graphene was transferred onto a Si/SiO$_2$ wafer using the traditional wet-transfer process for optical microscopy (figure 6(d)). Also, the Raman spectra taken on the copper surface immediately after the MAE revealed no graphene peaks (figure 4(b)). The presence of only sporadic, small residual individual graphene grains on the copper foil following MAE indicates that this process transfers predominantly the continuous top (metallized) layer of graphene and supports the theory that small patches of a second graphene layer form beneath the first layer during graphene growth on copper by CVD [19, 20]. Additionally, it is possible that these residual graphene grains serve as 'seed grains' for the subsequent cycle of growth. It has been shown in literature that best quality CVD graphene on copper is obtained by 'pre-seeding' graphene grains on the copper surface prior to graphene synthesis [21].

The principal advantage of the MAE process is that the copper foil is reusable indefinitely which should ultimately translate into decreased production of chemical waste. To illustrate this point, we made qualitative comparisons of the costs and environmental impacts of the MAE process to those of the conventional wet-etch method. The wholesale cost of copper on the global market is on the order of \$10 kg^{-1} [22], but research quantities of copper foil are obtained for costs around 100 times higher [23]. The production energy of copper is 64 MJ kg^{-1} [24], which translates to about 13 kg CO$_2$ emissions per kg of copper, using the current rate of generation in the US of 0.2 kg CO$_2$ MJ^{-1} [25]. The MAE process can reuse the ~25 μm thick copper foil indefinitely, while the prevailing wet-etch method destroys it. While the MAE process does involve the etching of nickel (or cobalt), the MAE process etches two hundred times less metal than does the wet-etch method. We also expect that metallization

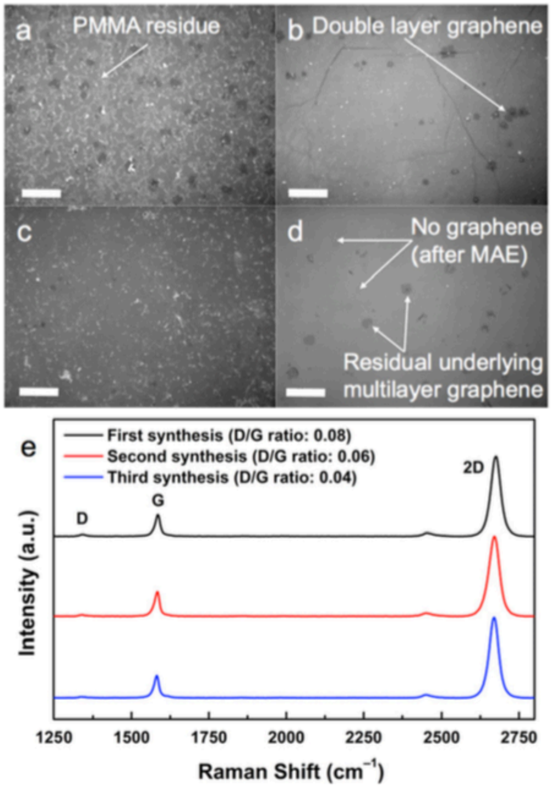

Figure 6. Optical micrographs of graphene transferred onto a Si/SiO$_2$ wafer from the same copper foil substrate after the first (a), second (b), and third (c) syntheses using the traditional wet-transfer method (scale bar 20 μm). Each consecutive synthesis after the transfer of graphene via nickel evaporation produced cleaner, better quality graphene. That is, the number of multilayer regions, which appear in the images as darker spots, decreased significantly from (a) to (c). We note that the white contamination visible in (a)–(c) is residual PMMA that could not be removed in the boiling acetone bath. Panel (d) represents the residual graphene grains (previously multilayer regions) on the copper substrate after exfoliation of graphene in the MAE process. (e) Raman spectra of the transferred graphene also indicated an improvement in quality upon consecutive synthesis of graphene on the same substrate (the D/G peak ratio decreased from 0.08 in the first growth to 0.04 in the third growth).

can be performed inexpensively (and with little waste) in a roll-to-roll manner as is done for metallized plastic foils for food packaging (e.g., potato chip bags) or under ambient conditions by electrodeposition. Moreover, the time it takes to etch the 150 nm nickel film completely is 3–5 s, whereas the time to etch the copper foil is at least 30 min. By avoiding the need for the preparation of the copper substrates after the first synthesis, the savings in time with the MAE process make it substantially more amenable to manufacturing than the conventional method. Additionally, while nickel and copper were etched with toxic FeCl$_3$ for convenience in the experiments described here, we expect that the FeCl$_3$ can be replaced with a more recyclable alternative such as ammonium persulfate (APS). Possible improvements in scalability include replacing the thermal release tape, which is convenient for laboratory-scale experiments, by another adhesion control mechanism: electrostatic, magnetic, or kinetically controlled stickion; for example with poly(dimethylsiloxane) (PDMS) stamps, which we have found can also exfoliate the graphene/nickel bilayer from the copper foil, and thus can probably redeposit the bilayer on a target substrate by kinetically controlled transfer printing.

4. Conclusion

We have developed a green, facile, and roll-to-roll compatible method for transferring large-area single-layer graphene to flexible substrates. With further improvements, the process has the capacity to produce films of similar quality to that of the prevailing method, which destroys an outsized amount of copper foil. Shortcomings in the current process include the anisotropic conductivity that is a consequence of manual peeling of the tape/nickel/graphene film from the copper substrate (step 3 in figure 1). This process has important implications for laboratory researchers, and for applications that demand very large areas of transparent electrodes or barrier films (e.g., solar farms based on organic or other thin-film technologies) due to the high production rates attainable with it through time, mass, and energy savings as well as reduced environmental impact and increased yield per batch. As compared to the traditional wet-etching process, MAE saves more than 60 min per batch (except the first run) by eliminating copper preparation steps (cleaning, electropolishing, annealing) and wet etching. Time required for Ni metallization and etching is negligible (seconds) considering that it is an industrial scale metallization process. Mass savings are due to the 188 times reduction in metal consumption (for 25 μm thick copper and 150 nm thick nickel) and energy savings are associated with removing the need to anneal foils for at least 30 min at more than 1000 °C prior to the synthesis of graphene. The 155 times reduction in the required corrosive waste handling represents a significantly lesser environmental impact. The yields per batch can be doubled in the MAE process due to harvesting graphene from both foil surfaces. Since the copper substrates are not etched in MAE, the robustness of the process can be significantly increased by using thicker, sturdier and more manageable copper foils (or plates) that will better withstand being repeatedly subjected to the high-temperature environment of the graphene synthesis chamber. We believe, furthermore, that a substantial decrease in the cost of large-area graphene will stimulate the development of applications that require very low cost—but high performance—graphene-enabled materials [26].

Acknowledgments

This work was supported by the laboratory startup funds from the University of California, San Diego. Some aspects were supported by the Air Force Office of Scientific Research (AFOSR) Young Investigator Program, grant number

FA9550-13-1-0156. AZ acknowledges a fellowship from SoCal Clean Energy Technology Acceleration Program from the von Liebig Center at UCSD sponsored by the US Department of Energy. SS acknowledges support provided by the National Science Foundation Graduate Research Fellowship under Grant No. DGE-1144086. HM acknowledges support provided by the Calit2-Qualcomm Institute Summer Undergraduate Research Scholars program. EV acknowledges support provided by the Ronald McNair Program. We gratefully acknowledge Prof. Richard Kaner and Jaime Torres for providing materials in the early stages of this project.

Supporting information available

The online supporting information contains complete experimental protocols. This information is available free of charge via the Internet at pubs.acs.org.

References

[1] Coleman K and Edwards R S 2013 Graphene synthesis: relationship to applications *Nanoscale* **5** 38–51

[2] Van Der Zande A M, Barton R A, Alden J S, Ruiz-Vargas C S, Whitney W S, Pham P H Q, Park J, Parpia J M, Craighead H G and McEuen P L 2010 Large-scale arrays of single-layer graphene resonators *Nano Lett.* **10** 4869–73

[3] Schwierz F 2010 Graphene transistors *Nat. Nanotechnology* **5** 487–96

[4] Bae S *et al* 2010 Roll-to-roll production of 30-inch graphene films for transparent electrodes *Nat. Nanotechnology* **5** 574–8

[5] Song W, Li D W, Li Y T, Li Y and Long Y T 2011 Disposable biosensor based on graphene oxide conjugated with tyrosinase assembled gold nanoparticles *Biosens. Bioelectron.* **26** 3181–6

[6] Yu G, Hu L, Vosgueritchian M, Wang H, Xie X, McDonough J R, Cui X, Cui Y and Bao Z 2011 Solution-processed graphene/MnO2 nanostructured textiles for high-performance electrochemical capacitors *Nano Lett.* **11** 2905–11

[7] Meng Y, Zhao Y, Hu C, Cheng H, Hu Y, Zhang Z, Shi G and Qu L 2013 All-graphene core-sheath microfibers for all-solid-state, stretchable fibriform supercapacitors and wearable electronic textiles *Adv. Mater.* **25** 2326–31

[8] Zhang Y, Nayak T R, Hong H and Cai W 2012 Graphene: a versatile nanoplatform for biomedical applications *Nanoscale* **4** 3833

[9] Ramuz M P, Vosgueritchian M, Wei P, Wang C, Gao Y, Wu Y, Chen Y and Bao Z 2012 Evaluation of solution-processable carbon-based electrodes for all-carbon solar cells *ACS Nano* **6** 10384–95

[10] Liu Z, Li J and Yan F 2013 Package-free flexible organic solar cells with graphene top electrodes *Adv. Mater.* **25** 4296–301

[11] He Y, Chen W F, Yu W B, Ouyang G and Yang G W 2013 Anomalous interface adhesion of graphene membranes *Sci. Rep.* **3** 2660

[12] Lee J-H *et al* 2014 Wafer-scale growth of single-crystal monolayer graphene on reusable hydrogen-terminated germanium *Science* **344** 286–9

[13] Jon P, Schiller S, Jaesch G, Neumann M and Manjiied F 1983 High rate electron beam evaporation *Thin Solid Films* **110** 149–64

[14] Hamada I and Otani M 2010 Comparative van der Waals density-functional study of graphene on metal surfaces *Phys. Rev. B—Condens. Matter Mater. Phys.* **82** 153412

[15] Kim J, Park H, Hannon J B, Bedell S W, Fogel K, Sadana D K and Dimitrakopoulos C 2013 Layer-resolved graphene transfer via engineered strain layers *Science* **342** 833–6

[16] Kwon K C, Choi K S and Kim S Y 2012 Increased work function in few-layer graphene sheets via metal chloride doping *Adv. Funct. Mater.* **22** 4724–31

[17] Meitl M A, Zhu Z-T, Kumar V, Lee K J, Feng X, Huang Y Y, Adesida I, Nuzzo R G and Rogers J A 2006 Transfer printing by kinetic control of adhesion to an elastomeric stamp *Nat. Mater.* **5** 33–8

[18] Ferrari A C *et al* 2006 Raman spectrum of graphene and graphene layers *Phys. Rev. Lett.* **97** 187401

[19] Nie S, Wu W, Xing S, Yu Q, Bao J, Pei S S and McCarty K F 2012 Growth from below: bilayer graphene on copper by chemical vapor deposition *New J. Phys.* **14** 093028

[20] Li Q, Chou H, Zhong J H, Liu J Y, Dolocan A, Zhang J, Zhou Y, Ruoff R S, Chen S and Cai W 2013 Growth of adlayer graphene on Cu studied by carbon isotope labeling *Nano Lett.* **13** 486–90

[21] Yu Q *et al* 2011 Control and characterization of individual grains and grain boundaries in graphene grown by chemical vapor deposition *Nat. Mater.* **10** 443–9

[22] Trade Service 2014 *Daily Report: Copper Pricing 2014* (accessed 20 May 2014) (www.tradeservice.com/copper_pricing)

[23] Alfa Aesar 2014 13392 Copper foil, 0.025 mm (0.001in) thick, annealed, coated, 99.8% (metals basis) (accessed 20 May 2014) (www.alfa.com/en/catalog/13382)

[24] Williams E D, Ayres R U and Heller M 2002 The 1.7 kilogram microchip: energy and material use in the production of semiconductor devices *Environ. Sci. Technol.* **36** 5504–10

[25] Environmental Protection Agency 2014 *EPA Clean Energy Calculations and References* (accessed 20 May 2014) (www.epa.gov/cleanenergy/energy-resources/refs.html)

[26] Geim A K and Novoselov K S 2007 The rise of graphene *Nat. Mater.* **6** 183–91

Chapter 3

Using the Thickness of Graphene to Template Lateral Subnanometer Gaps between Gold Nanostructures

Aliaksandr V. Zaretski, Brandon C. Marin, Herad Moetazedi, Tyler J. Dill, Liban Jibril,
Casey Kong, Andrea R. Tao, and Darren J. Lipomi

Department of NanoEngineering, University of California, San Diego
9500 Gilman Drive, Mail Code 0448, La Jolla, CA 92093-0448

NANO LETTERS

Letter

pubs.acs.org/NanoLett

Using the Thickness of Graphene to Template Lateral Subnanometer Gaps between Gold Nanostructures

Aliaksandr V. Zaretski, Brandon C. Marin, Herad Moetazedi, Tyler J. Dill, Liban Jibril, Casey Kong, Andrea R. Tao, and Darren J. Lipomi*

Department of NanoEngineering, University of California, San Diego, 9500 Gilman Drive Mail Code 0448, La Jolla, California 92093-0448, United States

Supporting Information

ABSTRACT: This work demonstrates the use of single-layer graphene as a template for the formation of subnanometer plasmonic gaps using a scalable fabrication process called "nanoskiving." These gaps are formed between parallel gold nanowires in a process that first produces three-layer thin films with the architecture gold/single-layer graphene/gold, and then sections the composite films with an ultramicrotome. The structures produced can be treated as two gold nanowires separated along their entire lengths by an atomically thin graphene nanoribbon. Oxygen plasma etches the sandwiched graphene to a finite depth; this action produces a subnanometer gap near the top surface of the junction between the wires that is capable of supporting highly confined optical fields. The confinement of light is confirmed by surface-enhanced Raman spectroscopy measurements, which indicate that the enhancement of the electric field arises from the junction between the gold nanowires. These experiments demonstrate nanoskiving as a unique and easy-to-implement fabrication technique that is capable of forming subnanometer plasmonic gaps between parallel metallic nanostructures over long, macroscopic distances. These structures could be valuable for fundamental investigations as well as applications in plasmonics and molecular electronics.

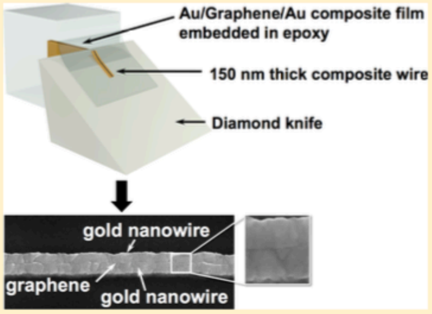

KEYWORDS: *Subnanometer gap, nanogap, graphene nanoribbon, ultramicrotomy, nanoskiving, SERS*

Nanoscale gaps formed by parallel metallic structures with extremely small separation distances are highly desired structures in optics and electronics. When irradiated with light, such structures are capable of producing enormous electromagnetic field enhancements by confining the optical field to the subnanometer gap. This near-field response is the basis of analytical spectroscopy techniques such as surface-enhanced Raman scattering (SERS).[1] Nanogaps are also an enabling component of molecular electronics in which the metallic surfaces that define the dimensions of the nanogap behave as electrodes.[2] A major obstacle in the fabrication of these nanogaps is the ability to template metal deposition with subnanometer precision. Standard lithographic methods (including electron-beam lithography and photolithography) reach a limit of resolution nearing 10 nm.

This letter describes the fabrication of a nanogap using a single layer of graphene as a template. Ultramicrotome sectioning,[3−6] or "nanoskiving," of gold/graphene/gold sandwiches embedded in epoxy can be carried out to form structures comprising two gold nanowires separated by a graphene nanoribbon (Figure 1). Given that carbon is the seventh-smallest element and has a van der Waals radius of only 0.185 nm, we believe that the nanogaps formed in our nanoskiving process are the smallest gaps that are physically possible to achieve by templating. Moreover, this simple method can in principle produce thousands of quasi-copies of a single embedded structure by automated sectioning.[7] The nanogap structures produced by nanoskiving could find a broad range of application in devices where nanoscale gaps play a critical role, such as SERS sensing, molecular electronics,[2] and metamaterials.[8]

Conventional methods of nanofabrication are generally expensive and usually require access to a cleanroom. Progress in understanding the behavior of materials at small length scales could be accelerated by simple techniques that use tools to which most researchers already have access. Moreover, scanning-beam techniques are slow and serial, and are most adept at producing low-aspect-ratio structures of single materials in a single step. Electron-beam lithography (EBL) cannot generate gaps smaller than a few nanometers, and focused-ion-beam (FIB) lithography is known to contaminate structures with the ions used for milling and thus is problematic in some optical applications.[9] Soft lithography,[10] nanoimprint lithography,[11,12] dip-pen nanolithography,[13] and processes that rely on self-assembly are relatively simple techniques that can

Received: October 27, 2014
Revised: December 26, 2014
Published: January 2, 2015

DOI: 10.1021/nl504121w
Nano Lett. 2015, 15, 635−640

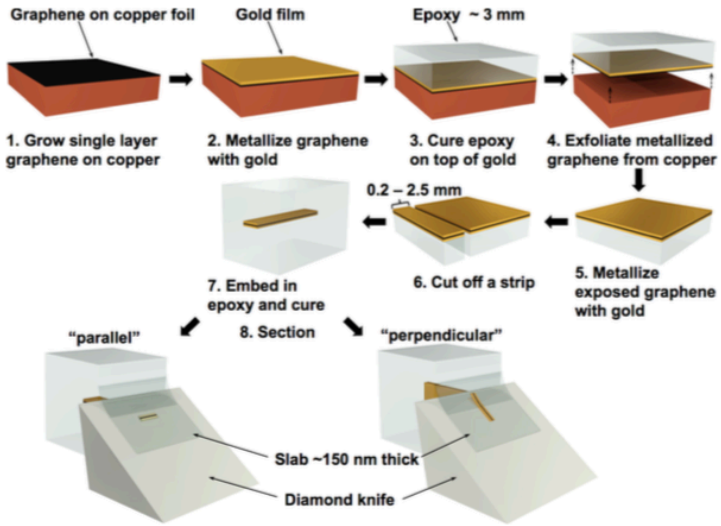

Figure 1. Summary of the process of fabricating subnanometer graphene-templated gaps between gold nanowires using ultramicrotomy (nanoskiving). The process is based on the metal-assisted exfoliation (MAE) of graphene from the copper substrate, metallization of both the top and bottom surfaces of the graphene, and ultrathin sectioning of the gold/graphene/gold composite films.

master and replicate structures, but forming nanoscale, or subnanoscale, gaps remains a particular challenge.

Nanoskiving is the nickname given to the use of ultramicrotome sectioning for the purposes of nanofabrication.[6] The ultramicrotome is a mechanical cutting tool that uses a single-crystal diamond blade to section samples of materials into slabs as thin as 20 nm for examination by electron microscopy. Nanoskiving is a form of edge lithography.[14,15] That is, it converts a structure (e.g., a film) that is thin in the vertical dimension to one that is thin in the lateral dimension. Recently, Pourhossein et al. created nanoscale gaps between gold electrodes by sectioning gold/molecule/gold trilayer structures with an ultramicrotome.[16] In that work, the thickness of a self-assembled monolayer (SAM) of alkanethiolates immobilized on the gold surface determined the width of the gap. Using this method, the authors were able to measure the current density through molecular tunnel junctions ≤5 nm thick. We reasoned that by using the thickness of a planar molecule, it should be possible to fabricate subnanometer gaps in a controlled manner. Nanoskiving is capable of producing laterally arranged, high-aspect-ratio structures comprising multiple materials in the same plane that would be difficult or impossible to fabricate using conventional tools.[5] The technique has been particularly useful for fabricating arrays of closed or open loops for optical applications.[17] The fabrication of nanometer or subnanometer gaps by nanoskiving could enable fundamental studies such as determination of the effect of quantum tunneling on surface-enhanced Raman scattering (SERS).[1]

Our group recently described a technique of synthesizing single-layer graphene by chemical vapor deposition and depositing it on a range of substrates in a way that does not require etching of the copper growth substrate.[18] The method, metal-assisted exfoliation (MAE), uses the high adhesion of certain metals such as nickel, gold, and cobalt to graphene to strip graphene from the copper substrate on which it is grown.[18] Figure 1 summarizes the procedure we developed in this letter, which combines the MAE process with nanoskiving. The MAE process produces high-quality graphene sheets that are intact over large areas. It also ensures intimate contact of graphene with both gold films and minimizes contamination of the interfaces and the occurrence of holes. Throughout the MAE process, the graphene layer is supported by a relatively rigid layer of gold at all times (the graphene is never free-standing). This mechanical support suppresses the occurrence of folds and wrinkles in graphene and thus enforces a separation between the gold layers of 3.4 Å throughout the length of the gold/graphene/gold composite film, and the composite nanowires after they are sectioned.

The final composite structures produced (Figure 1) can be treated as two long parallel gold nanowires longitudinally bisected by a single graphene nanoribbon. There are two extreme relative orientations of the knife with respect to the edge of the embedded film during the sectioning process: one in which the blade is parallel to the edge of the film, and one in which it is perpendicular to the edge of the film. The anisotropy of the cutting process compresses the axis of the epoxy slab parallel to the direction of cutting and leaves the axis perpendicular to the direction of cutting unchanged. The two orientations thus produce different morphologies in the gold/graphene/gold structures in the offcut ("slab") that ultimately affect the yield, the properties of the structures produced, or both.

Composite wires can be obtained reproducibly from either parallel or perpendicular sectioning without substantial defects, other than those imposed by the defects on the diamond knife, but composite wires obtained from perpendicular sectioning were preferable. In perpendicular sectioning, the likelihood of the edge of the gold/graphene/gold composite film coinciding with a defect in the knife is minimal (considering a nondefective or newly sharpened blade). In parallel sectioning, in contrast, the edge of the composite film is exposed to the length of the knife, and thus, defects along the edge of the knife will be transferred to the sectioned structures (i.e., parallel sectioning will produce decreased yields of intact wires if the knife contains damage due to wear). The yield of nondefective wires (not exceeding 1 break per 100 μm of wire) sectioned perpendicularly was close to 100%, while of those sectioned parallel was about 50%. The dimensions of the gold/graphene/gold composite structures were w = 300 nm, h = 150 nm, and l ≈ 500 μm. The width was determined by the thickness of the gold/graphene/gold composite film (two 150 nm thick gold films separated by a single graphene layer). The height was determined by the thickness setting on the ultramicrotome (150 nm here, but 20 nm is possible, Figure S1, Supporting Information), and the length was determined loosely by cutting a large sample into 500 μm wide strips. This dimension is limited by the width of the diamond knife (2.4 mm) in parallel sectioning and by the range of fine sectioning of the ultramicrotome in perpendicular sectioning (~1 cm).

Figure 2 shows scanning electron micrographs of the structures produced by cutting in the perpendicular (Figure 2a) and parallel (Figure 2b) orientations. The microstructure observable in the gold in which grain boundaries run roughly along the transverse axis in the perpendicularly sectioned sample (Figure 2a) are similar to shear lamellae produced in machined metal chips.[19] Compression of embedded films in perpendicular sectioning has previously been associated with a greater number of defects,[6] breaks and thin regions, in the wires per unit length for pure metal films, but we did not observe this effect for the gold/graphene/gold composite films. We attribute the increased mechanical robustness of the gold/graphene/gold films to a reinforcing effect of the graphene layer. Parallel sectioning partially delaminated the gold near the top surfaces of the wires and thus enlarged gaps formed (Figure 2b).

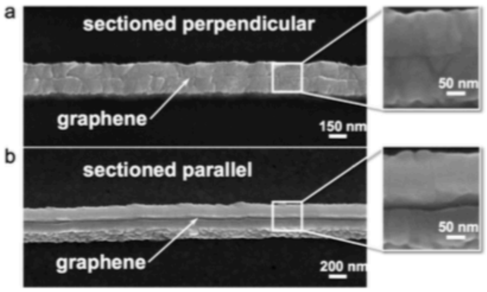

Figure 2. SEM images of gold/graphene/gold composite nanowires: sectioned with blade perpendicular (a) and parallel (b) to the edge of the embedded film. Parallel sectioning was performed top-to-bottom.

To investigate the origin of the dissimilar microstructures between the wires cut in the perpendicular and parallel orientations, we built a finite-element model of the stage in the sectioning process in which the knife first makes contact with the gold/graphene/gold film (Figures S2 and S3, Supporting Information). Compression of the materials during the sectioning process and unequal mechanical properties of the epoxy matrix and the embedded film typically produce a large number of defects; mechanical deformation manifests as breaks and delaminated areas.[20] These defects are due to the uneven distribution of stress; its localization at thin areas and microcracks cause eventual rupture.[21,22] In the case of the gold/graphene/gold composite films sectioned here, sectioning the structure in a perpendicular orientation produced a largely defect-free structure over lengths greater than 100 μm as confirmed by SEM (Figure S4).

We attribute the mechanical resiliency of the gold/graphene/gold composite to the mechanical strength of the graphene. Graphene is known to strengthen significantly thin metallic films composited with it.[23] Such compositing results in an increase of several hundred times in the metal yield strength, which is achieved by blocking the propagation of dislocations across the graphene−metal interface when the compression vector is perpendicular to the interface.[23] The absence of substantial defects in the structures sectioned in the perpendicular geometry suggest that the strengthening effect is also operative when the compressed axis is parallel to the interface. The shear direction during perpendicular sectioning is parallel to the plane of the metal/graphene interface. In this configuration, graphene, which possesses a tensile strength of 1 TPa[24] and good adhesion to gold (~40 meV per carbon atom),[25] reinforces the metal composite longitudinally by accommodating and redistributing the local stresses caused by compression.

Characterization of the composite nanowires by micro-Raman spectroscopy revealed several interesting features. We obtained Raman spectra of both as-sectioned wires (Figure 3a) and those treated by oxygen plasma to remove epoxy and graphene (Figure 3b). The laser had a wavelength of 532 nm with a spot size of 2 μm and was polarized orthogonally to the long axis of the wires. Enhancement by the surface enhanced Raman scattering (SERS) effect permitted the measurement of signals from the small amount of graphene contained within the gold/graphene/gold nanowires. All three of the peaks characteristic of graphene, D, G, and 2D, appeared in the

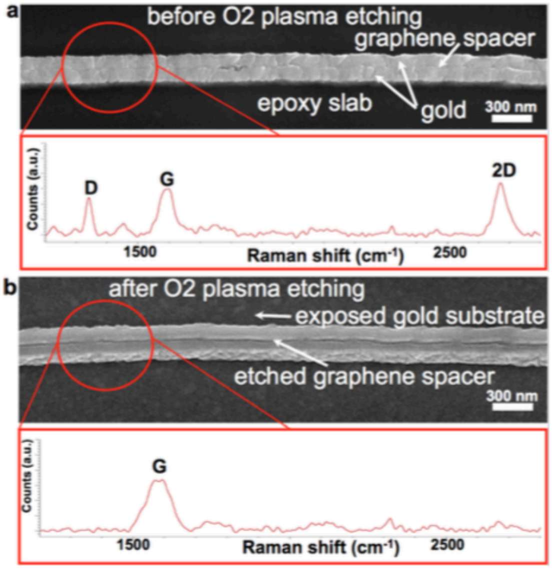

Figure 3. SEM images of the perpendicularly sectioned gold/graphene/gold composite before (a) and after (b) oxygen plasma etching. The insets are the respective Raman spectra. Note the disappearance of D and 2D vibrational modes after plasma etching of exposed graphene. Also, gaps formed in perpendicularly sectioned wires after extensive etching by oxygen plasma. These gaps are similar in width to the gaps mechanically formed in parallel sectioning but result due to the etching of gold along the gold/graphene interface by the oxygen plasma.

spectra of the as-sectioned wire.[26] Notably, there was a substantial increase in relative intensity of the D peak in as-sectioned wires in comparison to spectra obtained from planar single-layer graphene (SLG) on gold (Figure 4a). The D peak arises from transverse optical phonons and specifically requires a lattice defect for the scattering condition to be satisfied. The normalized intensity of this signal has thus been used as a figure of merit for determining the crystalline quality of a graphene film.[27] We attribute the presence of this peak in as-sectioned wires to the strong field enhancement located at the edges of the gold wires, which coincide with the cleaved edge of the graphene. This edge is an extended grain boundary that satisfies the criterion for a scattering event characteristic of the D peak. The peaks labeled D and 2D are characteristic of second-order scattering processes requiring optical phonons that propagate in-plane with graphene[26] but orthogonally with a bond vibration (transverse phonons). These processes differ only in the sense that the D mode requires an initial elastic scattering event by a crystal defect. After a long exposure to oxygen plasma (3 h, 30 W, 200 mTorr), the D and 2D peaks disappeared from the Raman spectra (Figure 3b). We hypothesize that the near-surface graphene was relatively free to vibrate in all modes associated with the D, G, and 2D signals in the Raman spectra. The disappearance of the D and 2D signals, suggesting that second-order transverse processes are forbidden, was possibly the result of confining graphene between the gold wires. In contrast, the G peak, which represents both transverse and longitudinal (in-plane with graphene and along the bond vibration) optical phonon processes, remained after etching. We attributed the persistence of small amounts of graphene between the wires even after extensive exposure to oxygen plasma to the inability of reactive ion species to sufficiently diffuse within the confined geometry of the subnanometer gap (i.e., Knudsen regime effects).[28] Only the graphene near the surface, including any graphene protruding from the gap between the gold nanowires along with that at some depth within the gap, was etched. It is most likely that during and after the oxygen plasma treatment, the edge of the graphene ribbon is decorated with carboxylates and hydroxyl groups. During acquisition of the Raman spectra, these groups are subject to laser irradiation and significant heating. Both these conditions have been previously demonstrated to reduce graphene oxide;[29] hence, it is possible that the obtained Raman spectra are of the reduced form of the graphene edge (gold-reduced or hydrogen-terminated). The splitting of the remaining G-peak, evident in the spectra of the oxygen plasma treated wires, may be attributable to uniaxial strain, either epitaxial or induced by the sectioning process, on the edge of the graphene that remained intact.[30] It is important to note that, to our knowledge, this is the first time a Raman spectrum of graphene has been obtained edge-on, with the incident wave propagating in-plane with graphene (especially after etching away the near-surface graphene).

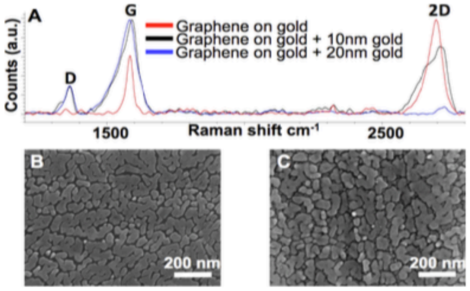

Figure 4. Raman spectra of 150 nm thick gold film/graphene/ultrathin gold film sandwich obtained from planar composite (a). SEM images of gold/graphene/10 nm gold composite (b) and gold/graphene/20 nm gold composite (c).

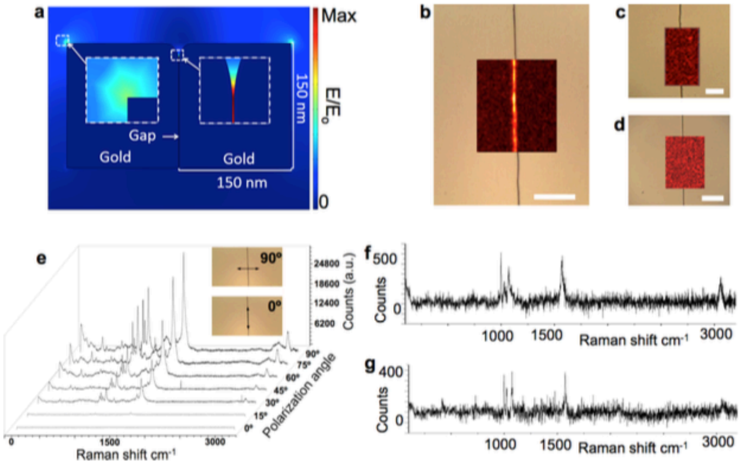

Figure 5. Finite element analysis simulation of the electric field distribution between the gold wires in cross-section (a). Note the significant E-field intensification at the opening of the crack between the wires as compared to that at the corner of the wire (the gap taper was determined by atomic force microscopy (AFM); Figure S5, Supporting Information). Raman map of 1002 cm^{-1} benzenethiol peak of gold/graphene/gold composite wire (b), a 300 nm wide gold wire (c), and a 150 nm wide gold wire (d); scale bars = 8 μm. Dependence of the Raman spectra of benzene thiolate taken from the sectioned wires on the angle of polarization of the laser (e). Raman spectra of benzene thiolate produced by the control samples: 300 nm wide gold wire (f) and 150 nm wide gold wire (g).

To verify that it was in principal possible to etch the graphene completely in the absence of a second gold wire, we sectioned a gold/graphene bilayer. Plasma etching of this structure completely eliminated signals associated with graphene from the Raman spectrum. To determine if confinement of graphene between gold layers was indeed responsible for the disappearance of the D and 2D peaks, we took Raman spectra of the samples where ultrathin layers of gold were evaporated on top of gold-exfoliated graphene films (Figure 4a). We found that deposition of 10 nm of gold onto the exfoliated graphene (Figure 4b) depressed the 2D peak by about a factor of 2, as compared to the G peak. In comparison, the D peak significantly increased, which indicated a more defective structure. This observation has been reported in similar gold−graphene interfaces.[31] Additionally, evaporated thin layers of gold on top of planar graphene formed discontinuous gold islands. Considering the absorption peak of gold in the visible range is very close to 532 nm (the wavelength of excitation),[32] used in the experiment, the islands can absorb the excitation radiation, forming thermal hot spots due to their discontinuous nature. These hot spots potentially cause thermal damage to the underlying graphene and could account for the increased D peak. Evaporation of a thin gold overlayer also produced a blue shift and substantial broadening of the 2D peak (characteristic of a graphitic structure).[26] When 20 nm of gold was evaporated (Figure 4c), the 2D signal reduced substantially in intensity, while the intensity of the D peak remained unchanged. Similar attenuation and line broadening of the 2D mode has also been observed in multilayered graphene.[33] These observations are consistent with the hypothesis that physical confinement of the graphene by gold produced the effects observed in the sectioned samples.

We next investigated the enhancement of the electric field in the gap. Using finite-element analysis (FEA), we modeled the electric field distribution in the cross-section of the composite wire (Figure 5a) in COMSOL. According to the simulation, the gap between the wires had a significantly increased electric field as compared to that at the outside corners of the wires. It is believed that quantum tunneling decreases the electric field in gaps between metallic structures smaller than approximately 1 nm, and thus, subnanometer gaps should significantly reduce the SERS effect.[1] COMSOL software is incapable of taking into account the quantum effects of tunneling; thus, we experimentally determined whether the SERS enhancement originated from the gap or simply from the outside edges of the wires. To test this hypothesis, we formed a self-assembled monolayer (SAM) of benzenethiolate on the exposed surfaces of an oxygen plasma-etched composite wire and two types of control wires: a single solid gold wire with similar dimensions to the composite wires ($h = 150$ nm, $w = 300$ nm, $l = 500$ μm) and a single solid gold wire with dimensions equal to only one of the wires in the composite ($h = 150$ nm, $w = 150$ nm, $l = 500$ μm). All wires were deposited on top of a silicon wafer bearing an evaporated gold film (150 nm) prior to the deposition of the SAM. We then obtained high-precision Raman maps of the spatial distribution of the 1002 cm^{-1} peak (characteristic of benzenethiolate). As seen on the Raman map (Figure 5b), the composite wire produced a well-defined signal that could be overlaid with the long-axis of the wires bearing the nanogap, while the signal originating from the two control solid gold wires were indistinguishable from the background benzenethiolate signal originating from the planar gold substrate (Figures 5c,d).

We also examined the dependence of the intensity of the Raman signals on polarization (Figure 5e). As expected, polarization of the laser beam orthogonal to the long axis of the nanogap generated the strongest signal because of the strong near-field response in the gap between the wires. The strength of the signal originating from benzenethiolate obtained from the composite wire (Figure 5b) was a factor of 50 greater than those obtained from the control wires (Figure 5f,g). This observation suggests that the SERS signal is overwhelmingly dependent on the gap mode of the two wires spaced by graphene, as opposed to the enhancement generated by the outside corners of the wires illustrated in Figure 5a. Similar results were obtained by using 1-butanethiol as the analyte for the SERS study of the gap (Figure S6, Supporting Information).

Conclusions. This letter demonstrated the use of nanoskiving combined with graphene spacers as templates for forming lateral subnanometer gaps reproducibly and with high yields. Composite nanowires fabricated in this fashion produce significantly enhanced SERS signals compared to control samples that did not contain gaps, and this study thus suggests the potential use of such structures in applications for nanoscale optics. Raman spectra of graphene sandwiched by metallic films in both vertical and horizontal orientations were obtained and revealed new details about graphene vibrational modes in such architectures. Varying the orientation of the blade with respect to the embedded films was shown to produce wires with slightly different geometry of the cross-section of the gap. Additionally, compositing metallic films with graphene as the interlayer resulted in reinforcement of the films not only in the lateral but also in the longitudinal direction by significantly increasing the ultimate strength of the metallic films, as shown by the absence of defects in the structures obtained by perpendicular sectioning of the composite wires. It is possible that functionalization of graphene used for templating the nanogaps, or the use of multilayer graphene, could be used to render the methodology amenable to applications in nanoelectronics.

■ ASSOCIATED CONTENT

Supporting Information

Graphene synthesis, metal evaporation, finite-element analysis of the sectioning processes, sample preparation for ultramicrotomy, oxygen plasma etching, and Raman spectroscopic analysis of the structures. This material is available free of charge via the Internet at http://pubs.acs.org.

■ AUTHOR INFORMATION

Corresponding Author

*E-mail: dlipomi@ucsd.edu.

Notes

The authors declare no competing financial interest.

■ ACKNOWLEDGMENTS

This work was supported by the laboratory startup funds from the University of California, San Diego. A.Z. acknowledges a fellowship from SoCal Clean Energy Technology Acceleration Program from the von Liebig Center at UCSD sponsored by the US Department of Energy, and a fellowship from the National Science Foundation Graduate Research Fellowship Program, DGE-1144086. H.M. acknowledges support provided by the Calit2-Qualcomm Institute Summer Undergraduate

Research Scholars program. B.M., T.D., and A.R.T. acknowledge support from the Office of Naval Research (Award No. N000141210574) and a DURIP grant (Award No. N000141310655). This work was performed in part with the support of the Calit2 Nano3 facilities and staff at the University of California, San Diego.

■ REFERENCES

(1) Mao, L.; Li, Z.; Wu, B.; Xu, H. *Appl. Phys. Lett.* **2009**, *94*, 243102.
(2) Aradhya, S. V.; Venkataraman, L. *Nat. Nanotechnol.* **2013**, *8*, 399–410.
(3) Xu, Q.; Gates, B. D.; Whitesides, G. M. *J. Am. Chem. Soc.* **2004**, *126*, 1332–1333.
(4) Xu, Q.; Bao, J.; Capasso, F.; Whitesides, G. M. *Angew. Chem., Int. Ed.* **2006**, *45*, 3631–3635.
(5) Xu, Q.; Rioux, R. M.; Dickey, M. D.; Whitesides, G. M. *Acc. Chem. Res.* **2008**, *41*, 1566–1577.
(6) Lipomi, D. J.; Martinez, R. V.; Whitesides, G. M. *Angew. Chem., Int. Ed.* **2011**, *50*, 8566–8583.
(7) Dawson, K.; Strutwolf, J.; Rodgers, K. P.; Herzog, G.; Arrigan, D. W. M.; Quinn, A. J.; O'Riordan, A. *Anal. Chem.* **2011**, *83*, 5535–5540.
(8) Pendry, J. B. *Phys. Rev. Lett.* **2000**, *85*, 3966–3969.
(9) Smythe, E. J.; Dickey, M. D.; Whitesides, G. M.; Capasso, F. *ACS Nano* **2009**, *3*, 59–65.
(10) Xia, Y.; Whitesides, G. M. *Annu. Rev. Mater. Sci.* **1998**, *28*, 153–184.
(11) Chou, S. Y.; Krauss, P. R.; Renstrom, P. J. *J. Vac. Sci. Technol., B* **1996**, *14*, 4129–4133.
(12) Resnick, D. J.; Sreenivasan, S. V.; Willson, C. G. *Mater. Today* **2005**, *8*, 34–42.
(13) Salaita, K.; Wang, Y.; Mirkin, C. A. *Nat. Nanotechnol.* **2007**, *2*, 145–155.
(14) Tang, J.; Wang, Y.; Nuckolls, C.; Wind, S. J. *J.Vac. Sci. Technol., B* **2006**, *24*, 3227–3229.
(15) Gates, B. D.; Xu, Q.; Stewart, M.; Ryan, D.; Willson, C. G.; Whitesides, G. M. *Chem. Rev.* **2005**, *105*, 1171–1196.
(16) Pourhossein, P.; Chiechi, R. C. *ACS Nano* **2012**, *6*, 5566–5573.
(17) Lipomi, D. J.; Kats, M. A.; Kim, P.; Kang, S. H.; Aizenberg, J.; Capasso, F.; Whitesides, G. M. *ACS Nano* **2010**, *4*, 4017–4026.
(18) Zaretski, A.; Moetazedi, H.; Kong, C.; Sawyer, E.; Savagartup, S.; Valle, E.; O'Connor, T.; Printz, A. L. *Nanotechnology* **2014**, in print.
(19) Malis, T. F.; Steele, D. *MRS Proc.* **1990**, *199*, 3–42.
(20) Lipomi, D. J.; Martinez, R. V.; Rioux, R. M.; Cademartiri, L.; Reus, W. F.; Whitesides, G. M. *ACS Appl. Mater. Interfaces* **2010**, *2*, 2503–2514.
(21) Li, T.; Suo, Z. *Int. J. Solids Struct.* **2007**, *44*, 1696–1705.
(22) Xiang, Y.; Li, T.; Suo, Z.; Vlassak, J. J. *Appl. Phys. Lett.* **2005**, *87*, 1–3.
(23) Kim, Y.; Lee, J.; Yeom, M. S.; Shin, J. W.; Kim, H.; Cui, Y.; Kysar, J. W.; Hone, J.; Jung, Y.; Jeon, S.; Han, S. M. *Nat. Commun.* **2013**, *4*, 2114.
(24) Lee, C.; Wei, X.; Kysar, J. W.; Hone, J. *Science* **2008**, *321*, 385–388.
(25) Vanin, M.; Mortensen, J. J.; Kelkkanen, A. K.; Garcia-Lastra, J. M.; Thygesen, K. S.; Jacobsen, K. W. *Phys. Rev. B* **2010**, *81*, 081408.
(26) Malard, L. M.; Pimenta, M. A.; Dresselhaus, G.; Dresselhaus, M. S. *Phys. Rep.* **2009**, *473*, 51–87.
(27) Pimenta, M. A.; Dresselhaus, G.; Dresselhaus, M. S.; Cançado, L. G.; Jorio, A.; Saito, R. *Phys. Chem. Chem. Phys.* **2007**, *9*, 1276–1291.
(28) Gottscho, R. A. *J. Vac. Sci. Technol., B* **1992**, *10*, 2133–2147.
(29) Trusovas, R.; Ratautas, K.; Račiukaitis, G.; Barkauskas, J.; Stankevičiene, I.; Niaura, G.; Mažeikiene, R. *Carbon N. Y.* **2013**, *52*, 574–582.
(30) Mohiuddin, T. M. G.; Lombardo, A.; Nair, R. R.; Bonetti, A.; Savini, G.; Jalil, R.; Bonini, N.; Basko, D. M.; Galiotis, C.; Marzari, N.; Novoselov, K. S.; Geim, A. K.; Ferrari, A. C. *Phys. Rev. B: Condens. Matter Mater. Phys.* **2009**, *79*, 205433 .
(31) Kim, N.-Y.; Oh, M.-K.; Park, S.-H.; Kim, S.-K.; Hong, B.-H. *Bull. Korean Chem. Soc.* **2010**, *31*, 999–1003.
(32) Ghosh, D. *Opt. Photonics J.* **2013**, *03*, 18–26.
(33) Ferrari, A. C.; Basko, D. M. *Nat. Nanotechnol.* **2013**, *8*, 235–246.

Chapter 4

Metallic Nanoislands on Graphene as Highly Sensitive Transducers of Mechanical, Biological, and Optical Signals

Aliaksandr V. Zaretski,† Samuel E. Root,† Alexander Savchenko,‡,§ Elena Molokanova,// Adam D. Printz,† Liban Jibril,† Gaurav Arya,† Mark Mercola,‡,§ and Darren J. Lipomi*,†

†Department of NanoEngineering, University of California, San Diego, 9500 Gilman Drive, La Jolla, California 92093-0448, United States

‡Department of Bioengineering, University of California, San Diego, 9500 Gilman Drive, La Jolla, California 92093-0412, United States

§Sanford-Burnham Medical Research Institute, 10901 North Torrey Pines Road., La Jolla, California 92037, United States

//NTBS, 309 Hestia Way, Encinitas, California 92024, United States

NANO LETTERS
Letter
pubs.acs.org/NanoLett

Metallic Nanoislands on Graphene as Highly Sensitive Transducers of Mechanical, Biological, and Optical Signals

Aliaksandr V. Zaretski,[†] Samuel E. Root,[†] Alexander Savchenko,[‡,§] Elena Molokanova,[∥] Adam D. Printz,[†] Liban Jibril,[†] Gaurav Arya,[†] Mark Mercola,[‡,§] and Darren J. Lipomi*[,†]

[†]Department of NanoEngineering, University of California, San Diego, 9500 Gilman Drive, La Jolla, California 92093-0448, United States

[‡]Department of Bioengineering, University of California, San Diego, 9500 Gilman Drive, La Jolla, California 92093-0412, United States

[§]Sanford-Burnham Medical Research Institute, 10901 North Torrey Pines Road., La Jolla, California 92037, United States

[∥]NTBS, 309 Hestia Way, Encinitas, California 92024, United States

Supporting Information

ABSTRACT: This article describes an effect based on the wetting transparency of graphene; the morphology of a metallic film (≤20 nm) when deposited on graphene by evaporation depends strongly on the identity of the substrate supporting the graphene. This control permits the formation of a range of geometries, such as tightly packed nanospheres, nanocrystals, and island-like formations with controllable gaps down to 3 nm. These graphene-supported structures can be transferred to any surface and function as ultrasensitive mechanical signal transducers with high sensitivity and range (at least 4 orders of magnitude of strain) for applications in structural health monitoring, electronic skin, measurement of the contractions of cardiomyocytes, and substrates for surface-enhanced Raman scattering (SERS, including on the tips of optical fibers). These composite films can thus be treated as a platform technology for multimodal sensing. Moreover, they are low profile, mechanically robust, semitransparent and have the potential for reproducible manufacturing over large areas.

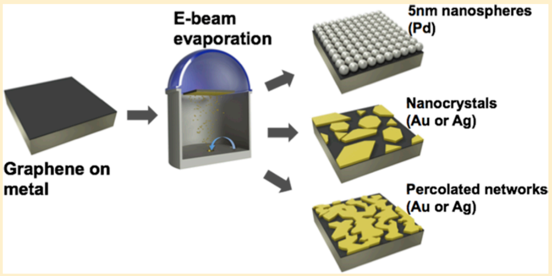

KEYWORDS: *Graphene, wetting transparency, strain sensor, SERS, wearable sensor, cardiomyocyte*

Graphene has several attractive characteristics for designing functional nanocomposite thin films. It is flexible (and stretchable, compared to metallic films, to strains of 5−6%), conductive, transparent, amenable to large-area growth and transfer to many substrates,[1] and its crystalline grains can extend over dimensions reaching 1 cm.[2] Critical to this paper, its stature as the thinnest obtainable 2D material gives rise to a phenomenon known as wetting transparency.[3] While this phenomenon has been explored primarily with respect to liquids, for which quantities such as contact angle are a strong function of the surface energy of the layer supporting the graphene, our experiments demonstrate that this concept extends to an evaporated flux of atoms. A metal/graphene bilayer can thus be used as a template for the self-assembly of nanoparticles of diverse and controllable morphologies, that is, nanospheres, nanocrystals, and percolated networks, by e-beam evaporation. Figure 1 illustrates this concept and the range of morphologies available when only the evaporated metal (gold and silver) and the substrate were changed (copper, nickel, gold, and silver), keeping all other parameters constant. These graphene/nanoisland (NI) films exhibited sufficient robustness to transfer to nearly any surface along with characteristics such as sharp tips and gaps approaching molecular dimensions that make them amenable to sensing of chemical, optical, and mechanical stimuli.

For all the experiments, the nanoislands were self-assembled on single-layer graphene synthesized on copper foils by chemical vapor deposition (CVD, Supporting Information Figure S1).[4] To transfer graphene from copper onto other metals (gold, silver, and nickel), we used metal-assisted exfoliation (MAE).[5] During a single concurrent deposition of thin (10 nm) metal film (gold, silver, or palladium) onto graphene on various substrates (copper, nickel, gold, and silver) the apparent crystallinity, shape, and size distribution of the resulting nanoislands, extent of percolation, as well as the size of the gaps between the islands were different for each substrate. The resulting morphologies directly depended on the nature of the substrate material (surface energy, crystallographic orientation, Supporting Information Figure S2) and the evaporated metal (surface energy, lattice mismatch with

Received: November 25, 2015
Revised: January 8, 2016

DOI: 10.1021/acs.nanolett.5b04821

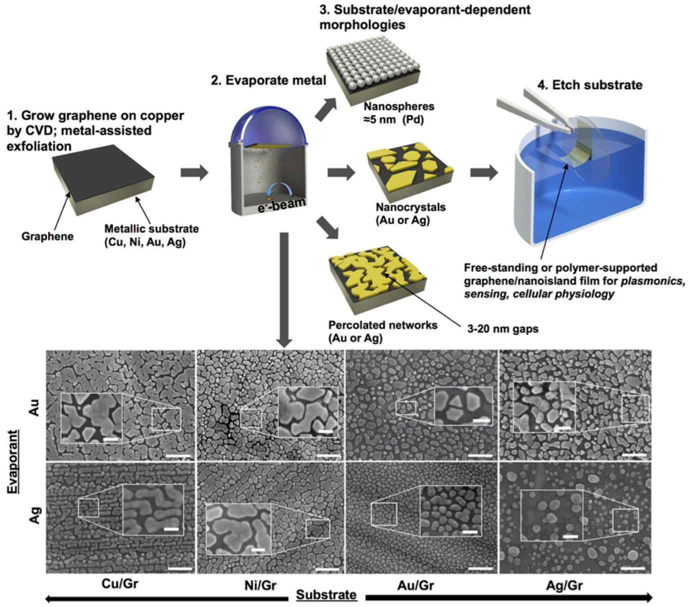

Figure 1. Schematic diagram of the process used to generate nanoislands (top) and scanning electron micrographs of metallic nanoislands on various substrates obtained by electron beam evaporation of evaporant (y-axis) onto a graphene/metal substrate (x-axis) (bottom). Ten nanometers of gold (first row) and 10 nm of silver (second row) evaporated onto (left to right) graphene on copper foil (as grown), MAE-transferred graphene on nickel, MAE-transferred graphene on gold, and MAE-transferred graphene on silver. Each evaporant was deposited onto the substrates concurrently in the same chamber. Scale bars: 200 nm. Scale bars in insets: 50 nm.

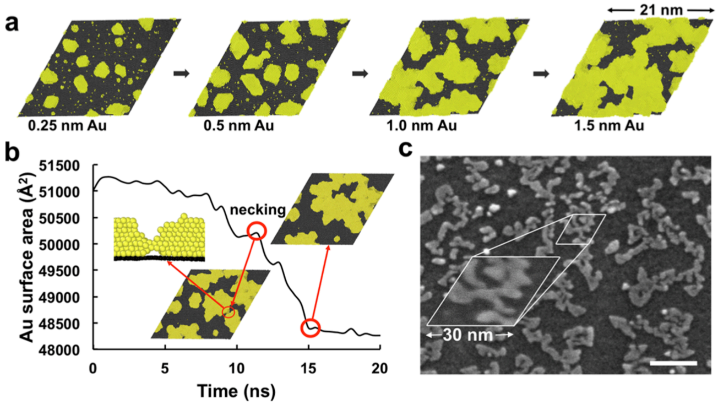

Figure 2. Structural evolution of nanoislands as predicted by molecular dynamics simulations. Simulated evaporation of 1.5 nm of gold onto graphene on copper (a). Plot of the change of the total surface area of gold nanoislands during 20 ns of vacuum annealing at 500 K. Merging of nanoislands is preceded by crystallographic alignment and necking (surface area increase) (Supporting Information Video S1) (b). Scanning electron micrograph of 1 nm of gold evaporated onto graphene on copper (c). Scale bar: 50 nm.

graphene) (Figure 1, bottom), the number of graphene layers (Supporting Information Figure S3), as well as the processing parameters. These parameters included rate (Supporting Information Figure S4) and amount of deposition, temperature of the substrate (Supporting Information Figure S5), thermal annealing after deposition (Supporting Information Figure S6), and transfer to the final receiving substrate (Supporting Information Figure S7).

The strong dependence of the final morphology of the islands on the identity of the metal supporting the graphene suggested that growth may follow rules similar to those that have been developed for epitaxial growth.[6] Generally, three major modes for film growth exist in a two-element system: layer-by-layer (Frank–Van der Merve), layer/island (Stranski–Krastanov), and island proper (Volmer–Weber).[7] These modes are determined largely by the mismatches of the lattice dimensions and the surface energies between the evaporant and the substrate. A larger lattice mismatch favors island growth, while positive surface energy difference, $(\gamma_{\text{substrate}} - \gamma_{\text{film}})/\gamma_{\text{substrate}}$, favors layer-by-layer growth. Inserting graphene between the evaporant and the substrate thus permitted tuning of the surface energy by changing the substrate metal, assuming

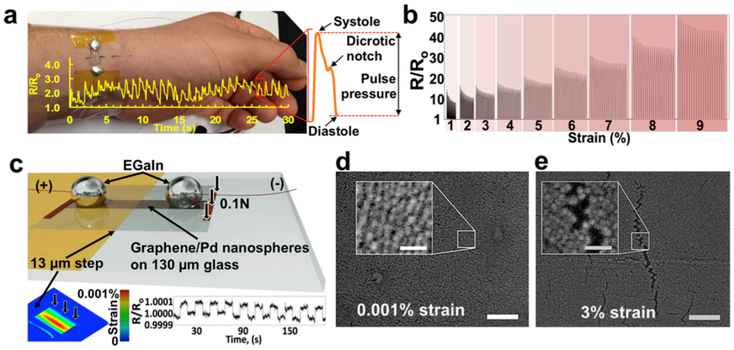

Figure 3. Nanoisland strain sensors. Photograph of the PDMS/PdNI/graphene strain sensor placed atop the radial artery for detection of the pulse (overlaid in figure) (a). Note the high resolution of the pulse pressure-waveform (in the blow-out) with distinguishable systolic and diastolic pressures, the dicrotic notch (aortic valve closure), and other cardiac cycle events. Normalized resistance plot of the PDMS/graphene/PdNI strain sensor stretched cyclically (20 cycles for each strain) to 1, 2, 3, ... 9% strain (b). Schematic diagram of a graphene/PdNI strain sensor used to sense 0.001% tensile strain on the surface of the 130 μm thick glass coverslip (used as a cantilever with the amplitude of deflection equal to 13 μm) (c). Finite-element analysis (FEA) model of the strain on the cantilever surface (left inset). Normalized resistance plot of the graphene/PdNI strain sensor under cyclic tensile strain of 0.001% (right inset). Scanning electron micrograph of the glass/graphene/PdNI strain sensor under tensile strain of ~0.001% (d). Scale bar: 100 nm. Scale bar in inset: 25 nm. Scanning electron micrograph of the PDMS/graphene/PdNI strain sensor under tensile strain of ~3% (e). Scale bar: 100 nm. Scale bar in inset: 25 nm.

some degree of wetting transparency of the graphene. The wetting transparency of graphene on metals (Cu and Au) to liquids has been explicitly demonstrated by Rafiee et al.[3] According to their findings (both empirical, water contact angle, and molecular dynamics simulations), single layer graphene changes the surface energy of metals by less than 2% of its initial value, so the wettability of the metallic substrates is maintained through the graphene layer. Introducing graphene on copper changed the water contact angle by ~0.3° (from 85.9 to 86.2°), while for gold the value was ~1.4° (from 77.4 to 78.8°).

The lattice mismatch between the evaporant and the graphene on any substrate was essentially fixed (±0.5% of the mismatch value due to the substrate-induced strain on graphene).[8,9] Considering very low diffusion barriers for gold and silver on graphene[10] and a low rate of deposition (consistent with thermodynamic, as opposed to kinetic, control), the system with graphene is biased toward island growth mode but still correlates quite well with the model (Supporting Information Figure S8).

To elucidate the mechanism of nanoisland formation, we have performed massively parallel atomistic simulations[11] of the deposition and annealing of gold atoms onto a graphene-coated copper (111) surface. Copper/graphene/gold was chosen as our model system due to the availability of accurate interatomic potentials[12−15] (see Supporting Information) and because fabricating this architecture experimentally required the least number of steps. We analyzed the deposition of five monolayers of gold (~30 000 atoms) onto a 3 × 3 copper/graphene Moiré super cell[16] (~240 000 atoms) over the course of 150 ns at 400 K. The simulated deposition rate was about 9 orders of magnitude faster than the experimental rate (30 s per monolayer) so we expected the initial morphology produced by the simulated deposition (Figure 2a) to be kinetically controlled. To generate a thermodynamically controlled morphology for comparison with experiment, we performed a simulation of thermal annealing of the gold nanoislands on graphene on copper (three monolayers of gold deposited) at 500 K for 20 ns. Figure 2b shows the decrease in the total surface area[17] of gold during the annealing. We observed that merging of islands occurs during the initial 15 ns, as noted by the decrease in the net surface area of gold, after which the rate of change of the island morphology became diminished. This observation suggested that the simulated deposition process indeed generated kinetically trapped clusters that aggregated over short (ns) time scales. The morphology predicted by the simulation in Figure 2a,b was verified experimentally for the deposition of 1 nm gold in Figure 2c. The similarity between the simulated and experimental morphologies is striking considering that the experiment was performed after the simulation (i.e., the parameters used in the simulation were not adjusted to fit the experiment).

The ability to predict the morphology of the graphene-supported nanoislands, along with their ability to be transferred to arbitrary substrates, suggested several applications in chemical and mechanical sensing. We examined the piezoresistance of metal nanoislands on graphene supported by rigid, flexible, and stretchable substrates and determined that these composites can serve as excellent strain sensors. In particular, depositing 8−10 nm of palladium onto graphene on copper and transferring the composite film onto thin (8 μm) polydimethylsiloxane (PDMS) by spin-coating the polymer and etching the copper substrate generated highly sensitive strain sensors capable of epidermal measurement of the human pulse pressure wave in the radial artery (Figure 3a). The device clearly resolves the systole, diastole, and the dicrotic notch (aortic valve closure). The sensitivity is among the highest of any thin-film strain sensor with the gauge factor (GF = $(R - R_0)/R_0 \times 1/\varepsilon$, where ε is strain and $(R - R_0)/R_0$ is normalized resistance) at 1% strain being 1335 (743 after 19 stretch/release cycles) (Figure 3b). We have measured strains as small as 0.001% with the graphene/PdNI sensor deposited onto a 130 μm thick glass coverslip. In order to induce such minor strains precisely and repeatedly, the sensor was placed onto a rigid substrate bearing 13 μm thick polyimide tape supporting one-half of the coverslip (the other half forming a cantilever) (Figure 3c). By applying a small force (~0.1 N) to the cantilever and bringing the far edge in contact with the substrate, 0.001% tensile strain (Supporting Information Figure S11) on the glass surface was achieved and measured repeatedly with the sensor. Thus, the graphene/PdNI strain sensors demonstrated a useful range spanning at least 4 orders of magnitude. We noticed that the sensors demonstrated a nonlinear rate of change in resistance versus strain (i.e., gauge factor) with at least two inflection points (Supporting Information Figure S12), which potentially indicated different sensing modes. The piezoresistive effect in the lowest strain regime (0.001%) is most likely due to the changes in tunneling current when the PdNI underwent small changes in separation (Figure 3d). The gauge factor of 10 in this regime is similar to literature values for changes in tunneling resistance at strains ≪1%[18] (though other similar sensors, generally prepared by interfacial self-assembly,[19−21] are unsupported and thus significantly less mechanically robust than graphene/NI films, which can be transferred easily to most substrates). At the lower single-digit strains, cracks appeared in the PdNI film (Figure 3e).[22] The opening and closing of these cracks in response to cyclic loading appears to be the mechanism of piezoresistance in the most sensitive regime.[23] Apparently, the crack propagation through the PdNI film is suppressed by the stiffness of the underlying graphene,[24] which is manifested in the reduction of the gauge factor from 735 to 316 (at 1 and 5%, respectively). At around 5−6% strain, the sensitivity increased, which can be explained by the crack onset of the underlying graphene (Supporting Information Figures S13, S14, and S20) and thus increased crack propagation through the PdNI film. Patterned graphene has been previously reported to demonstrate piezoresistive behavior in strain sensors with high gauge factors at up to 10% tensile strains due to cracking of the graphene.[25] We compared the characteristics of the graphene/NI films to other piezoresistive thin-film strain sensors reported in the literature (Supporting Information Table S2). In particular, the graphene/NI films demonstrated sensitivity to the smallest strain (0.001%), exhibited the greatest maximum gauge factor (1330), and were stable to cyclic loading over the greatest range of applied strains (0.001−9%). Moreover, the ability to manipulate graphene/NI films compare favorably to unsupported films of nanoparticles, which cannot be transferred easily to arbitrary substrates. We also found excellent compatibility of these thin films with cardiomyocytes (vide infra); the ability to interface these films with biological structures could have significant implications in applications from neuroprostheses to high-throughput screening for cardiotoxicity in drug discovery.

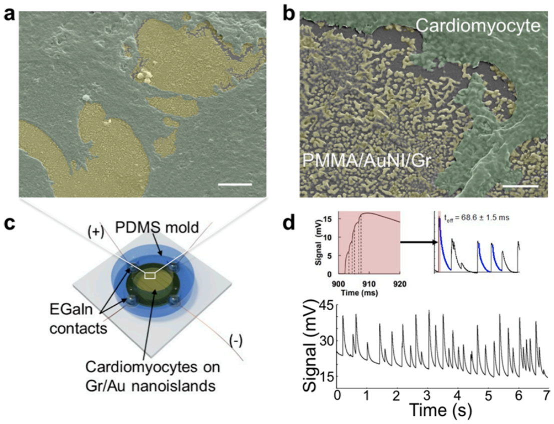

Figure 4. Nanoislands on graphene as substrates for cellular electrophysiology. Scanning electron microscopy images of the fixed cardiomyocyte culture on PMMA/AuNI/graphene substrate (cells are false-colored green and gold is false-colored yellow) (a,b). Scale bars: 5 μm and 200 nm, respectively. Schematic diagram of the electrophysiological chamber used for registering cardiomyocyte contractions (c). Signal modulation obtained from the cell culture on PMMA/AuNI/graphene during spontaneous contractions of cells (d). Profile of the signal rise phase (left inset). Profile of the signal decay phase (right inset).

To test the performance of graphene/AuNI sensors in biological settings, we used neonatal rat cardiomyocytes (CM) cultured on coverslips coated with poly(methyl methacrylate) (PMMA)/AuNI/graphene. We noticed excellent biocompatibility[26] of the substrates with live CM without the need for additional adhesion promoters as detected by optical and scanning electron microscopy (Figure 4a,b). Our choice of gold NI films in this application was made on the basis of biocompatibility. While AuNI films have a uniform morphology on copper, the morphology changes somewhat when wet-transferred onto glass substrates to a more disordered appearance (Figures 5b, inset and Supporting Information Figure S7) and further culturing cardiomyocytes on such substrates seemed to introduce additional disorder, possibly by fragmenting previously connected nanoislands by mechanical forces imposed on the substrate. Using a specialized chamber (Figure 4c and Supporting Information), we were able to detect reversible changes in the sensor signal that correlated with the spontaneous activity of cardiomyocytes (Figure 4d). Our sensors exhibited submillisecond response time (t_{on} = 0.8 ± 0.2 ms, n = 173), and very high signal-to-noise ratio (between 42 and 100 for CM contractions of different strength) (Figure 4d, top left, Supporting Information Video S2). The exponential decay profile was similar for all contractions and was fitted with a single exponential function (t_{off} = 68.6 ± 1.5 ms, n = 173) (Figure 4d, top right). The amplitude and the temporal profile of CM contractions as detected by our sensor allow a detailed characterization of CM response and enable testing of various pharmacological compounds for drug discovery applications.[27]

We also examined the optical response of these plasmonically active nanoparticles. Films of noble metals are widely used as substrates for surface-enhanced Raman scattering (SERS). The large increase of the electric field in the gaps between the metallic nanostructures upon illumination with a resonant frequency enhances the Raman scattering and allows label-free identification of molecules.[28] Placing SERS-active substrates onto optical fibers could allow remote sensing (e.g., for the detection of contaminants in groundwater or biomarkers in the bloodstream).[29−31] To this end, we transferred graphene/AuNI films onto tips of optical fibers (Figure 5a,b) and deposited a monolayer of 1-butanethiolate (BT) onto the surface structures. The modified optical fibers exhibited a strong signal, while an unstructured gold film on silicon produced no signal when excited from the top surface (Figure 5c).

Metallic nanoislands deposited on the surface of graphene, whose morphology can be controlled by the identity of the substrate supporting graphene and predicted by computation, offer a promising platform system for multimodal sensing. In contrast to films of metallic nanoparticles formed by other procedures, graphene-supported nanoislands have the capacity for manipulation and facile transfer to nearly any surface.

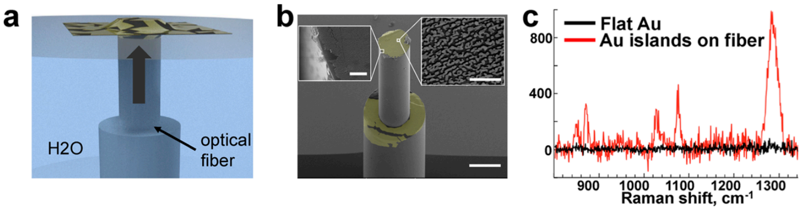

Figure 5. Graphene/NI as SERS sensors. Schematic diagram of the deposition of free-floating gold nanoislands/graphene SERS substrate onto the tip of the optical fiber (a). Scanning electron micrograph of graphene/AuNI SERS substrate on the tip of the optical fiber (gold is false-colored) (b). Scale bars: 150 μm, 2 μm in the left inset, 500 nm in the right inset. Raman spectra of 1-butanethiolate from graphene/AuNI-coated optical fibers (red) and unstructured 100 nm thick gold film (black) (c).

Deposition of these structures on relatively rigid (glass), flexible (PMMA), or stretchable (PDMS) substrates permits applications in human and structural health monitoring in which the demonstrated sensitivity spans at least 4 orders of magnitude and has among the highest absolute sensitivity and gauge factors of any thin-film strain sensor yet reported. The sensitivity and biocompatibility of these structures permit measurement of the contractions of cardiomyocytes noninvasively and may be an invaluable tool for functional characterization of stem-cell derived cardiomyocytes and multimodal screening of novel drug candidates for cardiotoxicity and cardiovascular drug discovery. The ability to transfer these multimodal sensors to any substrate permits mounting of structures directly on the tips of optical fibers for remote sensing by SERS.

■ ASSOCIATED CONTENT

Ⓢ Supporting Information

The Supporting Information is available free of charge on the ACS Publications website at DOI: 10.1021/acs.nanolett.5b04821.

Video showing merging of nanoislands is preceded by crystallographic alignment and necking. (AVI)

Video micrograph of cardiomyocytes contracting on top of sensors exhibiting submillisecond response time and very high signal-to-noise ratio. (AVI)

Detailed procedures for synthesis of graphene and transfer to metallic substrates, deposition of nanoislands, simulations of deposition, preparation of SERS substrate on optical fiber, fabrication of strain sensors, imaging, and electrophysiology, along with Figures S1−S23 and Tables S1−S2. (PDF)

■ AUTHOR INFORMATION

Corresponding Author

*E-mail: dlipomi@eng.ucsd.edu.

Notes

The authors declare no competing financial interest.

■ ACKNOWLEDGMENTS

A.Z. acknowledges a fellowship from SoCal Clean Energy Technology Acceleration Program from the von Liebig Center at UCSD sponsored by the U.S. Department of Energy and a fellowship from the National Science Foundation Graduate Research Fellowship Program, DGE-1144086. Authors A.Z., S.R., L.J., and D.L. acknowledge funding from the laboratory startup funds provided by the University of California, San Diego. A.S., E.M., and M.M. acknowledge funding from Fondation Leducq "Shapeheart" Transatlantic Alliance, California Institute for Regenerative Medicine, CIRM TR4-06857, and from the National Institutes of Health, 1R01HL128072-01, 5R01HL113601-04. We would like to acknowledge the assistance of Shelby Triplitt in preparing the copper substrates for graphene synthesis. We would like to gratefully acknowledge the computational resources provided by the Extreme Science and Engineering Discovery Environment (XSEDE) program, which is supported by the National Science Foundation grant number ACI-1053575.

■ REFERENCES

(1) Bae, S.; Kim, H.; Lee, Y.; Xu, X.; Park, J.-S.; Zheng, Y.; Balakrishnan, J.; Lei, T.; Kim, H. R.; Song, Y.; Il Kim, Y.-J.; Kim, K. S.; Ozyilmaz, B.; Ahn, J.-H.; Hong, B. H.; Iijima, S. *Nat. Nanotechnol.* **2010**, *5*, 574−578.

(2) Hao, Y.; Bharathi, M. S.; Wang, L.; Liu, Y.; Chen, H.; Nie, S.; Wang, X.; Chou, H.; Tan, C.; Fallahazad, B.; Ramanarayan, H.; Magnuson, C. W.; Tutuc, E.; Yakobson, B. I.; McCarty, K. F.; Zhang, Y.-W.; Kim, P.; Hone, J.; Colombo, L.; Ruoff, R. S. *Science* **2013**, *342*, 720−723.

(3) Rafiee, J.; Mi, X.; Gullapalli, H.; Thomas, A. V.; Yavari, F.; Shi, Y.; Ajayan, P. M.; Koratkar, N. A. Wetting transparency of graphene. *Nat. Mater.* **2012**, *11*, 217−222.

(4) Regmi, M.; Chisholm, M. F.; Eres, G. *Carbon* **2012**, *50*, 134−141.

(5) Zaretski, A. V.; Moetazedi, H.; Kong, C.; Sawyer, E. J.; Savagatrup, S.; Valle, E.; O'Connor, T. F.; Printz, A. D.; Lipomi, D. J. *Nanotechnology* **2015**, *26*, 045301.

(6) Ohring, M. *Materials Science of Thin Films*; Elsevier: New York, 2001.

(7) Tu, K.; Mayer, J. W.; Feldman, L. C. *Electronic Thin Film Science: For Electrical Engineers and Materials Scientists*; Macmillan: New York, 1992.

(8) Pannu, C.; Singh, U. B.; Kumar, S.; Tripathi, A.; Kabiraj, D.; Avasthi, D. K. *Appl. Surf. Sci.* **2014**, *308*, 193−198.

(9) He, R.; Zhao, L.; Petrone, N.; Kim, K. S.; Roth, M.; Hone, J.; Kim, P.; Pasupathy, A.; Pinczuk, A. *Nano Lett.* **2012**, *12*, 2408−2413.

(10) Liu, X.; Wang, C.-Z.; Hupalo, M.; Lin, H.-Q.; Ho, K.-M.; Tringides, M. C. *Crystals* **2013**, *3*, 79.

(11) Plimpton, S. *J. Comput. Phys.* **1995**, *117*, 1−42. The documentation and code for LAMMPS can be found at http://lammps.sandia.gov.

(12) Süle, P.; Szendrő, M. *Modell. Simul. Mater. Sci. Eng.* **2015**, *23*, 025001.

(13) Foiles, S. M.; Baskes, M. I.; Daw, M. S. *Phys. Rev. B: Condens. Matter Mater. Phys.* **1986**, *33*, 7983−7991.

(14) Stuart, S.; Tutein, A.; Harrison, J. *J. Chem. Phys.* **2000**, *112*, 6472−6486.

(15) Helgee, E. E.; Isacsson, A. Unpublished work, 2015. Available at http://publications.lib.chalmers.se/publication/214089-adsorption-of-metal-atoms-at-a-buckled-graphene-grain-boundary-using-model-potentials.

(16) Süle, P.; Szendrő, M.; Hwang, C.; Tapasztó, L. *Carbon* **2014**, *77*, 1082−1089.
(17) Stukowski, A. *JOM* **2014**, *66*, 399−407.
(18) Koppinen, P. J.; Lievonen, J. T.; Ahlskog, M. E.; Maasilta, I. J. Tunnel junction based displacement sensing for nanoelectromechanical systems. *Journal of Physics: Conference Series* **2007**, *92*, 012051.
(19) Segev-Bar, M.; Landman, A.; Nir-Shapira, M.; Shuster, G.; Haick, H. *ACS Appl. Mater. Interfaces* **2013**, *5*, 5531−5541.
(20) Moreira, H.; Grisolia, J.; Sangeetha, N. M.; Decorde, N.; Farcau, C.; Viallet, B.; Chen, K.; Viau, G.; Ressier, L. *Nanotechnology* **2013**, *24*, 095701.
(21) Siffalovic, P.; Chitu, L.; Vegso, K.; Majkova, E.; Jergel, M.; Weis, M.; Luby, S.; Capek, I.; Keckes, J.; Maier, G. A.; Satka, A.; Perlich, J.; Roth, S. V. *Nanotechnology* **2010**, *21*, 385702.
(22) Correa-Duarte, M. A.; Salgueiriño-Maceira, V.; Rinaldi, A.; Sieradzki, K.; Giersig, M.; Liz-Marzán, L. M. Optical strain detectors based on gold/elastomer nanoparticulated films. *Gold Bulletin* **2007**, *40*, 6−14.
(23) Lee, J.; Kim, S.; Lee, J.; Yang, D.; Park, B. C.; Ryu, S.; Park, I. *Nanoscale* **2014**, *6*, 11932−11939.
(24) Lee, C.; Wei, X.; Kysar, J. W.; Hone, J. *Science* **2008**, *321*, 385−388.
(25) Li, X.; Zhang, R.; Yu, W.; Wang, K.; Wei, J.; Wu, D.; Cao, A.; Li, Z.; Cheng, Y.; Zheng, Q.; Ruoff, R. S.; Zhu, H. *Sci. Rep.* **2012**, *2*, 870.
(26) Crisan, L.; Crisan, B.; Soritau, O.; Baciut, M.; Biris, A. R.; Baciut, G.; Lucaciu, O. *J. Appl. Toxicol.* **2015**, *35*, 1200−1210.
(27) Pointon, A.; Harmer, A. R.; Dale, I. L.; Abi-Gerges, N.; Bowes, J.; Pollard, C.; Garside, H. *Toxicol. Sci.* **2015**, *144*, 227−237.
(28) Zaretski, A.; Marin, B. C.; Moetazedi, H.; Dill, T. J.; Jibril, L.; Kong, C.; Tao, A. R.; Lipomi, D. J. *Nano Lett.* **2015**, *15*, 635−640.
(29) Wang, X. D.; Wolfbeis, O. S. Fiber-optic chemical sensors and biosensors (2008−2012). *Anal. Chem.* **2013**, *85*, 487−508.
(30) Smythe, E. J.; Dickey, M. D.; Bao, J.; Whitesides, G. M.; Capasso, F. *Nano Lett.* **2009**, *9*, 1132−1138.
(31) Lipomi, D. J.; Martinez, R. V.; Kats, M. A.; Kang, S. H.; Kim, P.; Aizenberg, J.; Capasso, F.; Whitesides, G. M. *Nano Lett.* **2011**, *11*, 632−636.

Appendix A

Supporting Information for Chapter 3

Using the Thickness of Graphene to Template Lateral Subnanometer Gaps between Gold Nanostructures

Aliaksandr V. Zaretski, Brandon C. Marin, Herad Moetazedi, Tyler J. Dill, Liban Jibril,
Casey Kong, Andrea R. Tao, and Darren J. Lipomi

Department of NanoEngineering, University of California, San Diego
9500 Gilman Drive, Mail Code 0448, La Jolla, CA 92093-0448

Supporting Information:

Using the Thickness of Graphene to Template Lateral Sub-Nanometer Gaps between Gold Nanostructures

Aliaksandr V. Zaretski, Brandon C. Marin, Herad Moetazedi, Tyler J. Dill, Liban Jibril, Casey Kong, Andrea R. Tao, and Darren J. Lipomi*

Department of NanoEngineering, University of California, San Diego, 9500 Gilman Drive Mail Code 0448, La Jolla, CA 92093-0448

*Author to whom correspondence should be addressed: dlipomi@ucsd.edu

Cleaning the copper foil. Graphene was synthesized on 25-µm-thick copper foils (Alpha Aesar, 13382, 99.8%) with the dimensions of 10 cm × 11 cm (the largest graphene sheet synthesized and transferred by us via the MAE method was 18 cm × 20 cm). Prior to the growth of graphene, we cleaned the copper foils by soaking them in a shallow acetone bath and wiping them with a Kimwipe tissue (while in acetone). After that the foils were rinsed with acetone and transferred into a similar bath filled with isopropyl alcohol (IPA), mechanical cleaning was repeated in this solvent. We note that the mechanical cleaning resulted in more pristine graphene than after cleaning the foils via sonication in acetone and IPA[1]; this method also saved a considerable amount of the both solvents (considering the large volumes required for sonicating large-area copper foils). After the mechanical cleaning in IPA, the foils were rinsed in IPA and dried in a stream of compressed air.

Electropolishing the copper foil. In order to generate mostly single-layer graphene, we found it necessary to electropolish the copper foils prior to graphene synthesis.[1,2] The clean, dry copper foil was placed into a 250-mL beaker, following the contours of the beaker side-walls, and was used as the anode. A copper pipe (d = 2.54 cm, l = 15 cm) was inserted into the beaker along the cylindrical axis and used as the cathode. The cylindrical shape of the cathode and the curved surface of the anode generated a uniform electric field during the electropolishing. Concentrated phosphoric acid (H_3PO_4, 15 M) was used as the electrolyte and was poured into the beaker after the cathode and the anode were secured with a clamp and an alligator clip respectively. A 20 W DC power supply was used to generate the necessary current and voltage. The voltage was set at 1.6 V and electropolishing proceeded until the current fell 50% and plateaued from the initial value (usually between 5 – 10 min). After the electropolishing, the cathode and the electrolyte were removed from the beaker and the copper foil was extensively rinsed with DI water (3 min). Then the copper foil was rinsed with IPA, blow-dried under a stream of compressed air, and immediately loaded into the middle of the quartz tube of a chemical vapor deposition (CVD) reactor.

Synthesis of graphene. Atmospheric-pressure CVD graphene synthesis was performed in a quartz tube furnace (MTI OTF-1200X-HVC-UL) with the following tube dimensions: d = 7.6 cm, l = 100 cm. The CVD chamber and the reactor gas-supply lines were purged of air for 5 min by flowing a mixture of all synthesis gases (hydrogen, methane, and argon) at their maximum flow rates while pulling vacuum on the chamber with a diaphragm vacuum pump. After 5 min, the gas flow was stopped and the chamber was evacuated to about 10^{-4} torr with a turbomolecular vacuum pump in order to remove methane and hydrogen from the gas-mixing and the reactor chambers as well as to desorb the possible organic contaminants from the surface of the copper foil. The chamber was then re-pressurized to atmospheric pressure with ultra-high purity argon (700 SCCM), which flowed constantly throughout the entire procedure of graphene synthesis. The copper foils were heated in argon flow to 1050 °C (30 min). Upon reaching this temperature, additional hydrogen (60 SCCM) was flowed for 30 min to anneal and activate the copper substrate. After the 30 min of annealing, the flow rate of hydrogen was reduced to 5 SCCM and 0.7 SCCM of methane was flowed for 20 min for the synthesis of graphene (total gas flow rate: 700 SCCM argon + 5 SCCM hydrogen + 0.7 SCCM methane = 705.7 SCCM). After 20 min of graphene growth, the furnace was turned off and cracked open 5 cm (continuing the same gas flow). When the furnace cooled to 700 °C (ca. 5 min) it was opened to 10 cm. At 350 °C (ca. 30 min), the furnace was completely opened. At 200 °C, the hydrogen and methane flows were cut off and the reactor chamber was allowed to cool to room temperature in the argon flow (total cooling time was approximately 1 h).

Electron-beam evaporation. A Temescal BJD-1800 e-beam evaporator was used to metallize the graphene with a 150-nm film of gold. The metal evaporation rate was 2 Å s^{-1} and the chamber pressure was kept at 7×10^{-7} torr.

Ultramicrotomy of extremely thin sections. We were able to obtain sections of the composite nanowire as thin as 20 nm, although such thin sectioning resulted in the increased defectiveness of the wires (breaks, regions of delamination, buckles – **Figure S1a,b**). Composite wires as thin as 40-50 nm did not exhibit buckles or delamination (**Figure S1c**) but had 2-3 times more break defects than 150 nm-thick wires. Thickness of the obtained composite wires was confirmed by AFM (**Figure S1d**).

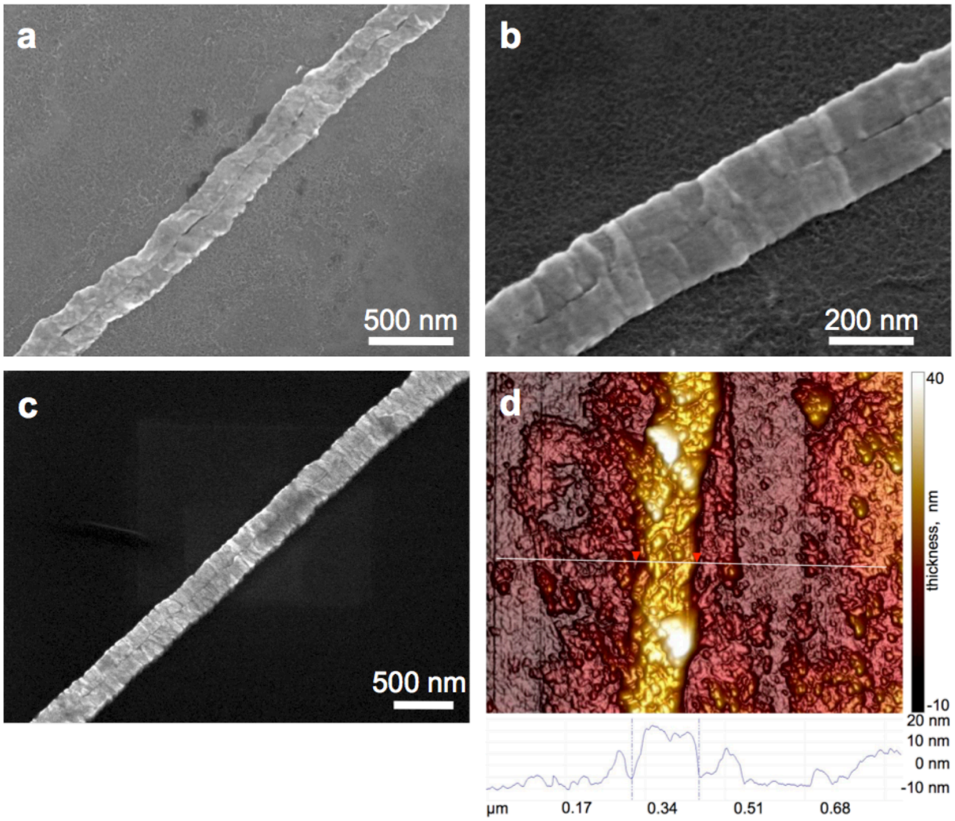

Figure S1. SEM images of perpendicularly-sectioned gold/graphene/gold composite nanowires sectioned at 20 nm thickness (**a,b**) and 50 nm thickness (**c**). AFM image and a height profile of a perpendicularly-sectioned gold/graphene/gold composite nanowire sectioned at 20 nm thickness (**d**).

Finite Element Analysis. To understand how the mechanics of the sectioning process influenced the geometry of the structures produced (formation of the opening at the top surface of the gold/graphene/gold interface), we performed finite-element simulations of cutting in both the parallel (**Figure S2)** and perpendicular (**Figure S3**) orientations in Autodesk Simulation software. The model of gold/graphene/gold composite structure was created with respective geometries and material properties assigned. The gold/graphene interface was modeled as a layer of material of minimal thickness with the ultimate strength equal to that of graphene/gold adhesion strength (~40 meV per carbon atom). **Figures S2** and **S3** plot both the strain and the safety factor present at the initial stages of the process of cutting into graphene. Safety factor is identified as the ratio of absolute strength to the applied load and is indicative of where critical failure is likely to occur (areas with safety factor values below 1). **Figure S2a** is the representative rendering of the parallel sectioning. **Figure S2b** represents the safety factor distribution in the composite sectioned parallel. As the diamond blade makes contact with graphene (**Figure S2c**), additional loading causes critical failure and crack propagation along the gold/graphene interface (marked with yellow oval) and plastic flow within the gold wire (marked with red oval) prior to the critical failure in the graphene sheet. Thus sectioning the composite parallel results in partial delamination of the two gold wires along the gold/graphene interface with the slight deflection of the gold wire bearing graphene. **Figure S2d** represents the XX (x-normal) strain tensor and identifies the location of the cut through the gold wire. Note the absence of the x-component of strain on the failing gold/graphene interface indicating pure tensile failure at the interface. As seen in **Figure S3a-c**, sectioning the composite perpendicularly also imposes strain on the gold/graphene interfaces and suggests failure at those sites. But these interfaces are strained compressively (**Figure S3c**) and no delamination is possible, thus the resultant wires present no opening at gold/graphene interface on the sheared face.

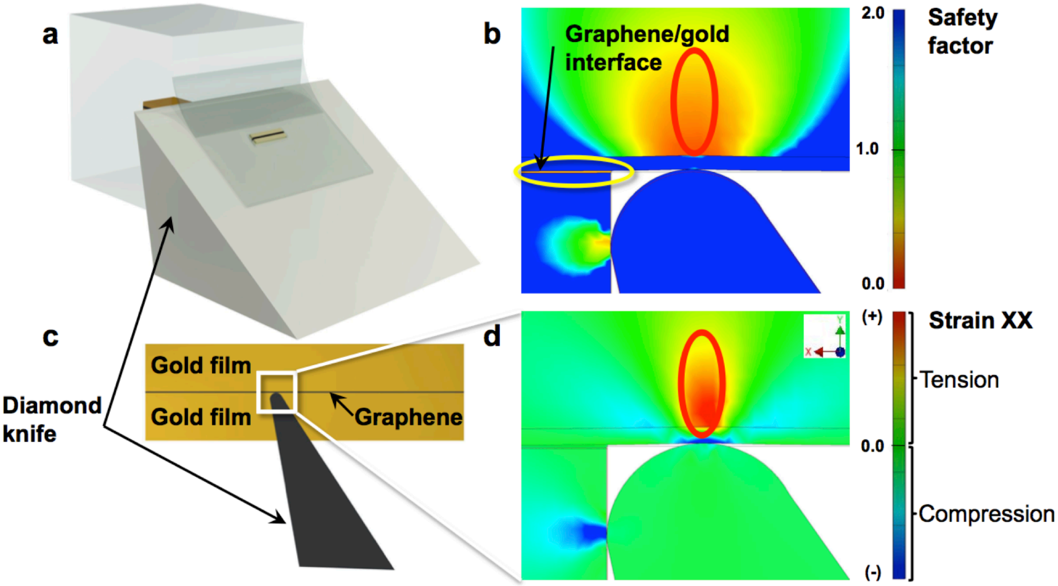

Figure S2. Representation of skiving the gold/graphene/gold composite in the parallel orientation (a,c). Finite element analysis simulation of skiving the gold/graphene/gold composite parallel (b,d). Safety factor plot (b) indicates the areas of structural failure (shear – circled red, and tensile – circled yellow) as the knife is sectioning the composite across the gold/graphene interfaces. XX Strain tensor (x-normal) is plotted in inset (d) and indicates the classical skiving compression zone (blue) and the plastic flow (red) of the gold film preceding the blade.

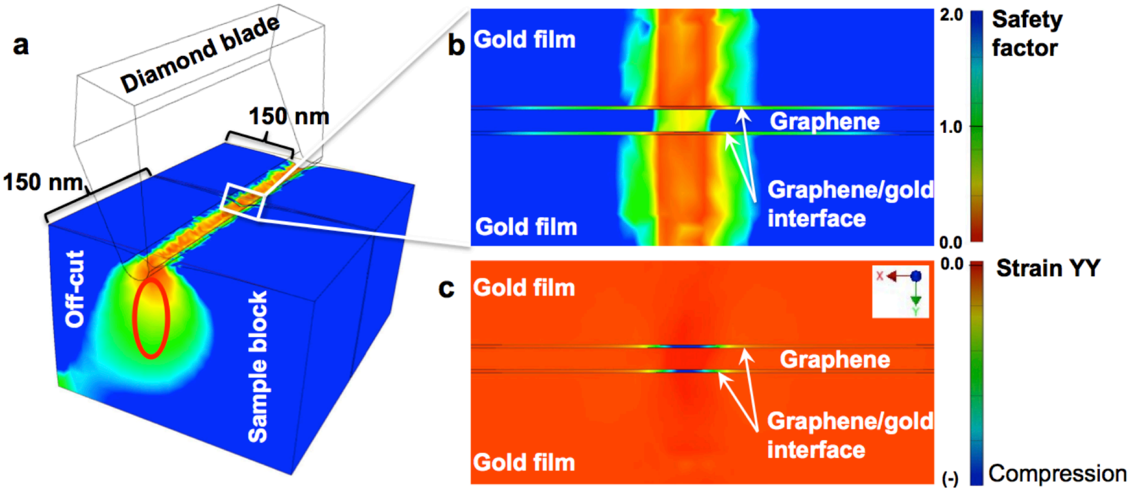

Figure S3. Finite element analysis simulation of sectioning the gold/graphene/gold composite in the perpendicular orientation. Safety factor plots (a, b) indicate the areas of structural failure (shear) – circled red – as the blade is skiving the composite along the gold/graphene interfaces. For the image clarity, (a) is flipped vertically (naturally, in ultra-microtomy, the knife is located below the sample block and cuts in an upwards motion). YY Strain tensor is plotted in inset (c) and indicates the compressive strain on the gold/graphene interfaces.

Scanning electron microscopy (SEM) imaging of the defects in the composite wires.

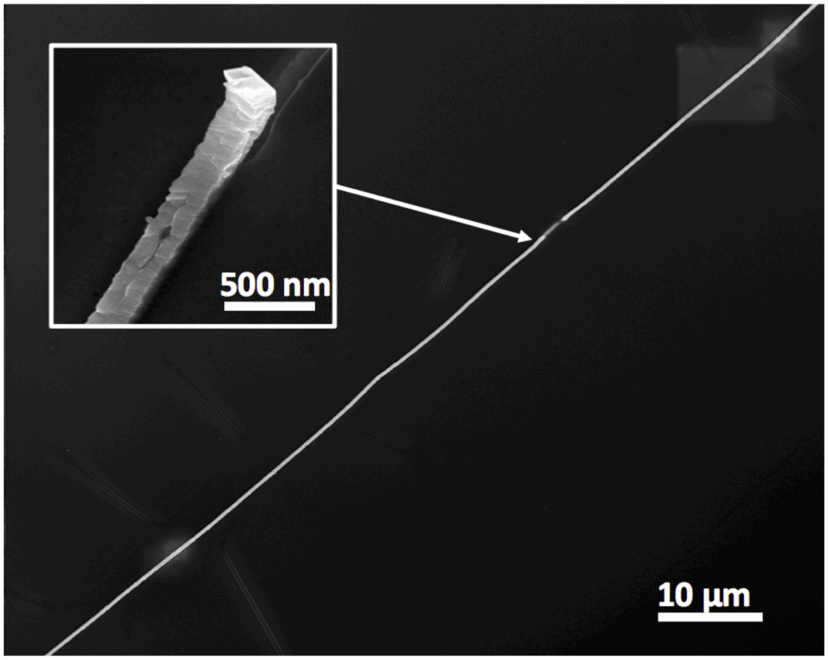

Figure S4. Scanning electron microscope image of a line defect in a perpendicularly-sectioned gold/graphene/gold composite nanowire. At the defect site, the nanowire delaminates from epoxy and deforms out of plane (inset).

Atomic force microscopy (AFM). AFM imaging of the gold/grahene/gold composite wires sectioned parallel (**Figure S5)** reveals that the gap is about 40 nm deep. Taking into consideration the radii of curvature of the AFM tip and the edges of the wires, the actual depth of the gap is predicted at about 50 nm **(Figure S5b inset).**

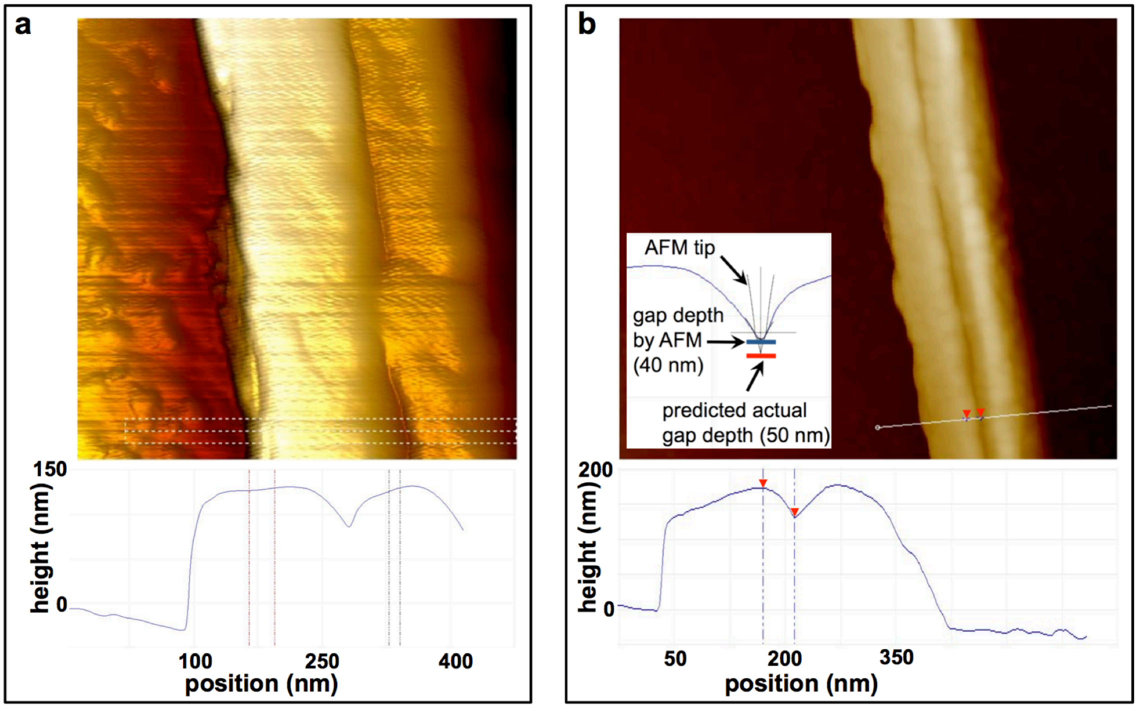

Figure S5. Atomic force microscopy image of the composite wire sectioned parallel.

Sample preparation for ultramicrotomy. To prepare gold/graphene/gold/epoxy composite films for ultramicrotomy sectioning after MAE, a 500 µm wide and 1 cm long strip was chopped off from the bulk of the composite film using a razor blade and a hammer, embedded in Epofix cold-setting epoxy resin and cured at room temperature for 24 hours to form a block (a parallelepiped 0.5 cm by 0.5 cm by 1 cm with the sample strip embedded in the bulk of the block). Further, a block face that is parallel to the short dimension of the embedded strip was tapered down to a 1 mm by 1 mm square bearing the embedded structure in its centre – the shape that determines the dimensions of the sectioned slabs. For sectioning, the block was placed into the holder chuck of the Reichert Jung Ultracut E ultramicrotome, a Diatome Ultra 2.5 mm 35° diamond knife was aligned with the block[4] for either parallel or perpendicular sectioning, and 150 nm-thick slabs were sectioned off the block at the rate of about 1 section per 1 second.

Oxygen plasma treatment of samples. To remove epoxy and graphene from the as-sectioned samples, the samples were etched in oxygen plasma for 3 hours at 200 mTorr, 30 W using a Harrick Plasma Cleaner.

Raman spectroscopy analysis. For obtaining the Raman spectra of as-sectioned and oxygen plasma treated wires, a Raman microscope (Renishaw inVia) with an inverted stage and with a 532 nm excitation source was used. The laser beam polarization was orthogonal to the long axis of the wires and focused to a 2 µm beam spot. The exposure was set to 10 seconds at 50 mW power. For obtaining the Raman maps and spectra of benzenethiolate on the samples, a 633 nm excitation source was used at 100 mW power and a 10-second exposure. Here, the laser was also polarized orthogonally to the length of the structures and focused to 2 µm spot size.

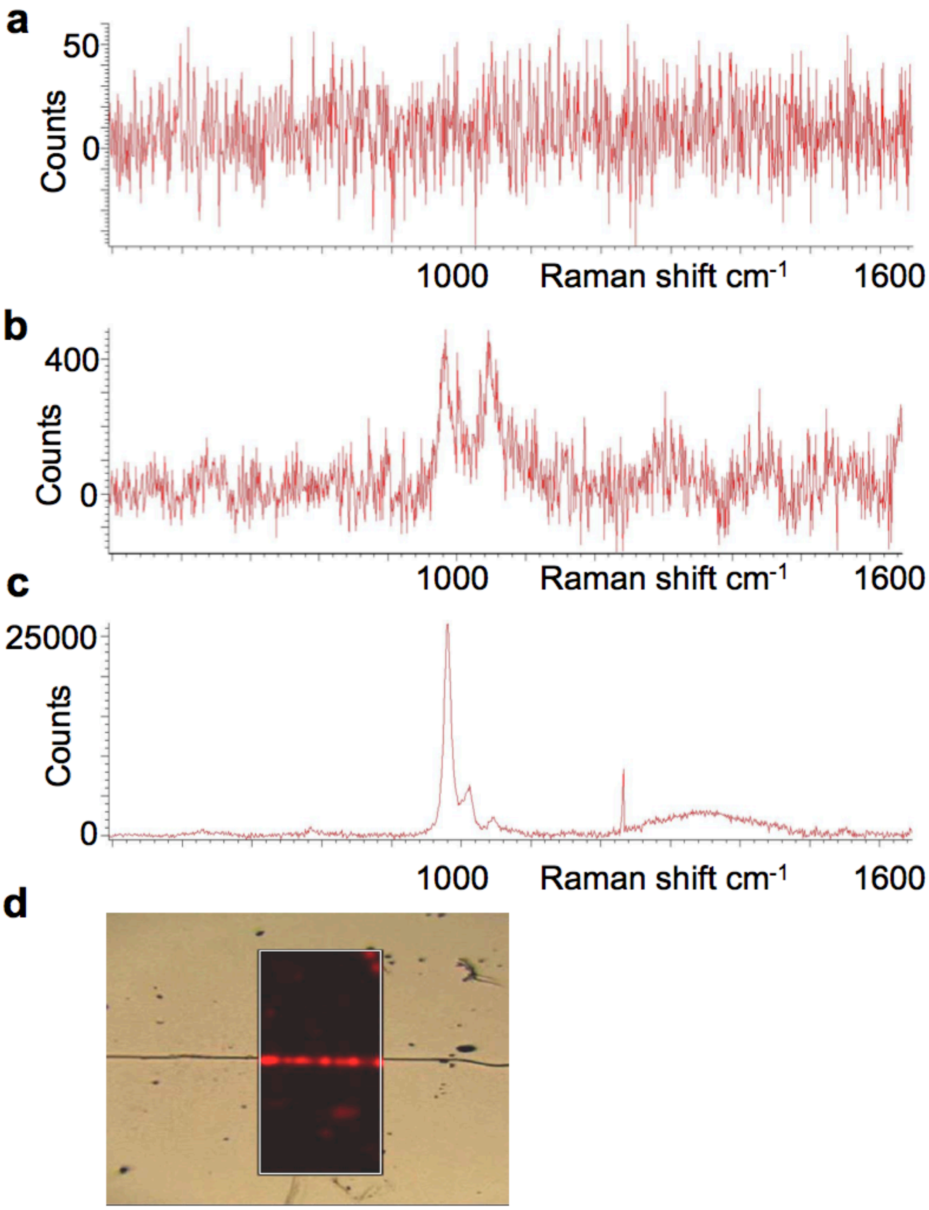

Figure S6. Raman spectra of 1-butane thiolate produced by: the gold-coated silicon wafer (**a**), 300-nm-wide gold wire on gold-coated silicon wafer (**b**), and the gold/graphene/gold composite wire on gold-coated silicon wafer (**c**). Raman map of 980 cm^{-1} 1-butanethiol peak of gold/graphene/gold composite wire (**d**).

References

(1) Vlassiouk, I.; Fulvio, P.; Meyer, H.; Lavrik, N.; Dai, S.; Datskos, P.; Smirnov, S. *Carbon N. Y.* **2013**, *54*, 58–67.

(2) Zhang, B.; Lee, W. H.; Piner, R.; Kholmanov, I.; Wu, Y.; Li, H.; Ji, H.; Ruoff, R. S. *ACS Nano* **2012**, *6*, 2471–2476.

(3) Li, X.; Zhu, Y.; Cai, W.; Borysiak, M.; Han, B.; Chen, D.; Piner, R. D.; Colomba, L.; Ruoff, R. S. *Nano Lett.* **2009**, *9*, 4359–4363.

(4) Xu, Q.; Bao, J.; Rioux, R. M.; Perez-Castillejos, R.; Capasso, F.; Whitesides, G. M. *Nano Lett.* **2007**, *7*, 2800–2805.

Appendix B

Supporting Information for Chapter 4

Metallic Nanoislands on Graphene as Highly Sensitive Transducers of Mechanical, Biological, and Optical Signals

Aliaksandr V. Zaretski[1], Samuel E. Root[1], Alexander Savchenko[2,3], Elena Molokanova[4], Adam D. Printz[1], Liban Jibril[1], Gaurav Arya[1], Mark Mercola[2,3], and Darren J. Lipomi[1*]

[1]Department of NanoEngineering, University of California,
San Diego, 9500 Gilman Dr., La Jolla, CA 92093-0448
[2]Department of Bioengineering, University of California,
San Diego, 9500 Gilman Dr., La Jolla, CA 92093-0412
[3]Sanford-Burnham Medical Research Institute,
10901 N Torrey Pines Rd., La Jolla, CA 92037
[4]NTBS, 309 Hestia Way, Encinitas, CA 92024
*Correspondence to: dlipomi@eng.ucsd.edu

Supporting Information:

Metallic Nanoislands on Graphene as Highly Sensitive Transducers of Mechanical, Biological, and Optical Signals

Aliaksandr V. Zaretski[1], Samuel E. Root[1], Alexander Savchenko[2,3], Elena Molokanova[4], Adam D. Printz[1], Liban Jibril[1], Gaurav Arya[1], Mark Mercola[2,3], and Darren J. Lipomi[1]*

[1]Department of NanoEngineering, University of California, San Diego, 9500 Gilman Dr., La Jolla, CA 92093-0448

[2]Department of Bioengineering, University of California, San Diego, 9500 Gilman Dr., La Jolla, CA 92093-0412

[3]Sanford-Burnham Medical Research Institute, 10901 N Torrey Pines Rd., La Jolla, CA 92037

[4]NTBS, 309 Hestia Way, Encinitas, CA 92024

*Correspondence to: dlipomi@eng.ucsd.edu

Graphene synthesis

Cleaning the copper foil. Graphene was synthesized on 25-µm-thick copper foils (Alpha Aesar, 13382, 99.8%) with the dimensions of 10 cm × 11 cm. Prior to the growth of graphene, we cleaned the copper foils by soaking them in a shallow acetone bath and wiping them with a Kimwipe tissue (while in acetone). After that the foils were rinsed with acetone and transferred into a similar bath filled with isopropyl alcohol (IPA), mechanical cleaning was repeated in this solvent. We note that the mechanical cleaning resulted in more pristine graphene than after cleaning the foils via sonication in acetone and IPA[1]; this method also saved a considerable amount of the both solvents (considering the large volumes required for sonicating large-area copper foils). After the mechanical cleaning in IPA, the foils were rinsed in IPA and dried in a stream of compressed air.

Electropolishing the copper foil. In order to generate mostly single-layer graphene, we found it necessary to electropolish the copper foils prior to graphene synthesis.[1,2] The clean, dry copper foil was placed into a 250-mL beaker, following the contours of the beaker side-walls, and was used as the anode. A copper pipe (*d* = 2.54 cm, *l* = 15 cm) was inserted into the beaker along the cylindrical axis and used as the cathode. The cylindrical shape of the cathode and the curved surface of the anode generated a uniform electric field during the electropolishing. Concentrated phosphoric acid (H_3PO_4, 15 M) was used as the electrolyte and was poured into the beaker after the cathode and the anode were secured with a clamp and an alligator clip respectively. A 20 W DC power supply was used to generate the necessary current and voltage. The voltage was set at 1.6 V and electropolishing proceeded until the current fell 50% and plateaued from the initial value (usually between 5 – 10 min). After the electropolishing, the cathode and the electrolyte were removed from the beaker and the copper foil was extensively rinsed with DI water (3 min). Then the copper foil was rinsed with IPA, blow-dried under a stream of compressed air, and immediately loaded into the middle of the quartz tube of a chemical vapor deposition (CVD) reactor.

Synthesis of graphene. Atmospheric-pressure CVD graphene synthesis[3] was performed in a quartz tube furnace (MTI OTF-1200X-HVC-UL) with the following tube dimensions: *d* = 7.6 cm, *l* = 100 cm. The CVD chamber and the reactor gas-supply lines were purged of air for 5 min by flowing a mixture of all synthesis gases (hydrogen, methane, and argon) at their maximum flow rates while pulling vacuum on the chamber with a diaphragm vacuum pump. After 5 min, the gas flow was stopped and the chamber was evacuated to about 10^{-4} torr with a turbomolecular vacuum pump in order to remove methane and hydrogen from the gas-mixing and the reactor chambers as well as to desorb the possible organic contaminants from the surface of the copper foil, then the furnace was than heated to 730 °C. The chamber was then re-pressurized to atmospheric pressure with ultra-high purity argon (700 SCCM), which flowed constantly throughout the entire procedure of graphene synthesis. The copper foils were heated in argon flow to 1050 °C (30 min). Upon reaching this temperature, additional hydrogen (60 SCCM) was flowed for 60 min to anneal and activate the copper substrate. After the 60 min of annealing, the flow rate of hydrogen was reduced to 5 SCCM. After 30 min, 0.3 SCCM of methane was flowed for 40 min for the synthesis of graphene (total gas flow rate: 700 SCCM argon + 5 SCCM hydrogen + 0.3 SCCM methane = 705.7 SCCM). After 40 min, the flow rate of methane was increased to 0.7 SCCM. After 60 min of total graphene growth time (with methane flow), the furnace was turned off and cracked open 5 cm (continuing the same gas flow). When the furnace cooled to 700 °C (ca. 5 min) it was opened to 10 cm. At 350 °C (ca. 30 min), the furnace was completely opened. At 200 °C, the hydrogen and methane flows were cut off and the reactor chamber was allowed to cool to room temperature in the argon flow (total cooling time was approximately 1 h). The synthesized graphene was analyzed via optical microscopy and a Raman spectromicroscope (**Figure S1**) and was determined to be of high quality and comprising a single-layer with few add-layers. Upon the completion of graphene synthesis, the copper foil bearing graphene was transferred into an oxygen plasma-treated Pyrex dish (to avoid contaminating the graphene with adventitious adsorbents from the ambient air) and evaporation of metal was immediately performed in a cleanroom environment.

Metal-assisted exfoliation (MAE)

In order to transfer graphene from copper onto other metals (gold, silver, and nickel), we used metal-assisted exfoliation (MAE) described by us elsewhere.[4] The formation of a conformal graphene/receiving metal interface in the high vacuum environment during MAE ensures that the interface is free from oxides and other contaminants and that the resultant morphologies after the subsequent nanoisland deposition are solely a function of the materials involved and the processing parameters.

Deposition of metal and self-assembly of nanoisland (NI) films

To compare the NI morphologies resulting from the selection of the underlying substrate, we used a Temescal BJD-1800 e-beam evaporator to deposit 10 nm of evaporant (gold or silver) onto graphene supported by copper, nickel, gold, and silver. The graphene-bearing substrates were fixed to the sample stage and positioned directly under the source of the evaporant (at distance of 40 cm). The metal evaporation rate was kept low (0.1 Å s^{-1}, as monitored by a quartz crystal microbalance) and the chamber pressure was kept at 7×10^{-7} torr during evaporation. The temperature of the substrate at the end of the evaporation was 400 K (further in text referred to as standard deposition conditions - SDC). The rate of evaporation and the temperature of the substrate are important parameters that determine the resulting morphology of the NI. We performed control evaporations of 10 nm of gold onto graphene supported by copper at 2 Å/s, 400 K and at 0.1 Å/s, 500 K. We have found that even though graphene offers very low diffusion barriers for gold and silver atoms, the faster rate of evaporation (2 Å/s as opposed to 0.1 Å/s) biases the process to be more kinetically-controlled and results in a less-structured morphology (**Figure S4**). Conversely, higher temperatures (500 K as opposed to 400 K) result in morphologies of higher crystallinity and lower area coverage (**Figure S5**).[5]

All samples were analyzed using the XL30 FEI SFEG UHR scanning electron microscope (SEM). By SEM imaging we have determined that the morphology on the

NI depends on the crystallographic orientation of the underlying substrate. **Figure S2** demonstrates the difference in morphology of AgNI resulting from deposition of 10 nm of silver onto graphene on copper substrate (at SDC) with two neighboring copper grains of different orientations. In order to determine if the number of graphene layers between the substrate and the evaporant influence the NI self-assembly, we deposited 10 nm of gold at SDC onto copper substrate bearing graphene with a greater density of ad-layers. Further, the copper/graphene/AuNI were coated with 1 μm of Parylene C using a PDS 2010 Parylene coater. Upon etching of the underlying copper, the Parylene/AuNI/graphene was imaged using the SEM (the AuNI were imaged through the underlying graphene). In **Figure S3** it is seen that the amount of percolation on the AuNI decreased on graphene bearing progressively more layers. This correlated well with the model for thin-film growth, since additional graphene layers sequentially lowered the surface energy of copper.[6]

We would like to note the repeatability of the AuNI morphology between samples for which depositions were performed at similar conditions (film thickness, rate of deposition, chamber pressure and temperature) and on similarly synthesized graphene (AuNI on copper in **Figures 1** and **S22**). In **Figure S22** it is seen that the AuNI morphology is consistent over the entire graphene sample of as large as 40 cm^2 in area. From this we conclude that the methodology described in this letter is applicable to large area substrates and is possibly limited in scale by the dimensions of the equipment utilized.

Transfer of graphene/NI films

For many applications, NI have to be transferred from the substrate upon which they were generated onto the final receiving substrate (optical fiber, glass slide, PDMS, PET, human skin, etc.). The transfer to glass coverslips, silicon wafers and strips of PDMS was performed following the well-established methodology for transferring graphene.[7] First, the supporting layer of PMMA (100 nm thick) was spin-coated onto copper/graphene/NI, followed by etching of the copper substrate in 1M iron (III) chloride (FeCl3) for 1 hour. After this, the graphene/NI/PMMA film was free floating on the surface of the etchant and was scooped and transferred into a beaker containing deionized water (3 times, 5 min in each beaker) in order to remove contaminants residual from etching the copper. The graphene/NI/PMMA was then scooped with a piece of a silicon wafer for SEM analysis, (**Figure S7**). Strikingly, the morphology of the graphene/AuNI as transferred to the silicon wafer was very different than that before the transfer (**Figure 1**). The AuNI formed a completely percolated network and lost sharp crystal edges and corners in favor of rounded features. This effect is likely due to substituting (intermittently) the substrate with a high surface area (copper, 1650 mJ/m^2) from under graphene/AuNI for water with a low surface energy (72 mJ/m2). The stabilizing substrate crystallinity also disappears with etching of the copper. At this stage, the AuNI apparently reconstruct into the most thermodynamically favorable configuration and likely retain it upon their placement onto the final receiving substrate. Note that this drastic reconstruction occurs in STP conditions. A free-floating film consisting of graphene/NI/polymer (**Figure S16**) can be deposited onto a substrate in one of two ways: the final receiving substrate interfacing with the graphene or conversely with the supporting polymer. In the first case, the substrate has to first be submerged into the DI water and slowly lifted out of the water picking up the floating composite film in a Langmuir-Blodgett fashion (optical fibers, glass coverslips and PDMS strips were coated in this way for Raman sensing, rigid substrate and flexible substrate strain sensing respectively). In the second case, the substrate is plunged into the floating graphene/NI/polymer film and further down into the water (**Figure S17**) (substrates for cardiomyocyte culture and contraction experiments and well as heart-rate monitoring were coated in this way). If sensors are supported by PMMA during transfer, this supporting polymer film can be easily removed with acetone. Noticeably, no supporting polymer was used for coating the tips of optical fibers with graphene/AuNI films, as the area of a tip (~0.03 mm^2) is significantly smaller than the fragments resulting from breakage of the unsupported graphene/NI film (when such breakage occurs).

In addition to the abovementioned transfer methods, a polymeric film can be laminated on top of the copper/graphene/NI film (e.g. with a commercial laminator) and thus serve as the supporting and final receiving substrate upon copper etching.[8] Such transfer was used by us to generate flexible strain sensors supported by 125 μm-thick polyethylterephtalate (PET) (**Figure S18c,d**).

Atomistic Physical Vapor Deposition Simulations

All simulations were performed using the open-source simulation package LAMMPS (12/09/2014)[9] as available on the Comet supercomputer at the San Diego Supercomputer Center. The simulations were accelerated with a dynamically load-balanced domain decomposition using a message-passing interface distributed on two compute nodes containing a total of 48 Intel Xeon processors. We achieved a parallel speed up of ~20× corresponding to an efficiency of ~ 5 ns/day. Visualization and post-processing analyses were performed using the open-sourced visualization tool, OVITO[10] along with a custom python module.

The initial configuration of the graphene/copper (111) surface was generated and equilibrated following the procedure of Süle et al.[11] Specifically, we chose to use a 3 × 3 Moiré super cell[12,13] with a thick copper support (30 layers) and fixed its bottommost layer to effectively model a bulk copper surface. A vacuum layer of height of 4 nm was inserted above the surface to deposit the gold atoms and provide space for the islands to grow. A reflective boundary condition was imposed in the vertical direction with periodic boundaries in the horizontal directions. A schematic of the initial simulation cell is provided in **Figure S21**.

Simulated gold deposition. To simulate the deposition process, gold atoms were introduced at random positions within the insertion plane of the vacuum region at a rate of 200 particles per ns with a velocity directed at the surface. This deposition rate was chosen due to computational constraints. Although it is orders of magnitude larger than the experimental rate, it is the best we can do to perform these simulations in a reasonable amount of time and is standard practice throughout the literature.[14,15] The particle velocities were sampled from the Maxwell-Boltzmann distribution at a temperature commensurate with the experimental evaporation temperature. The temperature of the entire system was maintained at 400 K throughout the deposition process using a Nosé-Hoover style thermostat[16] in an NVT ensemble with a time constant of 0.01 ps. The equations of motion were integrated with a time-reversible, measure preserving Verlet algorithm[17] using a time step of 1 femtosecond, which was found to result in numerically stable simulations.

Simulation of thermal annealing. Following the deposition process, the experimental vacuum annealing process was simulated by increasing the temperature to 500 K and allowing the gold islands to diffuse and aggregate until the morphology became stable (~15 ns). During annealing, the surface area of the gold clusters was monitored using the surface mesh modification[18] from the OVITO software package with probe sphere radius of 2.5 Å and a smoothing level of 20.

Interatomic Potentials. Due to the hybrid nature of the system, each pair-wise interaction was treated independently with an appropriate interatomic potential. The metal-metal interactions were all computed using the embedded-atom method, which has been extensively used and verified throughout the literature for metallic systems.[19] The carbon-carbon interactions were treated using an AIREBO potential,[20] which has been shown to be a good model for graphene[11]. Carbon-copper interactions were treated using an angle-dependent Abell-Tersoff potential[21], which was parameterized specifically for this system using high level density-functional theory calculations[11]. Finally, the carbon-gold interactions were treated using a Lennard-Jones potential (epsilon = 0.0341 eV, sigma = 3.003 angstrom),[22] which has been shown to provide an accurate description of the binding and diffusion of gold on graphene, so long as there are no defects or grain boundaries present (which is the case in this study). A summary of the interatomic potentials used can be seen in **Table S21**.

Statistical Analysis of Island Growth. The trajectory files output from the physical vapor deposition simulations provide a wealth of information that can be used to quantitatively characterize the morphological evolution and growth of the nanoislands. These metrics provide a basis for comparing different systems and can give insights into the physical mechanisms underlying island growth unattainable from experiments alone. One quantity that can be quite easily monitored is the coordination numbers of the individual gold atoms. To calculate this we used a custom python code to parse through snapshots of the trajectory file and calculate all the nearest neighbors for every gold particle using the bond length as a distance cutoff. **Figure S19** shows the evolution of the probability distribution of the coordination number of the gold particles as the islands grow. From these results, we see that after 0.5 nm of Au has been deposited the majority of the gold atoms have a coordination number of 6, which corresponds to the surface of the cluster. After 1 nm has been deposited, we see that the majority of the gold atoms have a coordination number of 12, which corresponds to the bulk of the clusters.

Another quantitative metric to characterize the gold island growth is the distribution of the heights of the gold particles. These were calculated by binning the gold particles from a trajectory snapshot with respect to their vertical heights and normalizing the distribution. **Figure S10** shows the evolution of this probability distribution during the deposition process. We can see that with only 0.5 nm Au deposited, we have a maximum island height of 6 layers (22 Å). This result clearly demonstrates the preference of the gold clusters to bunch up instead of spreading out over the surface, likely due to more favorable gold/gold interactions versus gold/substrate interactions. We will use the above analysis to compare the effect of underlying substrate and deposited metal on island growth in future computational experiments.

Optical fiber Raman sensors

In order to study the feasibility of using the graphene/NI composite films as SERS substrates for label-free sensing, we transferred unsupported graphene/AuNI onto tips of freshly cleaved 300 μm-thick optical fibers (core: 50 μm in diameter, 50 μm-thick cladding, 50 μm-thick sheath). 7.5 nm of gold was evaporated onto graphene on copper in order to obtain non-percolated AuNI with minimal gaps between them (**Figure 3b, right inset**) (we have established 7.5-8 nm of Au deposition to be the percolation threshold for AuNI). After transferring the films and drying the fibers overnight in ambient air, they were placed into a beaker containing a 10 mM ethanolic solution of 1-butanethiol (BT) together with a 1 cm^2 piece of a silicon wafer with an evaporated 100 nm-thick film of gold (as a control substrate) in order to form a self-assembled monolayer (SAM) of BT on gold surfaces. After 24 h, the test substrates were thoroughly rinsed in DI water and isopropanol (IPA) and dried in ambient air.

Raman spectroscopy analysis. For obtaining the Raman spectra from the test substrates, a Raman microscope (Renishaw inVia) with an inverted stage and with a 785 nm excitation source was used. For both test samples and the control, the laser beam was focused to a 2 μm beam spot and the exposure was set to 60 seconds at 0.5 mW power. It is worthy to note that we were able to obtain distinct BT signals from the tips of the coated optical fibers (albeit with a low signal-to-noise ratio) even at as low as one second exposure, while no BT signal was obtainable at 60 s exposure even by raising the beam power to 5 and then to 50 mW. This indicates that graphene/AuNI are suitable SERS substrates and far superior to unstructured gold films.

Graphene/PdNI films as strain sensors

We have noticed that depositing ~10 nm of Pd onto graphene on copper under the SDC resulted in formation of a uniform monolayer of spherical particles (4-5 nm in diameter). We further transferred these graphene/PdNI onto rigid (glass), flexible (PET) and stretchable (PDMS) substrates (**Figure S18**) in order to test their piezoresistive properties over large range of strains.

PdNI sensors on rigid substrates. In order to evaluate the performance of PdNI as strain sensors under very low strains <<1%, 3-5 by 25 mm graphene/PdNI/PMMA strips were transferred onto 1 in × 1 in glass coverslips that were 130 μm thick. To remove PMMA, the slides were rinsed with acetone. To electrically address the sensor, copper wires (36 gauge) were adhered to the PdNI and glass coverslips with copper tape bearing conductive adhesive and drops of EGaIn were placed on the loose wire ends to ensure a stable electrical contact (**Figure S18a**). In all cases the aspect ratio of PdNI sensors after the attachment of electrodes was between 3 and 10 and unstrained resistance between 644 and 2015 Ohms.

To induce and register very small strains (0.001%-0.003%) with PdNI sensors, we placed 13 μm-thick polyimide (PI) tape (1 layer for 0.001% and 3 layers for 0.003% strain) onto a 2 in × 3 in glass slide. We then used the PI as a step of controllable height to create a cantilever by resting and fixing one half of the PdNI-coated glass coverslip on the tape while creating a gap between the coverslip and the glass slide under the other half of the coverslip (**Figure 3f**). By applying a small force (~0.1 N) to the free end of the cantilever and bringing it in contact with the glass slide, we bent the glass slide inducing tensile strains on its PdNI-coated surface and registered the resistance change with a Keithley 2400 source/meter using a custom-generated LabVIEW code (**Figure 3f, right inset**). Solid Pd film control samples were analyzed in a similar fashion (**Figure S15**).

PdNI sensors on stretchable substrates. To measure the piezoresistivity of PdNI sensors at higher strains (>1%), we transferred them onto strips of PDMS (3 mm × 10 mm × 100 mm), addressed them with copper wires and EGaIn, and used a high-precision linear actuator to stretch the PDMS (**Figure S18b**). Graphene (without PdNI) control samples were analyzed in a similar fashion. We cycled the sensors between 0% and 9% with 1% intervals (20 cycles per each 1% interval) (**Figure 3e**). The sensors exhibited very high gauge factors and cyclability while maintaining a stable baseline (**Figure S20**).

Heart rate measurements. In order to obtain biometric signals, we spincoated 8 μm-thick PDMS films on copper/graphene/PdNI, cured the PDMS on a hotplate at 100 °C for 10 min, and etched the copper in 1 M iron (III) chloride (1 h). Then we transferred the free-floating graphene/PdNI/PDMS films into DI water (3 times) and deposited the sensor onto the skin on the wrist (on top of the radial artery) (**Figure 3d**) by plunging the wrist into the vessel with the DI water and the sensor. The PDMS surface formed a good interface with the skin. Previously to depositing the sensor, we adhered a strip of an adhesive tape around the wrist while leaving a section of the skin above the radial artery tape-free. The adhesive tape served two purposes: it helped the attachment and keeping in place of the electrical contact wires and localized the strain on the tape-free section of the skin by rendering the tape-covered skin unstretchable. It is worthy to note that out of three sensors prepared this way, only one sensor was able to measure the heartrate while the other sensors generated wrinkles in PDMS during the transfer process and were not sensitive enough (although all three sensors were able to register wrist and individual digit motions with a high fidelity).

In-situ SEM on PdNI sensors. In order to register the film morphology of PdNI sensors under 0.001%, 3%, and 5% strains, we imaged them with the XL30 FEI SFEG UHR scanning electron microscope. To image the sensors under small strains on the rigid substrate, the PI tape step methodology was used. Here, instead of applying intermittent force on the cantilever, we permanently taped the free end of the cantilever to the glass slide with a conductive copper tape. This tape also served as an electrical ground electrode to discharge the sample to the SEM stage.

For obtaining the images of the sensor films under 3% and 5% strain, the sensors supported by 1 mm-thick PDMS strips were adhered to the curved surfaces of 3D-printed half-cylinders with the radii of curvature of 15mm and 10mm respectively (bending PDMS strips to the specified radii generated surface tensile strains of 3 and 5%) by using the adherent copper tape that also served to electrically ground the samples to the SEM stage.

Application-specific NI. We would like to point out the universality of the suggested platform in generating substrates for various applications. The selection of the optimal morphology and materials depends entirely on the application. Thus for a cellular biology sensing application, biocompatibility is potentially the greatest concern, so the metals are mostly limited to gold. This material limitation is also the case with the SERS sensing applications, where the metal has to be plasmonically active in the desired spectrum. Additional desired morphological traits for SERS sensing are morphologies with sharp features (plasmonic hot spots) and small gaps (ideally 1-3 nm). We believe that the ideal morphologies for strain sensors are those that would support the tunneling current piezoresistivity (for sensing extremely low strains) while providing the maximum coverage of the graphene area in order to “heal” the cracks generated by higher strains upon relaxation. For this reason, for strain sensing we found palladium NI to outperform the films bearing other morphologies.

Electrophysiology

Neonatal rat ventricular cardiomyocytes were isolated using the neonatal rat cardiomyocyte isolation kit (Worthington) and cultured at 37 °C with 5% CO_2. In brief, ventricles were dissected from 1-day-old Hsd:SD rats (Sprague Dawley), then digested overnight at 4 °C with trypsin. Digestion continued the following morning with collagenase for approximately 60 min at 37 °C. Cells were pre-plated for 90 min to remove fibroblasts, and plated on 12 mm glass coverslips coated with PMMA/AuNI/graphene in high-serum media (DMEM/F12 [1:1], 0.2% BSA, 3 mM sodium-pyruvate, 0.1 mM ascorbic acid, 4 mg/liter transferrin, 2 mM L-glutamine, 100 nM thyroid hormone (T3) supplemented with 10% horse serum and 5% fetal bovine serum) at 2×10^5 cells/cm^2. After 24 h, media was changed to low-serum medium (same as above but with only 0.25% fetal bovine serum). Three cell cultures were plated on PMMA/AuNI/graphene with at least 8 substrates in each cell culture. We coated several PMMA/AuNI/graphene substrates with Matrigel in each cell culture plating in order to compare the adhesion of cells to bare PMMA/AuNI/graphene substrates and those coated with Matrigel. We noticed no difference in cell adhesion and viability between the samples.

Scanning Electron Microscopy. First, cells were washed with 0.1 M phosphate buffer (pH 7.4), then fixed with 4% formaldehyde solution for 2 hours at room temperature, and washed with the same buffer three times for 5 min each. Following dehydration with graded series of alcohol (30% ethanol – 10 min, 50% ethanol - 10 min, 70% ethanol - 10 min, 80% ethanol - 10 min, 95% ethanol – 2 changes in 10 min, 100% ethanol – 3 changes in 15 min), all samples were freeze dried in a vacuum chamber, and coated with sputtered iridium. Scanning electron microscopy images were acquired on the XL30 FEI SFEG UHR at the working distance of 5 mm while using the 10 kV energy beam.

Electrophysiological measurements. A custom electrophysiology chamber was built by 3D printing a mold in which PDMS (Sylgard 184) was cured. The finished chamber had a central opening (for cell culture and media) and side openings (for eutectic electrode placement) and was placed on top of the glass coverslips bearing PMMA/AuNI/graphene and CM culture in a way that the central portion of the AuNI substrate was located in the central opening and the edges of the AuNI substrate were accessible for electrical addressing using EGaIn through the side openings (**Figure 4a**). The assembly was then sandwiched between two 1 in × 3 in glass slides and clamped with binder clips to ensure a good seal. A 5 mm aperture was pre-drilled in the top glass slide to allow adding media to the central opening of the chamber. The PDMS walls between the camber openings served to separate the EGaIn electrodes from the cell media (in mM, NaCl, 135; KCl, 2.5; $CaCl_2$, 2; $NaHCO_3$, 1; Na_2HPO_4, 0.34; KH_2PO_4, 0.44; glucose, 20; and HEPES, 10 (pH 7.4). Electrophysiological recordings were performed in current-clamp configuration using a Digidata 1322 interface, an Axopatch 200B amplifier, and pClamp software (Molecular Devices Corp.). The data were digitally sampled at 50 kHz and filtered at 2 kHz. Experiments were performed at room temperature. All traces representing individual contractions were fitted with exponential functions using Clampfit10.3 and OriginPro2015.

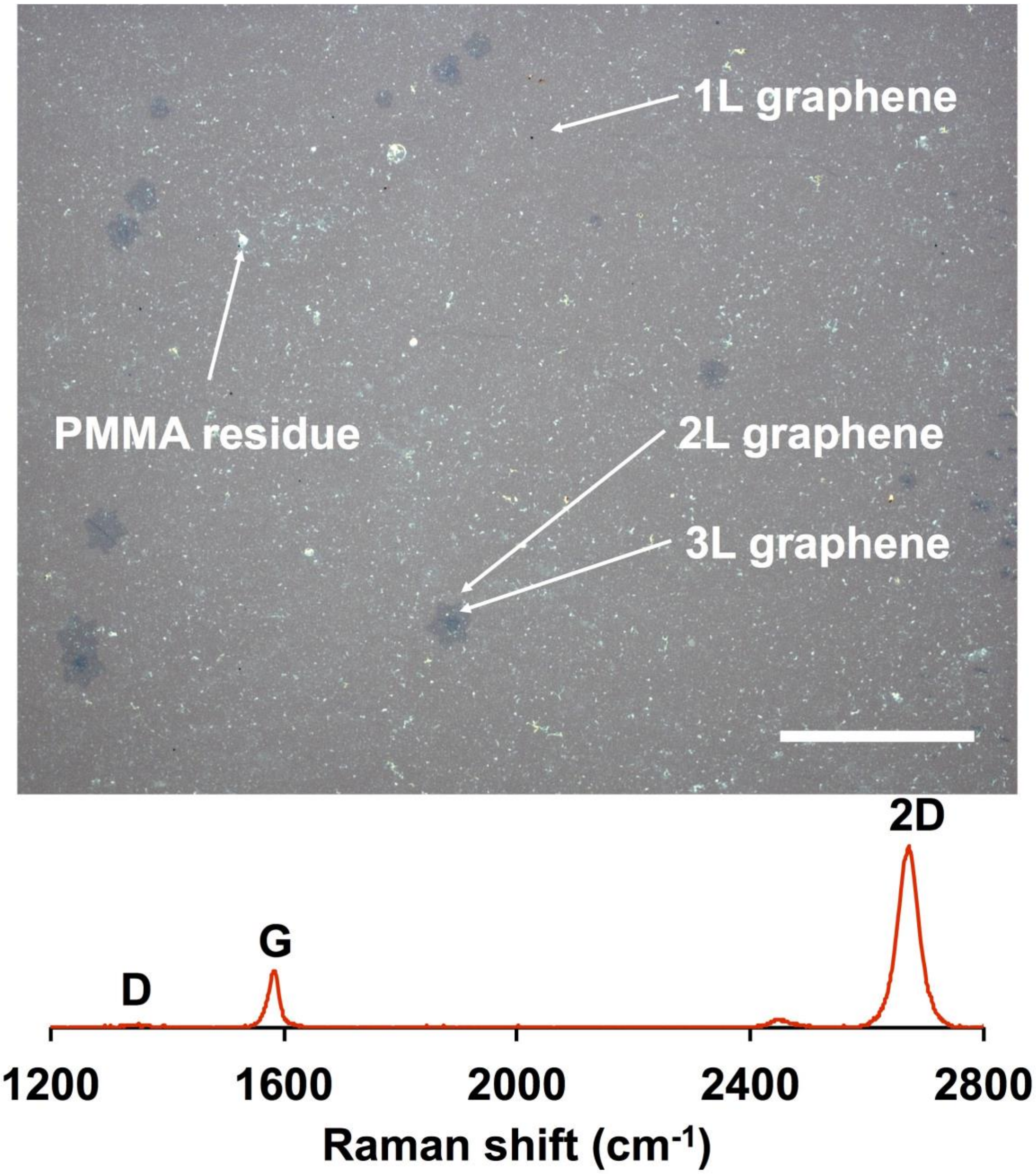

Figure S1 | Single-layer graphene. Optical micrograph of single layer CVD graphene wet-transferred to a silicon wafer with 90 nm thermal oxide (top). Scale bar: 100 µm. RAMAN spectrum of single layer CVD graphene wet-transferred to a silicon wafer with 90 nm thermal oxide (bottom). The ratii of the prominent graphene peaks indicate high-quality, predominantly single-layer graphene (D/G ratio: 0.019. 2D/G ratio: 3.1).

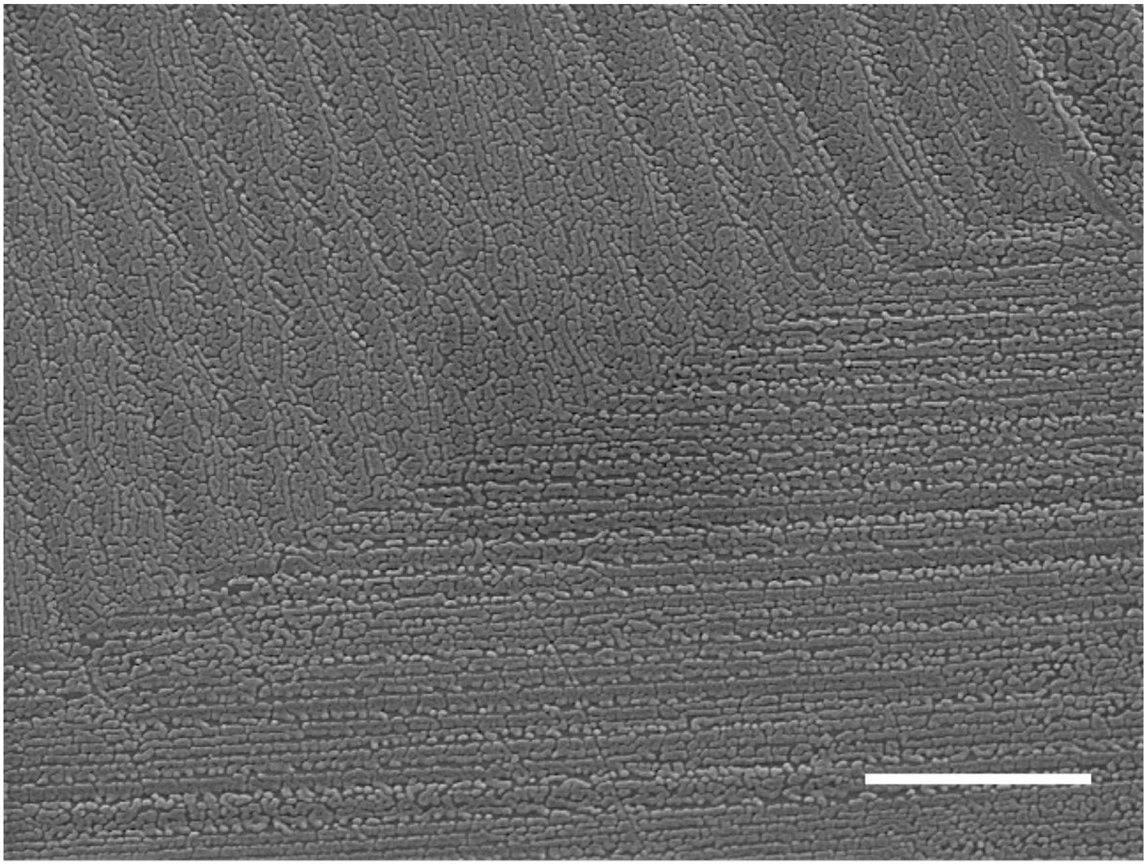

Figure S2. NI on different substrate grain orientations. Scanning electron micrograph of AgNI (10 nm deposition) on graphene on copper. Scale bar: 1 µm. Note the copper grain boundary diagonally across the image (from bottom left to top right) and the difference in AgNI morphology (percolation, level of anisotropy) on the respective copper grains.

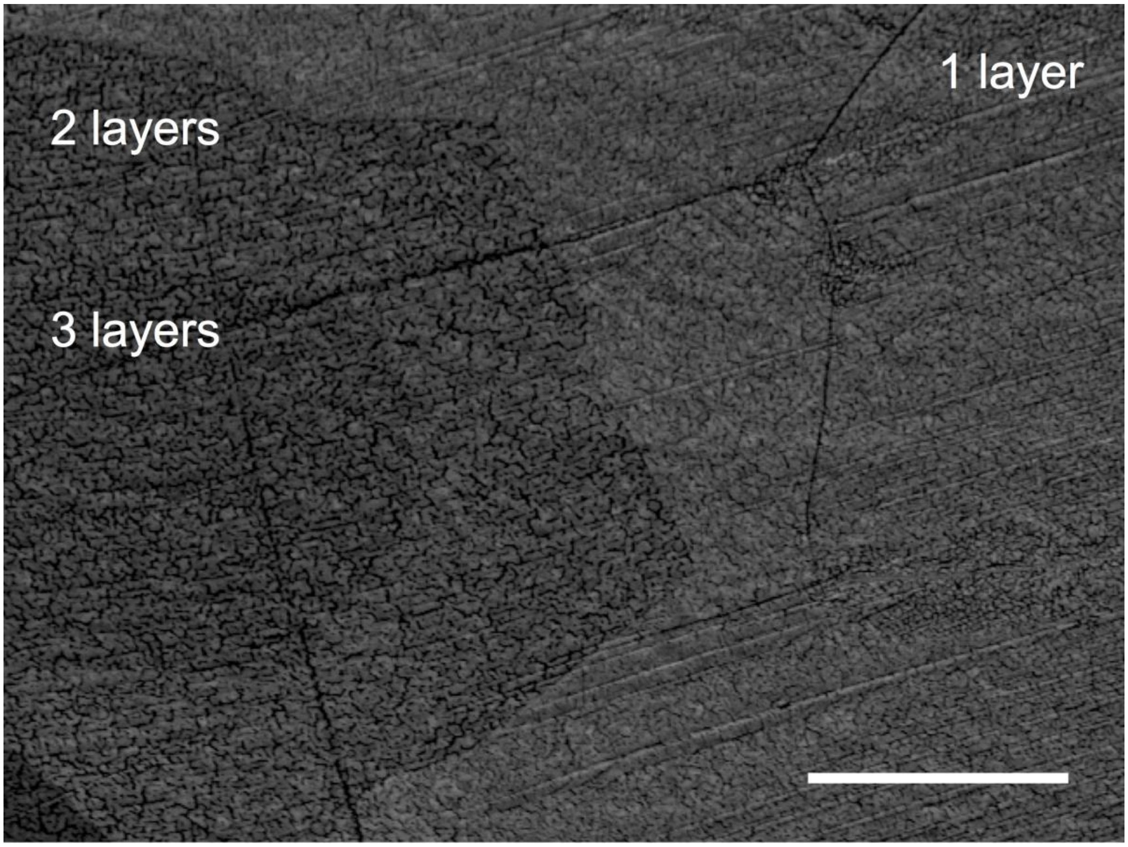

Figure S3. NI on multiple layers of graphene. Scanning electron micrograph of AuNI (10 nm deposition onto graphene on copper) on graphene transferred onto Parylene-C (etching copper after deposition of 1 µm-thick film of Parylene C (graphene is on top in this image and is covering the gold islands). Note the change in the amount of percolation in gold islands deposited over 1, 2, and 3 layers of graphene on copper. Scale bar: 2 µm.

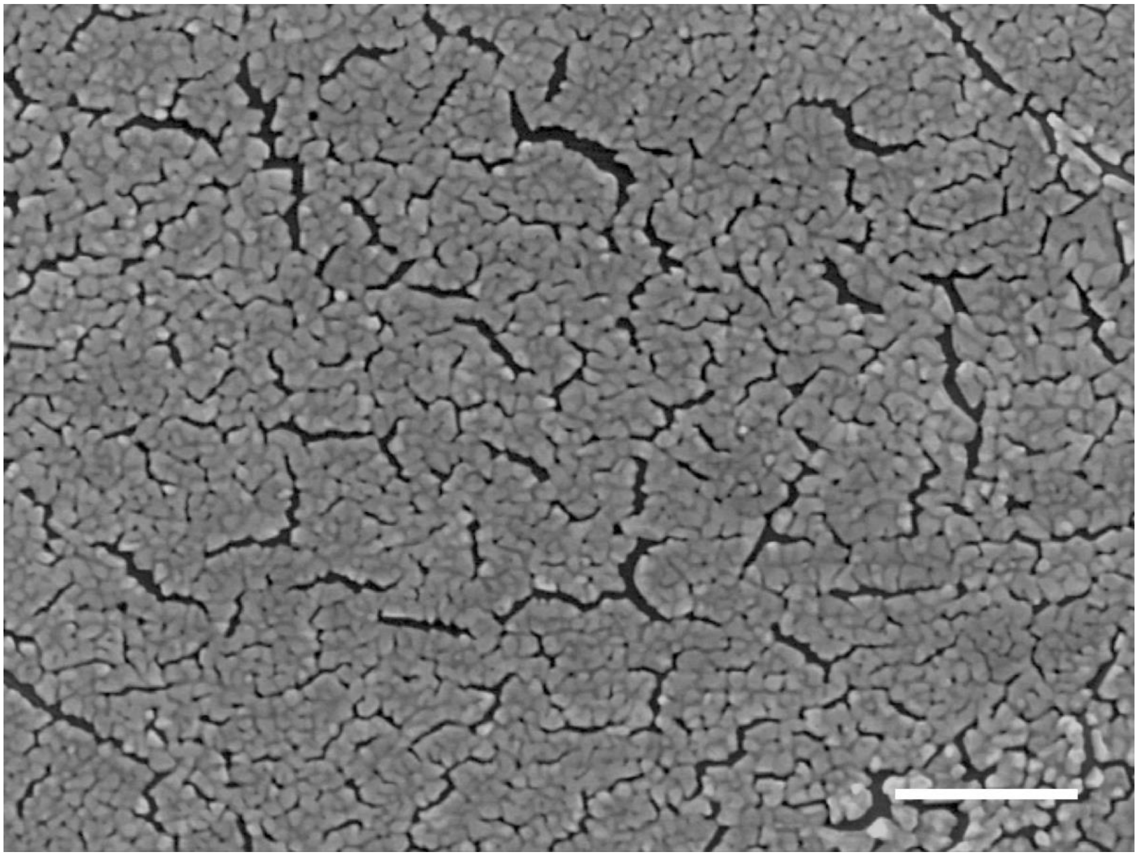

Figure S4. NI deposited at high evaporation rate. Scanning electron micrograph of AuNI (10 nm deposition) on graphene on copper deposited at the rate of 2Å/s. Compared to the slow rate of deposition (0.1 Å/s, **Figure 1, bottom**) the structure of the gold islands demonstrates significantly higher granularity, complete percolation, and significantly higher area coverage. Scale bar: 200 nm.

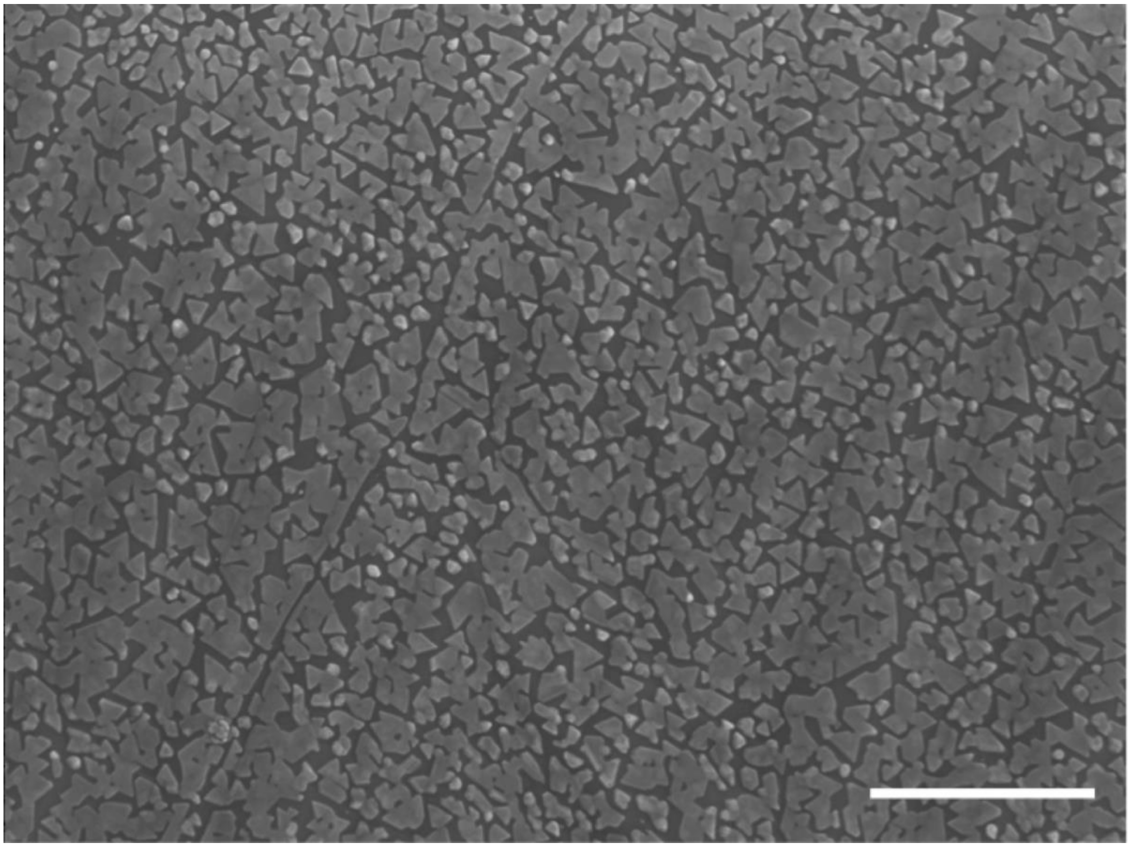

Figure S5. NI deposited at elevated temperature. Scanning electron micrograph of AuNI (8 nm deposition) on graphene on copper deposited at the rate of 0.1 Å/s and the substrate temperature ~500 K (100 K higher than SDC used in **Figure 1**). Scale bar: 500 nm.

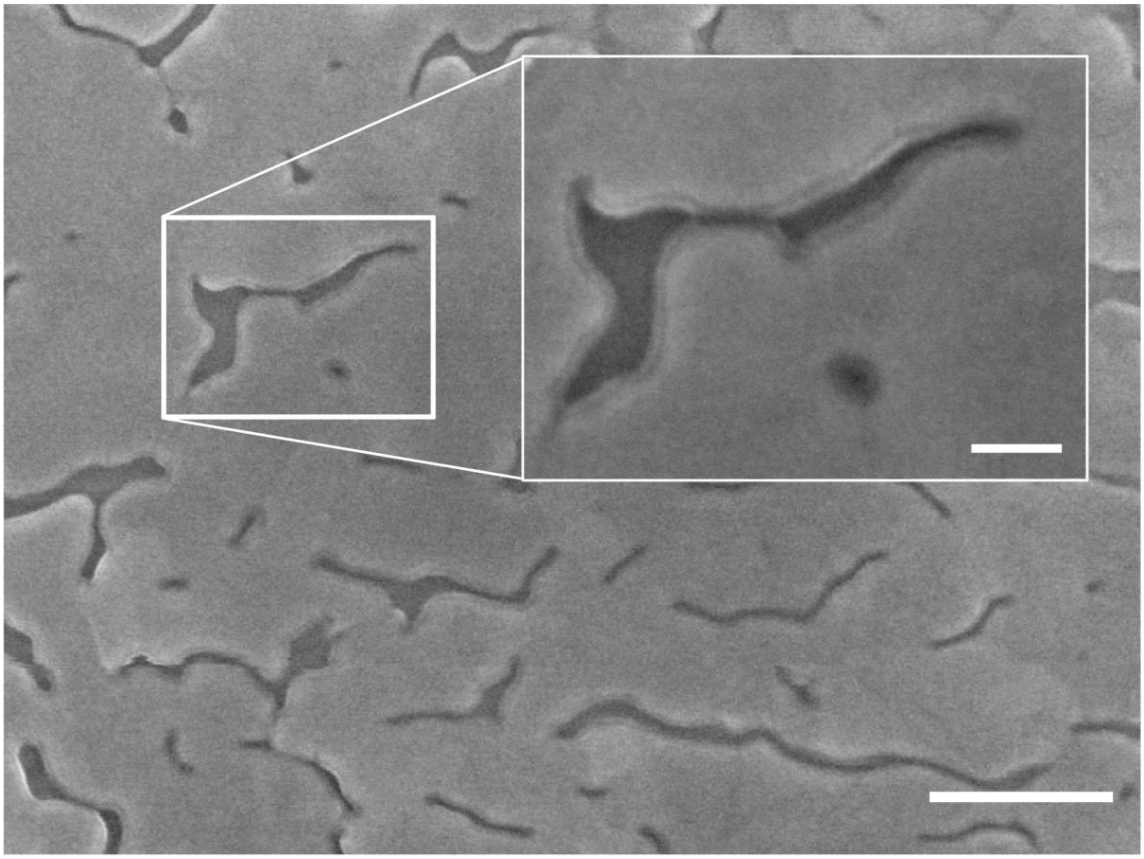

Figure S6. Thermal annealing of AuNI. Scanning electron micrograph of AuNI (10nm deposition) on graphene on copper foil after vacuum annealing at 600 K for 1 h. In comparison to the unannealed sample (**Figure 2, top left**), notice merging and spreading of the islands. Scale bar: 200 nm. Scale bar in inset: 50 nm.

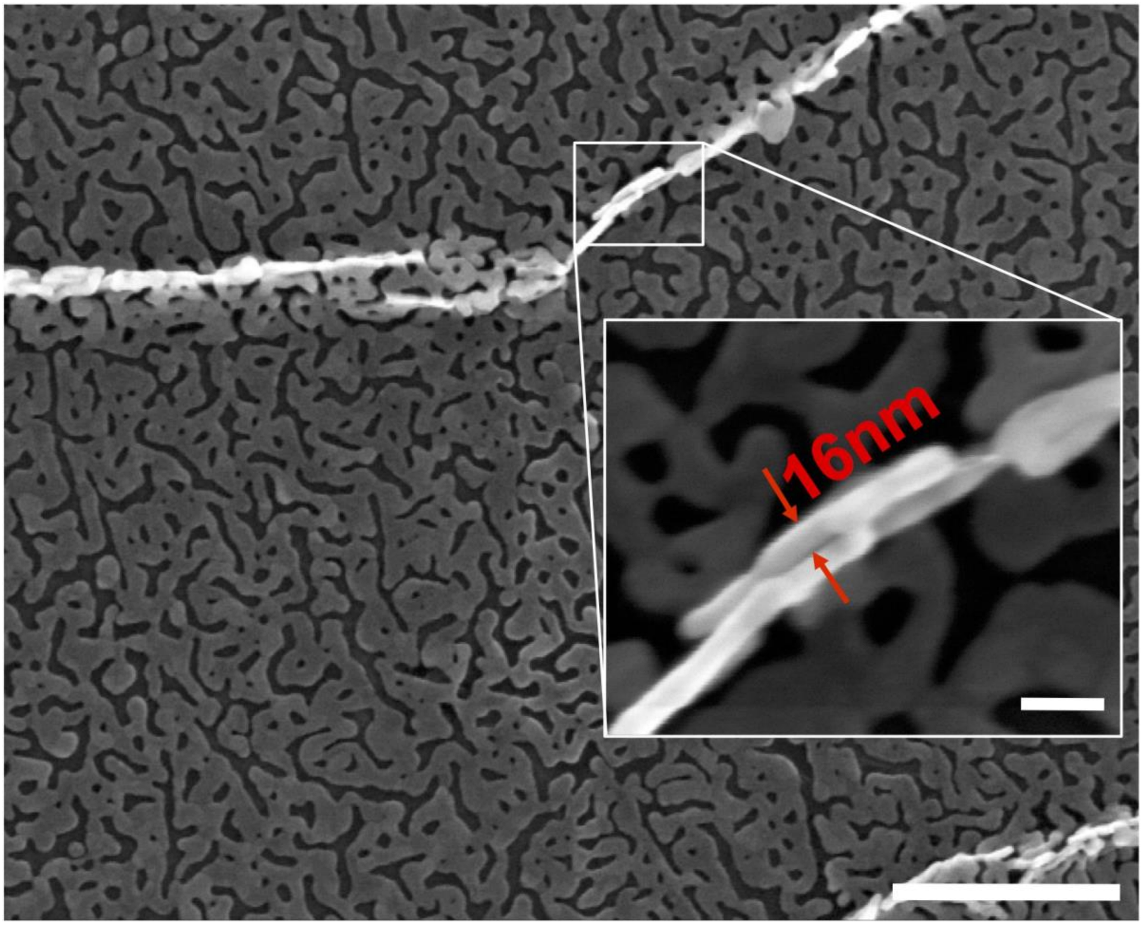

Figure S7. Wet transfer transforms AuNI. Scanning electron micrograph of AuNI (10nm deposition) synthesized on graphene on copper foil and transferred onto a glass slide. In comparison to the non-transferred sample (**Figure 1, bottom left**), notice merging of the islands into a completely percolated network and smoothing of the crystal facets. The metamorphosis is potentially due to etching of the copper substrate (surface energy 1650 mJ/m^2) away and floating the Au island/graphene film on the surface of water (surface energy 72 mJ/m^2) during the wet-transfer process. Notice wrinkles in graphene/AuNI as the result of wet transfer. Scale bar: 200 nm. Scale bar in inset: 50 nm.

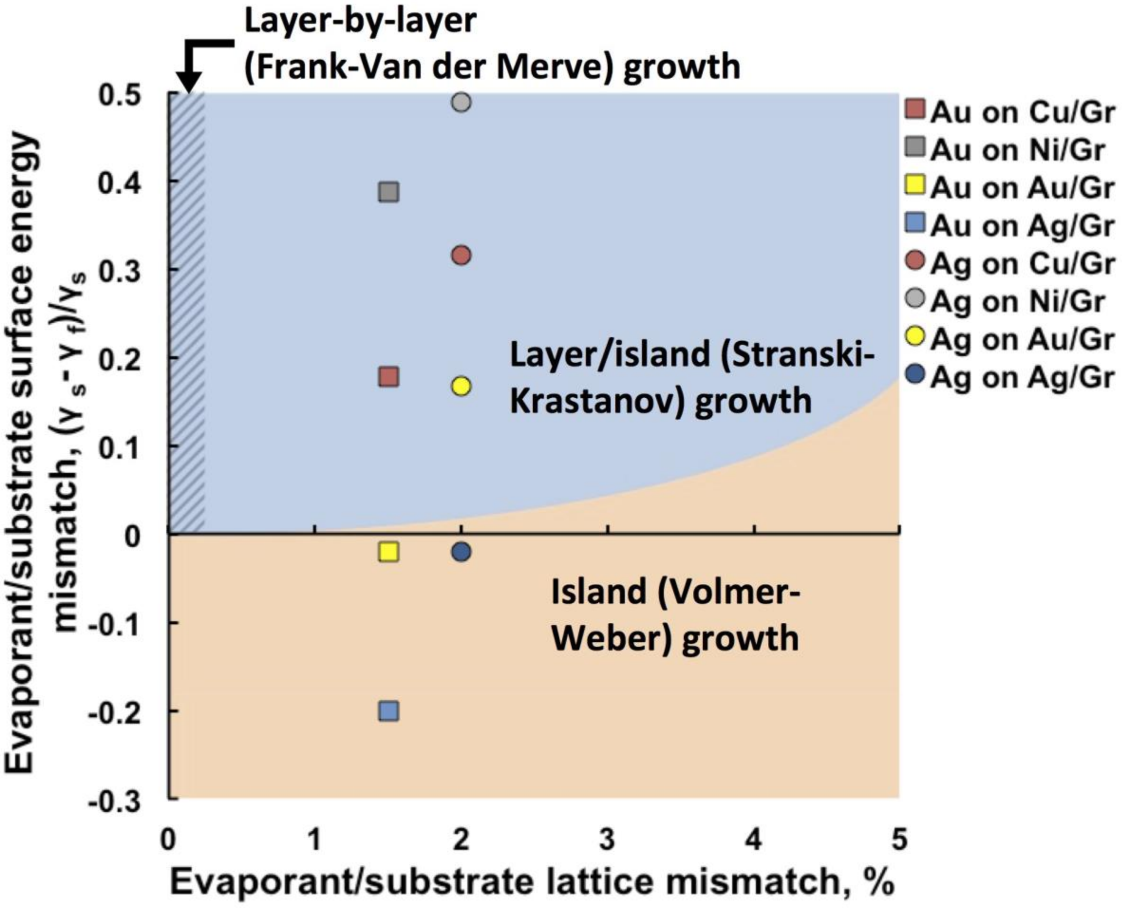

Figure S8. Thin-film growth model. Plot of the evaporant/substrate surface energy mismatch (vertical axis) vs. evaporant/substrate (graphene) lattice mismatch (horizontal). Stability regions of the three major modes of film growth are indicated on the plot: layer-by layer (cross-hatch), layer/island (light-blue), island (beige).[23] Note that due to the wetting transparency of graphene, the surface energy of the substrate was calculated as surface energy of the substrate metal less 2% (hence notice the vertical position of same-evaporant/same-metal substrate (Au on Au/Gr and Ag on Ag/Gr) at –0.02. The substrate lattice constant was taken as that of graphene (2.46 Å) (the effect of the strain (≈0.5%)[24] on graphene by the underlying substrates was negligible and not accounted for). This model does not take into account the Moiré patterns (first-order: substrate/graphene and second order: substrate/graphene/evaporant) that can possibly influence the nanoisland morphology. Notice a good accord of the model with the experimental results (**Figure 1, bottom**): higher degree of nanoisland percolation and graphene area coverage suggests the Stranski-Krastanov mode (Cu/Gr, Ni/Gr substrates), while the systems located in the Volmer-Weber stability zone (Ag on Ag/Gr, Au on Ag/Gr, and Au on Au/Gr) clearly have a purely nanoisland morphology.

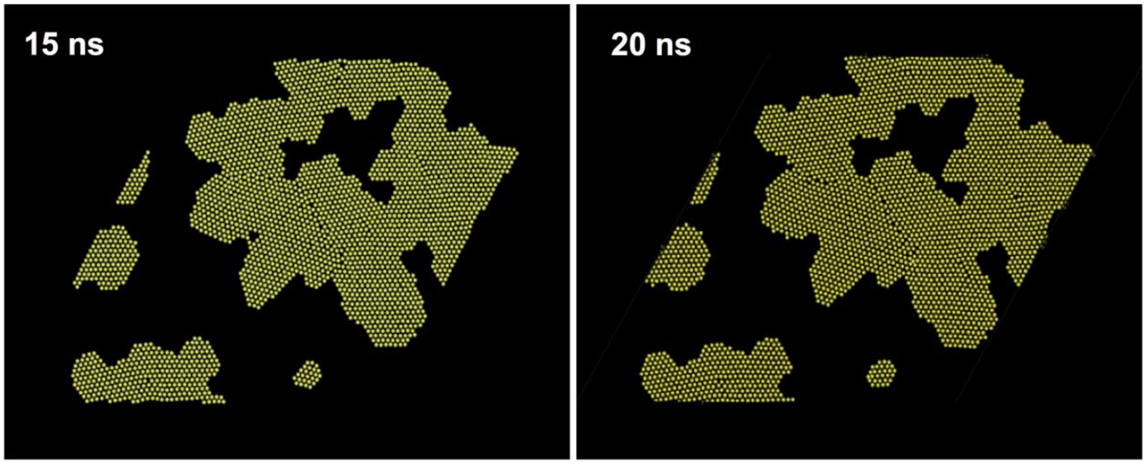

Figure S9. Monitoring graphene/gold interface events. LAMMPS simulation of thermal annealing (500°K) of gold nanoislands on graphene on copper. Represented is the reconstruction of the bottom layer of gold (in contact with graphene) over a 5 nanosecond-period during annealing. Notice the reconstruction on the grain boundary between the merged islands and point defect migrations.

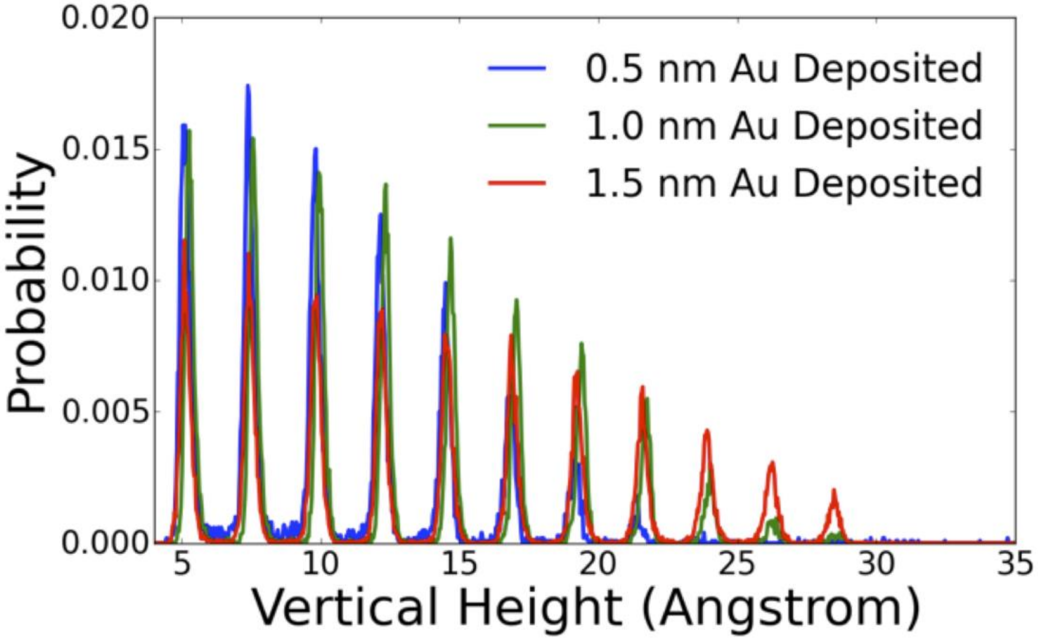

Figure S10. Monitoring AuNI height distribution during deposition. Simulated distribution of heights of AuNI (graphene and gold) during the deposition of 2 monolayers of gold.

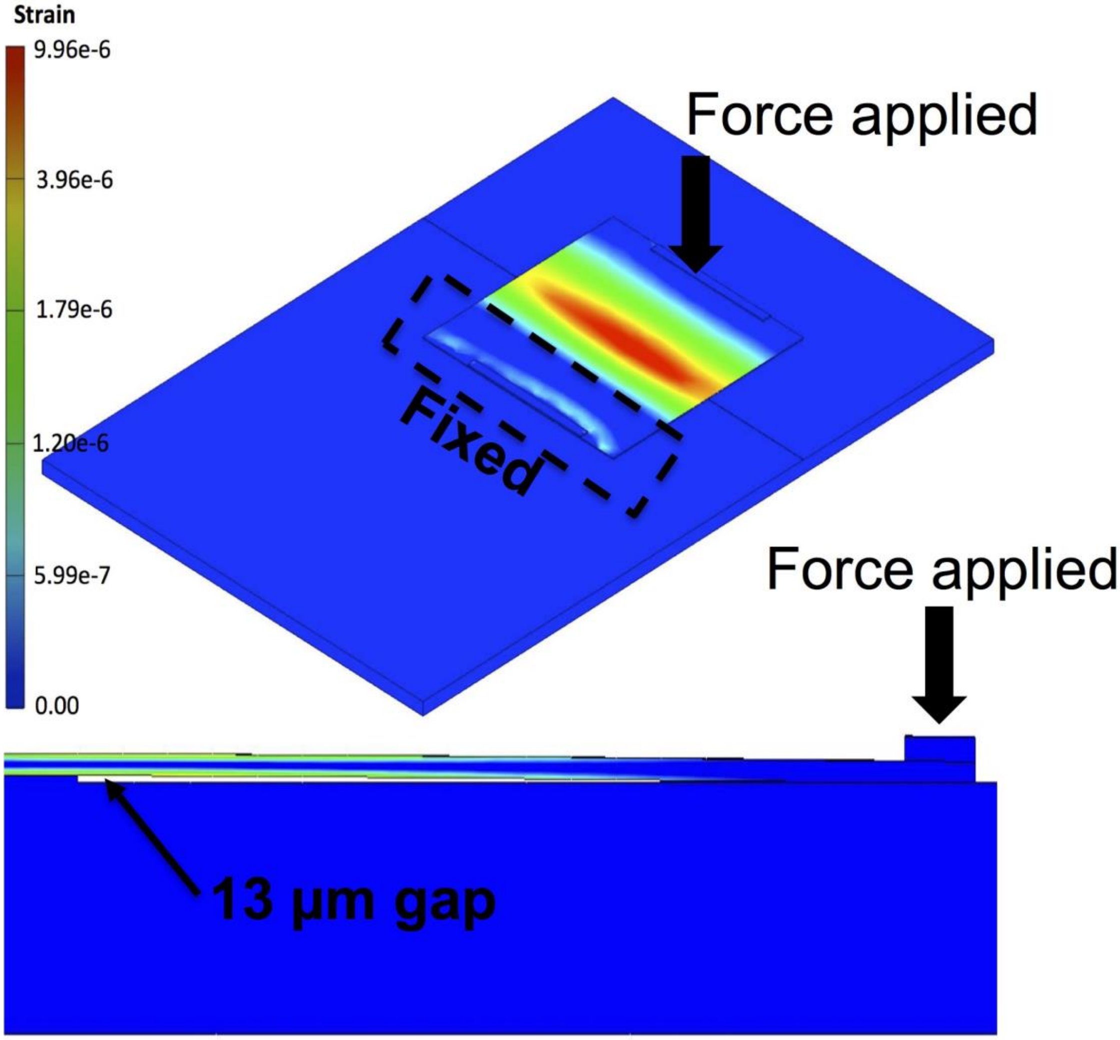

Figure S11. FEA of glass under small strain. Finite element analysis simulation of the equivalent strain on the glass cantilever bearing graphene/PdNI strain sensor after applying 0.1N force to the edge of the cantilever. The top surface of the cantilever experiences the maximal tensile strain of 0.001%

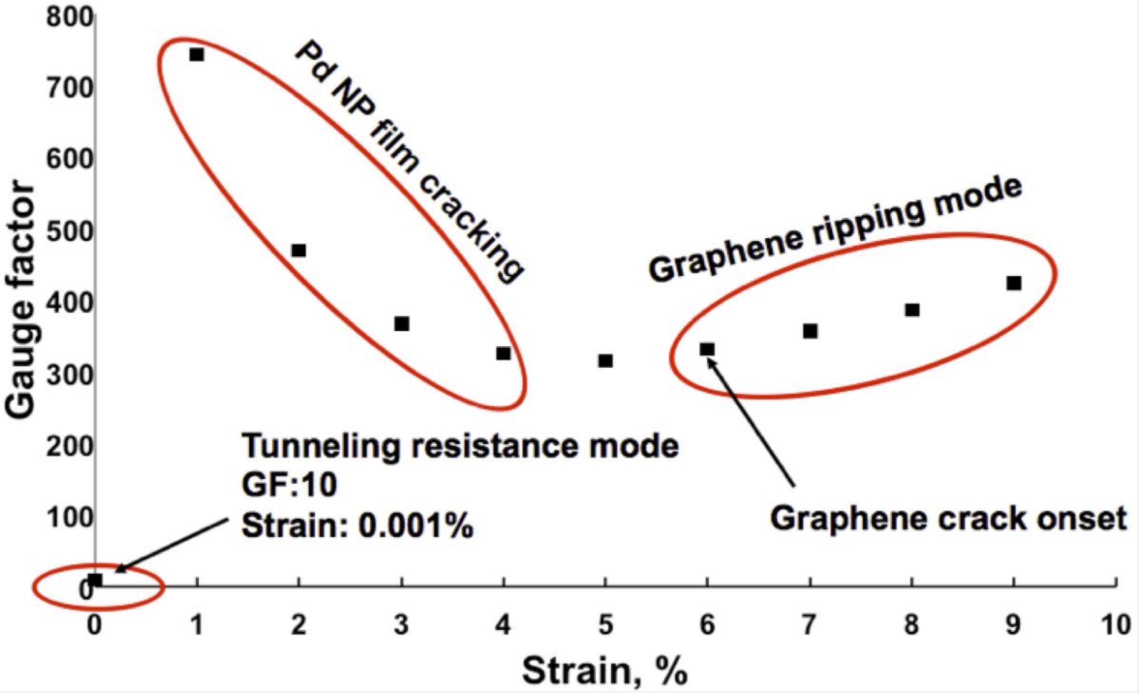

Figure S12. **Three sensing modes of graphene/PdNI sensors.** The plot of the gauge factor versus strain % for graphene/PdNI strain sensors indicates three major sensing modes: interparticle tunneling resistance modulation (<<1% strain), PdNI film cracking (<6% strain), and graphene cracking (>6% strain). Note that the lowest value for 0.001% strain was obtained by flexing 130 μm-thick glass slides bearing graphene/PdNI films (**Figure S18a**), while the rest of the values were obtained with sensors transferred to PDMS strips (**Figure S18b**).

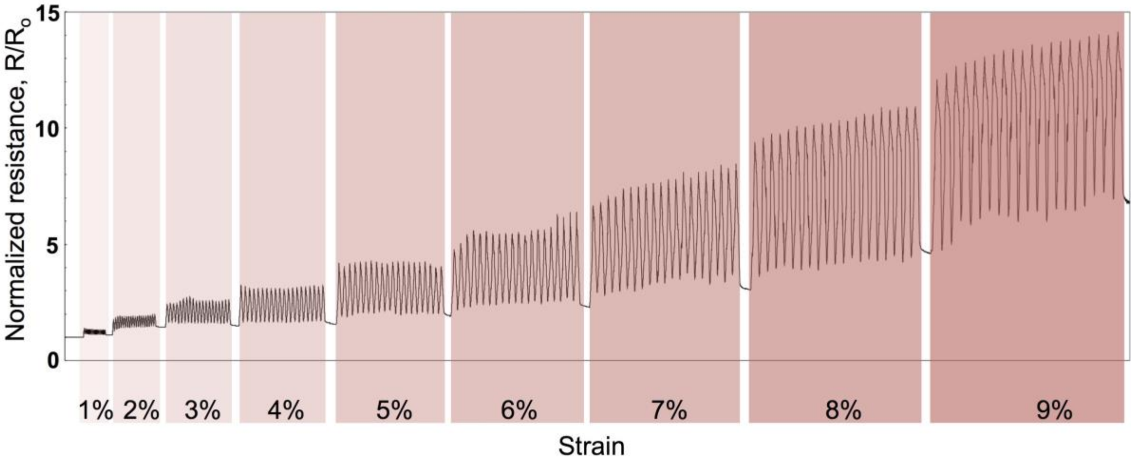

Figure S13. Graphene as strain sensor. Normalized resistance plot of graphene on PDMS stretched cyclically (20 cycles for each strain) to 1, 2, 3, … 9% strain. Notice that the baseline within a set of 20 strain cycles is stable until 6% strain is reached (graphene crack onset). The step-wise baseline shift between the sets of different cycles is due to the viscoelastic response of the PDMS substrate.

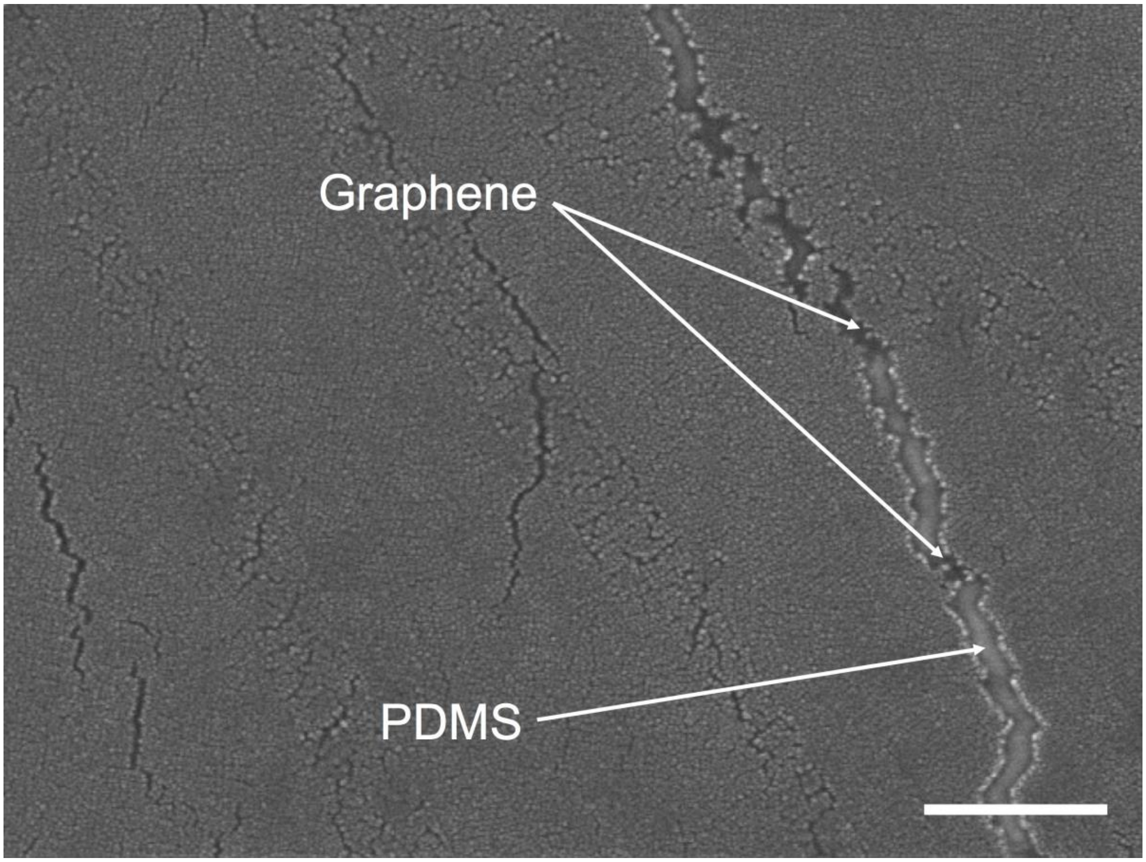

Figure S14. Graphene/PdNI sensor under 5% srtain. Scanning electron micrograph of the PDMS/graphene/PdNI strain sensor under tensile strain of ~5% (h). Scale bar: 200 nm.

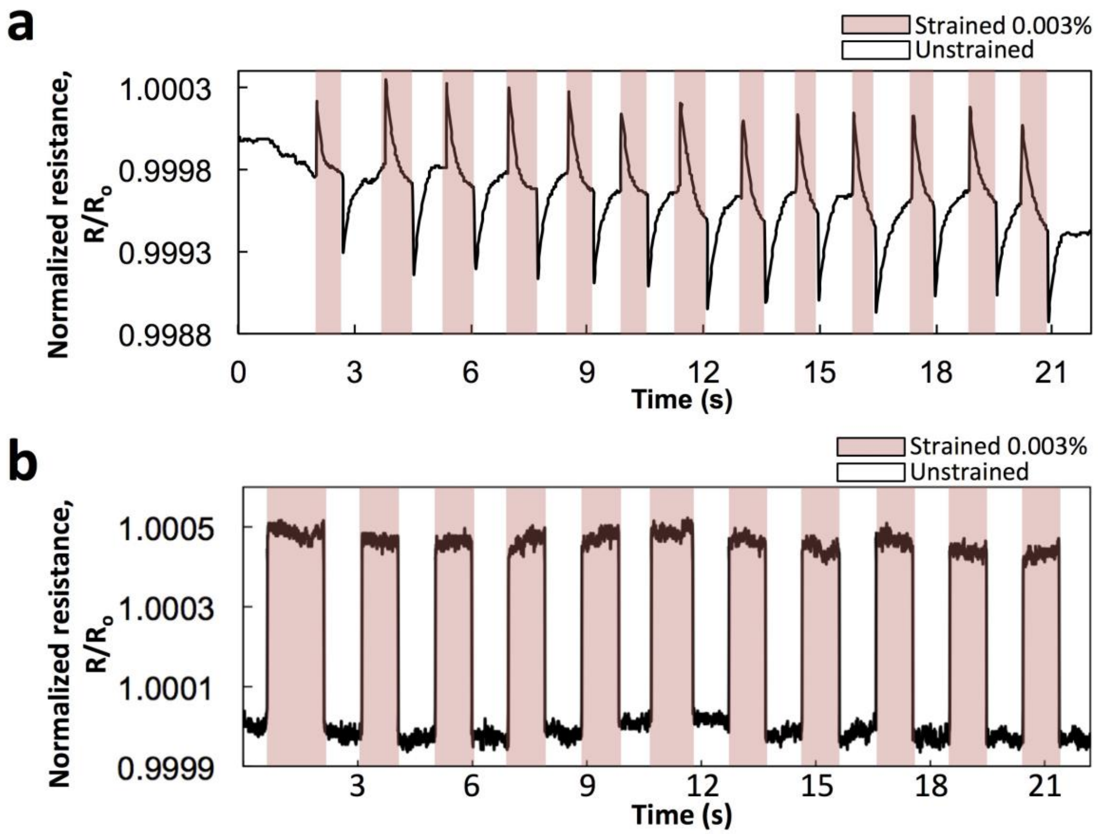

Figure S15. Solid Pd thin film sensor vs. graphene/PdNI sensor. Normalized resistance plots of solid (100 nm) film Pd strain sensor on glass coverslip under cyclic tensile strain of 0.003% (a) and the graphene/PdNI strain sensor on glass coverslip under cyclic tensile strain of 0.003% (b). Notice that at similar gauge factors (~17) at 0.003%, the PdNI sensor demonstrates stable behavior (holds the resistance value during the one second strain cycle), while the solid Pd film sensor registers the applied strain but does not hold the resistance value and reverts the it back to the baseline (upon returning the sensor into unstrained position, the resistance value drops and then reverts to the baseline during the one second unstrained cycle). This observation suggests that at very small strains (<<1%), the grain boundaries in the solid Pd film reconstruct to minimize the separation between the grains, which makes impossible to register static strains with such sensors. Conversely, PdNI sensors demonstrate good stability for static strain measurement.

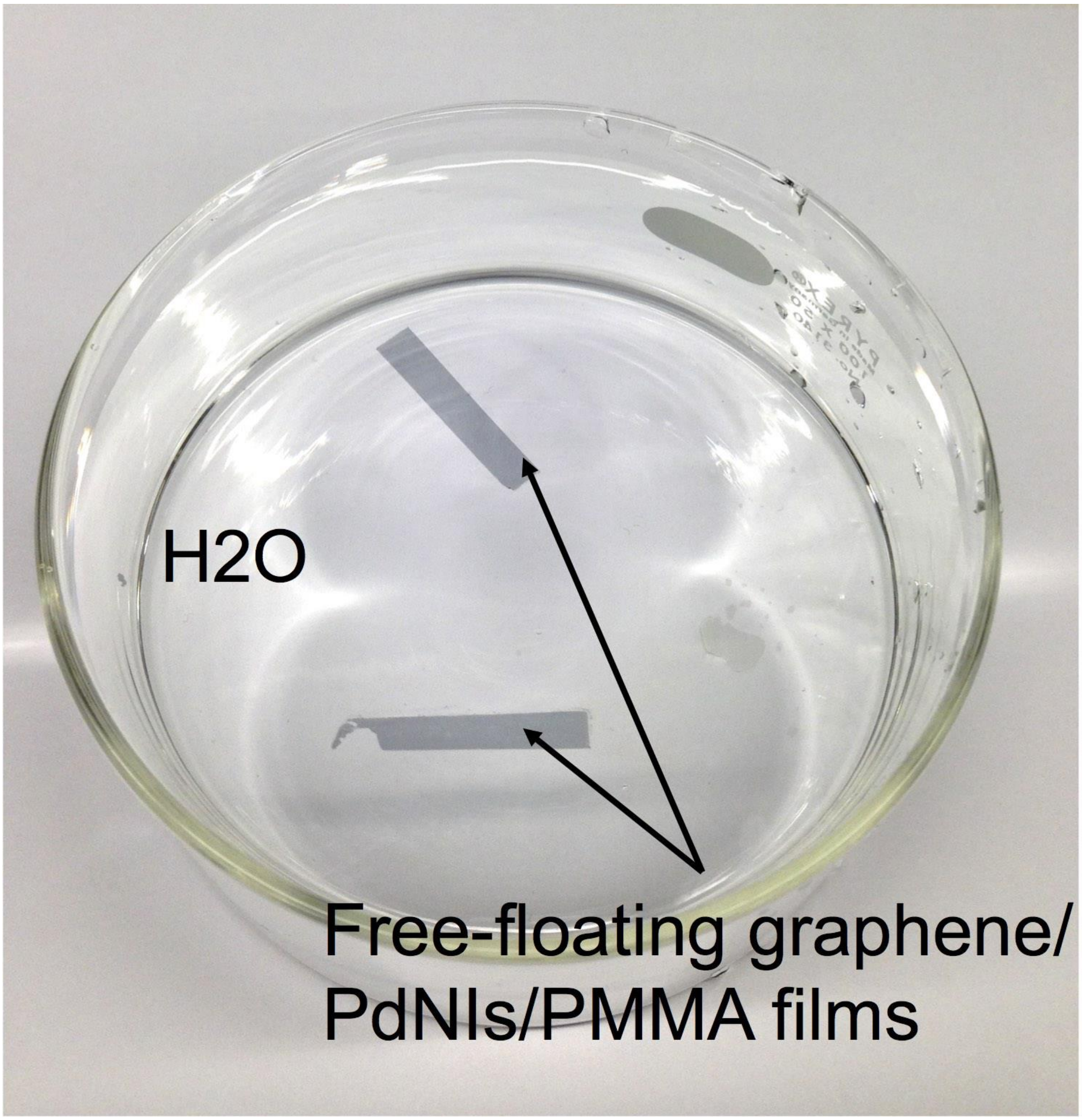

Figure S16. Free-floating graphene/NI films. A photograph of free-floating graphene/PdNI/PMMA films after copper etching and transferred into a DI water bath.

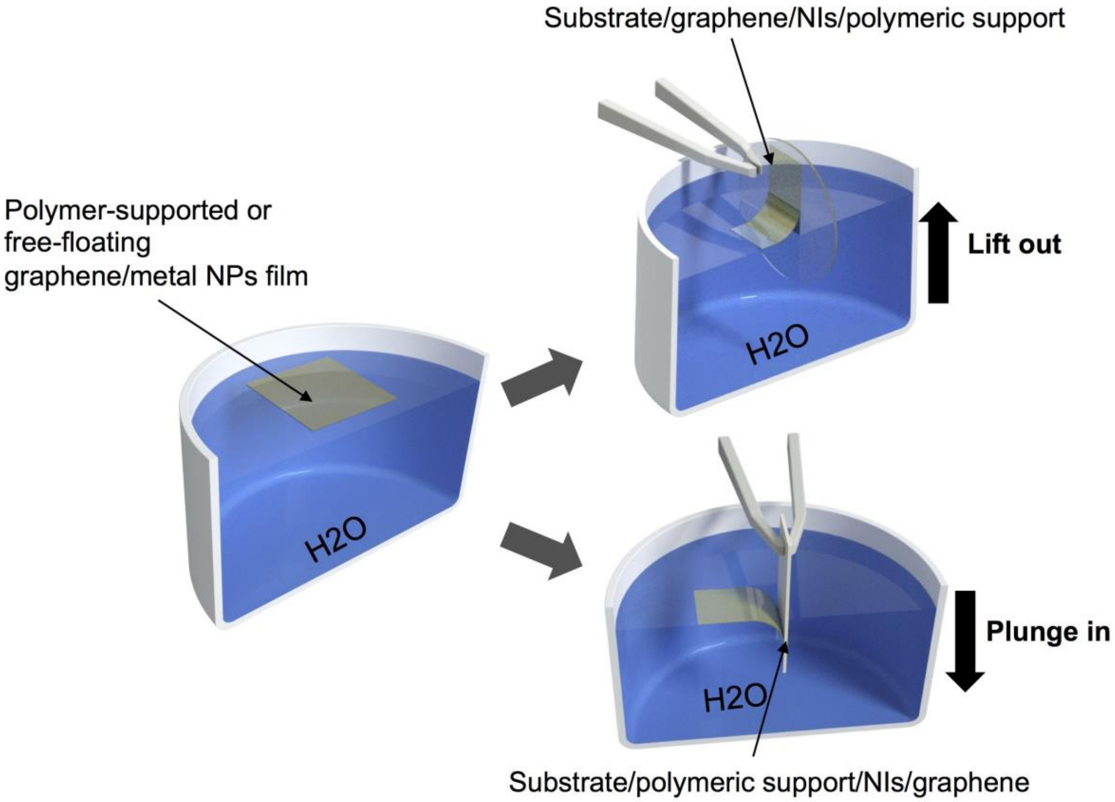

Figure S17. Graphene/NI transfer. Rendered schematic of depositing free-floating graphene/NI/polymeric support (or no polymer) onto the final receiving substrate.

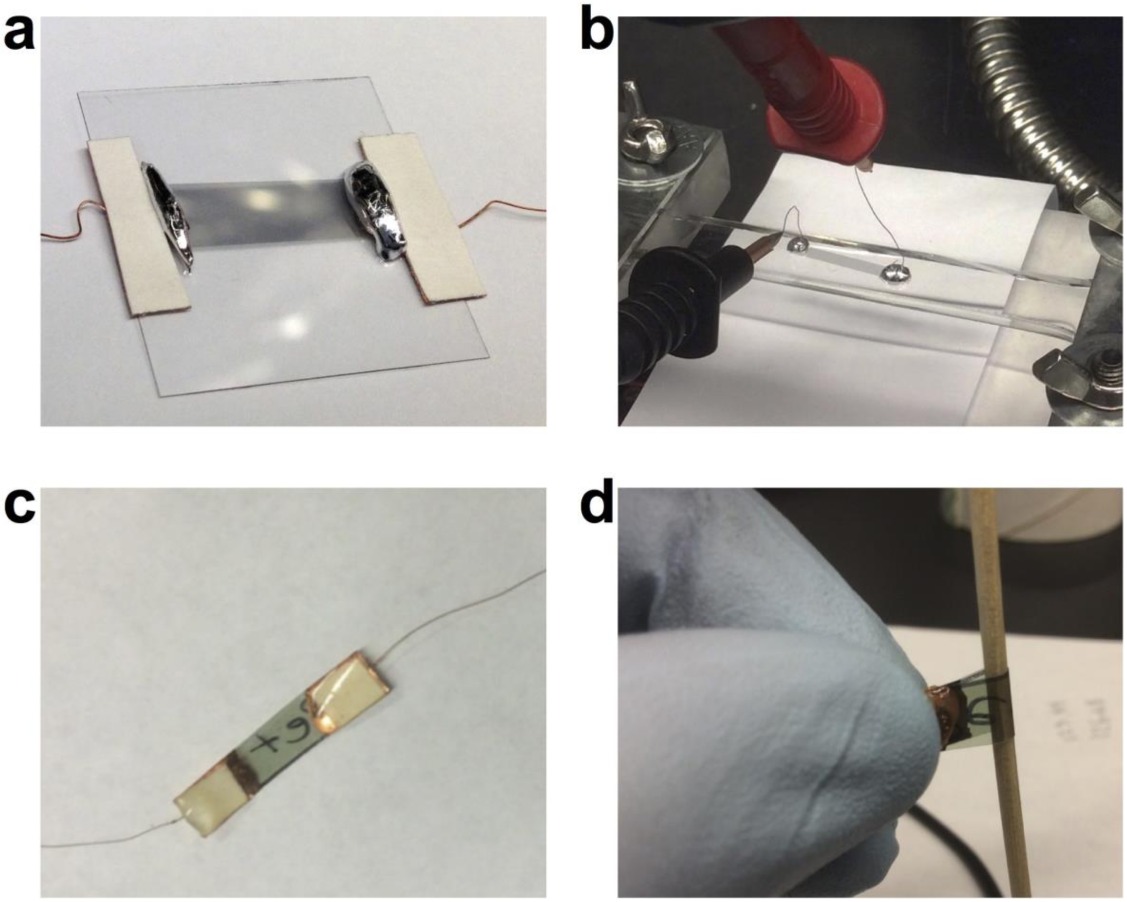

Figure S18. Graphene/PdNI sensors of rigid, flexible, and stretchable substrates. Optical photographs of a graphene/PdNI film transferred onto a glass coverslip and electrically addressed with EGaIN and copper wires (a), graphene/PdNI film transferred onto a strip of PDMS under tensile strain cyclic loading (b), PET/PdNI/graphene strain sensors unstrained (c) and bent around a toothpick (d) under ~1% tensile strain.

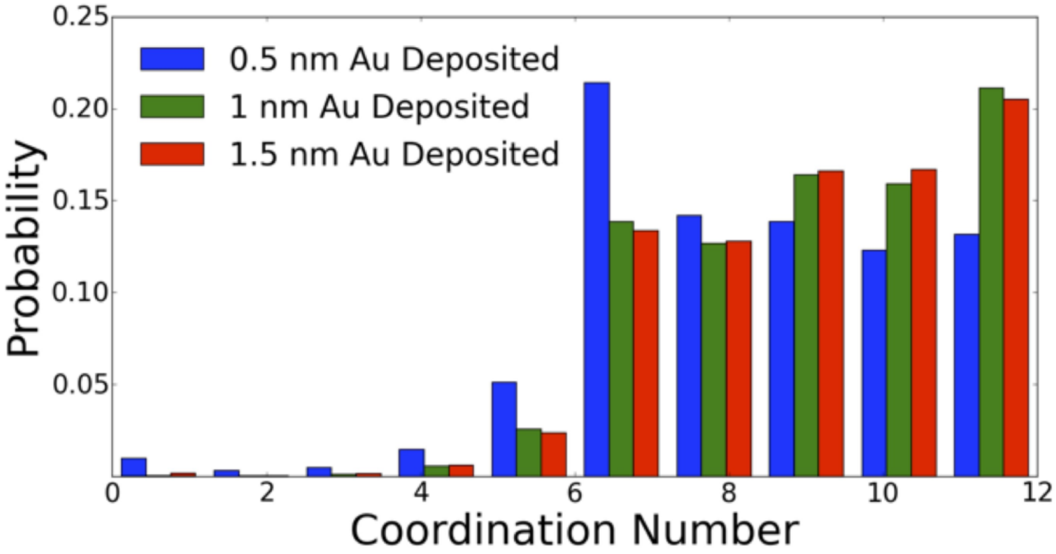

Figure S19. Evolution of the coordination number probability distribution as the gold islands are deposited

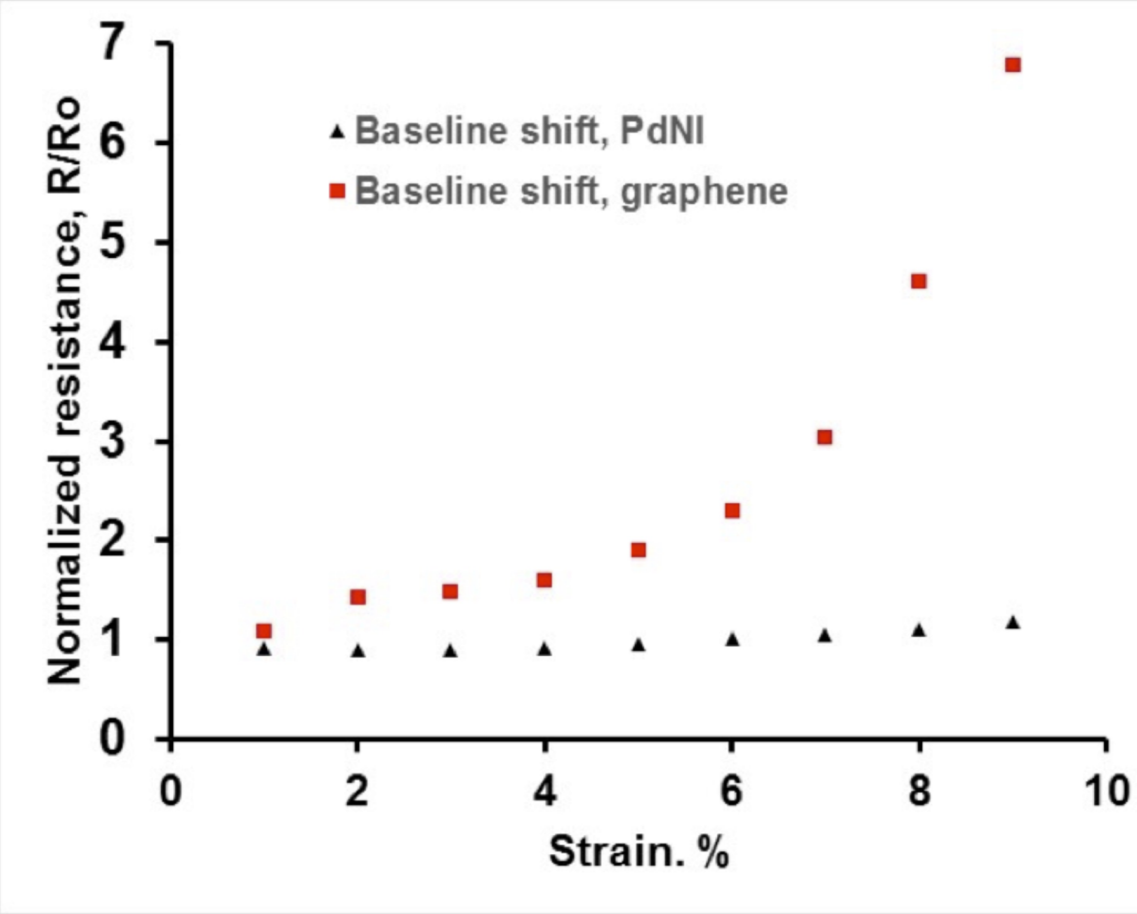

Figure S20. Sensor baseline stability. Plot of the baseline shift (normalized resistance) after 1% strain increments (20 cycles per increment) for PdNI sensor on PDMS (black triangles) and graphene on PDMS (red squares). Notice the stability of the PdNI sensor (the baseline normalized resistance drops by 0.11 until 3-4% strain is reached, potentially due to Pd particle repacking; after which it rises minimally to 1.18 after 9% strain cycles). The baseline of the graphene control was rising steadily until 5-6% was reached (graphene crack onset), after which the baseline rose exponentially and reached 6.80 after 9% strain cycles. This indicates that cracks in PdNI films can effectively reclose thus ensuring the stability of the sensor at high strains.

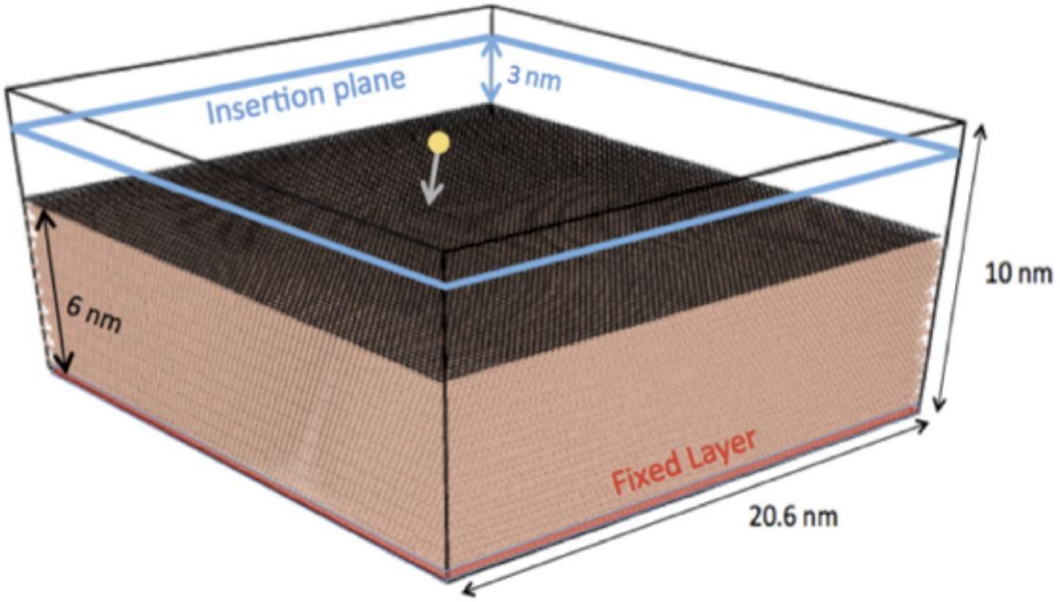

Figure S21. Simulation box. Schematic showing the geometry of the graphene/copper substrate.

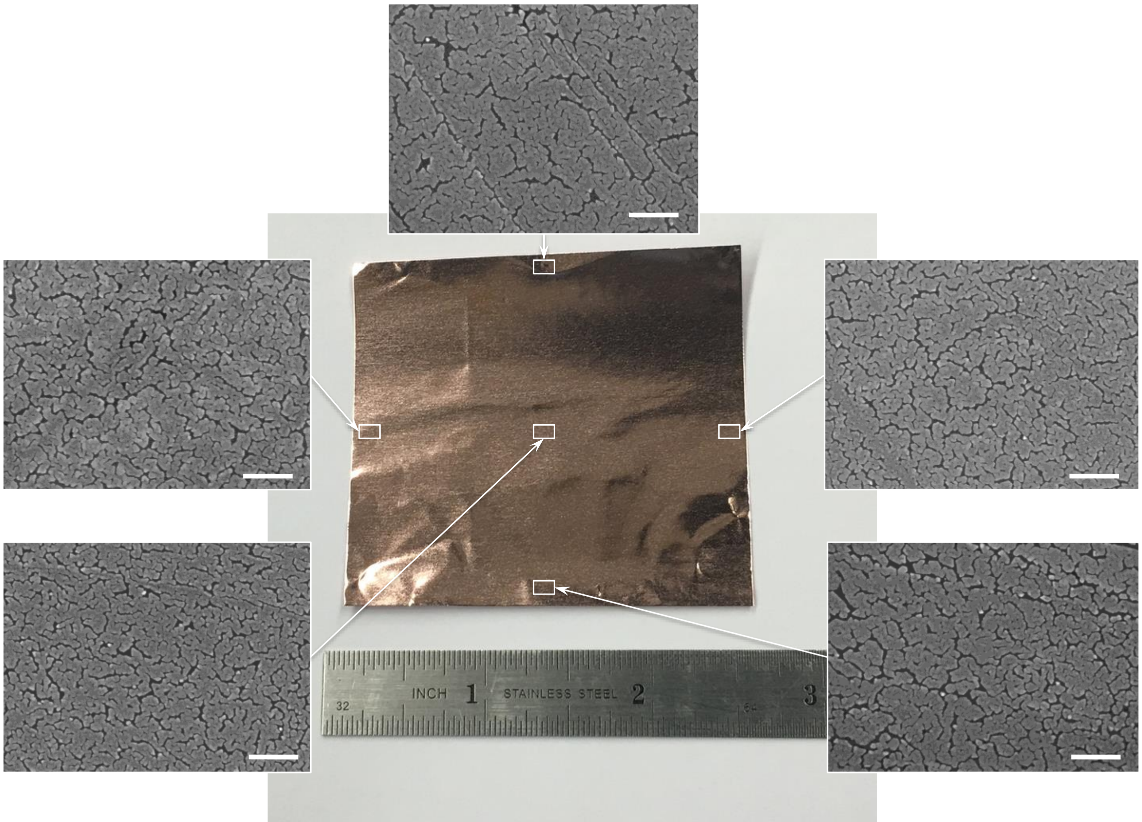

Figure S22. AuNI uniformity over large area. Photograph of large-area graphene on copper after the deposition of 10 nm of gold. Insets: SEM images of the corresponding sites throughout the sample. Note the similarity of the NI morphology over ~40 cm^2 area. Scale bars: 200 nm.

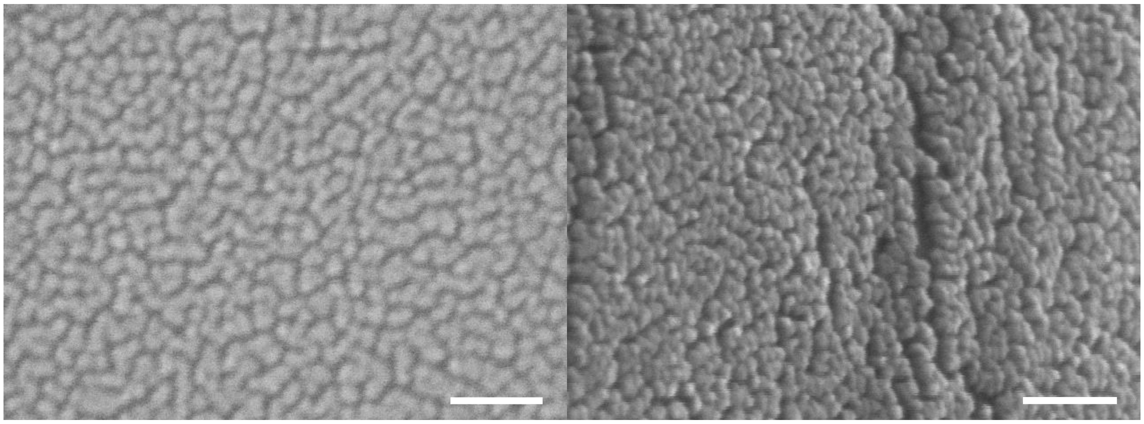

Figure S23. Coalesced PdNI. Examples of PdNI films where nanospheres coalesce/aggregate into short chains. Scale bars: 50 nm.

Interaction Pair	Interatomic Potential
Carbon-Carbon	AIREBO [20]
Carbon-Copper	Abel-Tersoff Potential [13]
Carbon-Gold	Lennard-Jones [22]
Copper-Copper	Embedded Atom Method [25]
Copper-Gold	Embedded Atom Method [26]
Gold-Gold	Embedded Atom Method [19]

Table S1. Summary of interatomic potentials used in this study.

Sensor geometry	Applied strain range (%)	Range of gauge factor	Range of reproducible behavior (strain, %)	Manipulability*	Biocompatibility	References
Graphene/NI on glass or PDMS	0.001-9	10-1330	0.001-9	YES	YES	This work
Colloidal Au NPs on PET	0.01-0.8	59-135	N/A	No	N/A	Farcau *et al.*[27] ⍰
Colloidal Au NPs on PET	0.1-0.6	12-190	0.1-0.5	No	N/A	Sangeetha *et al.*[28]
Pt NPs sputtered on SiO_2	0.06-0.15	337-735	N/A	No	N/A	Tanner *et al.*[29,30]
PU-PEDOT:PSS/CNT composite	1.6-100	<62	1.6-3.6	YES	N/A	⍰Roh *et al.*[31] ⍰

Table S2. Comparison of graphene/NI strain sensor performance.
*Manipulability – ability to be transferred onto arbitrary substrates

References

(1) Vlassiouk, I.; Fulvio, P.; Meyer, H.; Lavrik, N.; Dai, S.; Datskos, P.; Smirnov, S. *Carbon N. Y.* **2013**, *54*, 58–67.

(2) Zhang, B.; Lee, W. H.; Piner, R.; Kholmanov, I.; Wu, Y.; Li, H.; Ji, H.; Ruoff, R. S. *ACS Nano* **2012**, *6*, 2471–2476.

(3) Regmi, M.; Chisholm, M. F.; Eres, G. *Carbon N. Y.* **2012**, *50*, 134–141.

(4) Zaretski, A. V; Moetazedi, H.; Kong, C.; Sawyer, E. J.; Savagatrup, S.; Valle, E.; O'Connor, T. F.; Printz, A. D.; Lipomi, D. J. *Nanotechnology* **2015**, *26*, 45301.

(5) Ohring, M. *Materials Science of Thin Films*; 2001.

(6) Rafiee, J.; Mi, X.; Gullapalli, H.; Thomas, A. V.; Yavari, F.; Shi, Y.; Ajayan, P. M.; Koratkar, N. A. Wetting transparency of graphene. *Nature Materials*, 2012, *11*, 217–222.

(7) Li, X.; Zhu, Y.; Cai, W.; Borysiak, M.; Han, B.; Chen, D.; Piner, R. D.; Colomba, L.; Ruoff, R. S. *Nano Lett.* **2009**, *9*, 4359–4363.

(8) Bae, S.; Kim, H.; Lee, Y.; Xu, X.; Park, J.-S.; Zheng, Y.; Balakrishnan, J.; Lei, T.; Kim, H. R.; Song, Y. Il; Kim, Y.-J.; Kim, K. S.; Ozyilmaz, B.; Ahn, J.-H.; Hong, B. H.; Iijima, S. *Nat. Nanotechnol.* **2010**, *5*, 574–578.

(9) Plimpton, S. *J. Comput. Phys.* **1995**, *117*, 1–42.

(10) Stukowski, A. *Model. Simul. Mater. Sci. Eng.* **2009**, *18*, 015012.

(11) Süle, P.; Szendrő, M. *Model. Simul. Mater. Sci. Eng.* **2015**, *23*, 025001.

(12) Hermann, K. *J. Phys. Condens. Matter* **2012**, *24*, 314210.

(13) Süle, P.; Szendró, M.; Hwang, C.; Tapasztó, L. *Carbon N. Y.* **2014**, *77*, 1082–1089.

(14) Cao, Y.; Zhang, J.; Sun, T.; Yan, Y.; Yu, F. *Appl. Surf. Sci.* **2010**, *256*, 5993–5997.

(15) Zhang, J.; Liu, C.; Shu, Y.; Fan, J. *Appl. Surf. Sci.* **2012**, *261*, 690–696.

(16) Shinoda, W.; Shiga, M.; Mikami, M. *Phys. Rev. B - Condens. Matter Mater. Phys.* **2004**, *69*, 16–18.

(17) Tuckerman, M. E.; Alejandre, J.; López-Rendón, R.; Jochim, A. L.; Martyna, G. J. *J. Phys. A. Math. Gen.* **2006**, *39*, 5629–5651.

(18) Stukowski, A. *Jom* **2013**, *66*, 399–407.

(19) Foiles, S. M.; Baskes, M. I.; Daw, M. S. *Phys. Rev. B* **1986**, *33*, 7983–7991.

(20) Stuart, S.; Tutein, A.; Harrison, J. *J. Chem. Phys.* **2000**, *112*, 6472–6486.

(21) Liang, T.; Shin, Y. K.; Cheng, Y.-T.; Yilmaz, D. E.; Vishnu, K. G.; Verners, O.; Zou, C.; Phillpot, S. R.; Sinnott, S. B.; van Duin, A. C. T. *Annu. Rev. Mater. Res.* **2013**, *43*, 109–129.

(22) Helgee, E. E.; Isacsson, A. *Forthcoming* **2015**, 1–4.

(23) Tu, K.; Mayer, J. W.; Feldman, L. C. *Electronic Thin Film Science: For Electrical Engineers and Materials Scientists*; Macmillan, 1992.

(24) He, R.; Zhao, L.; Petrone, N.; Kim, K. S.; Roth, M.; Hone, J.; Kim, P.; Pasupathy, A.; Pinczuk, A. *Nano Lett*. **2012**, *12*, 2408–2413.

(25) Sheng, H. W.; Kramer, M. J.; Cadien, a.; Fujita, T.; Chen, M. W. *Phys. Rev. B - Condens. Matter Mater. Phys*. **2011**, *83*, 1–20.

(26) Ward, L.; Agrawal, a; Flores, K. M.; Windl, W. *Model. Simul. Mater. Sci. Eng*. **2012**.

(27) Farcau, C.; Moreira, H.; Viallet, B.; Grisolia, J.; Ciuculescu-Pradines, D.; Amiens, C.; Ressier, L. *J. Phys. Chem. C* **2011**, *115*, 14494–14499.

(28) Sangeetha, N. M.; Decorde, N.; Viallet, B.; Viau, G.; Ressier, L. *J. Phys. Chem. C* **2013**, *117*, 1935–1940.

(29) Tanner, J. L.; Mousadakos, D.; Giannakopoulos, K.; Skotadis, E.; Tsoukalas, D. High strain sensitivity controlled by the surface density of platinum nanoparticles. *Nanotechnology*, 2012, *23*, 285501.

(30) Tanner, J. L.; Mousadakos, D.; Broutas, P.; Chatzandroulis, S.; Raptis, Y. S.; Tsoukalas, D. In *Procedia Engineering*; 2011; Vol. 25, pp. 635–638.

(31) Roh, E.; Hwang, B.-U.; Kim, D.; Kim, B.-Y.; Lee, N.-E. *ACS Nano* **2015**, *9*, 6252–6261.